NUMERICAL MODELLING OF HIGH TEMPERATURE SUPERCONDUCTING TAPES AND CABLES

THÈSE N^{O} 2909 (2003)

PRÉSENTÉE À LA FACULTÉ INFORMATIQUE ET COMMUNICATIONS

Institut de systèmes de communication

SECTION DES SYSTÈMES DE COMMUNICATION

ÉCOLE POLYTECHNIQUE FÉDÉRALE DE LAUSANNE

POUR L'OBTENTION DU GRADE DE DOCTEUR ÈS SCIENCES TECHNIQUES

PAR

Francesco GRILLI

laurea in fisica, Università degli Studi di Genova, Italie
et de nationalité italienne

acceptée sur proposition du jury:

Prof. M. Hasler, directeur de thèse
Dr B. Dutoit, rapporteur
Prof. R. Flükiger, rapporteur
Prof. M. Q. Tran, rapporteur
Dr S. Zannella, rapporteur

Lausanne, EPFL
2004

To Sara

Abstract

This Ph.D. thesis is focused on the numerical modelling of high-T_c superconductors (HTS) at the operating temperature of 77 K (liquid nitrogen). The purpose of numerical modelling is to precisely calculate the current and field distributions inside HTS devices (tapes, cables) and the corresponding AC losses, which are one of the most important limiting factors for a large-scale application of such materials.

From the electrical point of view, superconductors are characterized by a strongly non-linear voltage-current relation, which defines the transition from superconducting to normal state. In the case of HTS, the steepness of this transition is smoother than for low-T_c superconductors (LTS), so that the commonly used critical state model (CSM) gives a too simplified representation of their electromagnetic behaviour and can be used for a qualitative description only.

In this thesis the finite element method (FEM) has been used for precisely computing the current and field distributions as well as for evaluating the AC losses in HTS devices. The superconducting transition is modelled with a power-law relation, $E(J) = E_c(J/J_c)^n$, which is derived from the fit of transport measurements.

Firstly, the results obtained with the software package FLUX3D on multi-filamentary tapes have been validated by means of a comparison with the ones obtained by another software package (FLUX2D). The results from FLUX2D, having already been successfully compared with experimental measurements within the framework of two previous Ph.D. theses at LANOS, have been used as reference.

Secondly, two power-law models, which take into account the spatial variation of the critical current density inside HTS tapes and its strongly anisotropic dependence on the magnetic field, have been implemented in FLUX3D. In most cases, this latter dependence is extremely important, since the transport capacity of the superconductor is considerably reduced (and its power loss sensibly increased) by the presence of a magnetic field.

Afterwards, FEM modelling of HTS tapes has been extended to cables. HTS cables are in general composed by different layers of several tapes and have a quite complex three-dimensional structure: in fact, the layers are wound around a central cylindrical support with different pitch lengths and relative winding orientations, in order to obtain a uniform repartition of the transport current among the layers, which minimizes the total AC losses. For overcoming the difficulties of a direct 3D FEM simulation, a simple electrical model, which allows to find the optimal pitch lengths and whose results are the input data for a 2D FEM evaluation of the AC losses, has been developed. FEM computations have also been used to investigate the influence of the non-uniformity of the tape properties (contact resistance, critical current, power index) on the global loss performance of a single-layer HTS cable.

As an alternative to FEM computations, an equivalent circuit model of HTS cables has been utilized. It describes the cable from the macroscopic point of view and allows to compute the current repartition among the layers and the corresponding AC losses, without the necessity of having detailed information about individual tapes.

In the framework of the European project BIG-POWA, I have collaborated to the assembling process of a HTS power-link at the Pirelli Labs, in the Milan region, Italy.

Finally, 3D simulations have been performed to extensively study the coupling effect between two superconducting filaments via the resistive matrix, which is a typical case where analytical solutions exist for very peculiar geometries and physical conditions only. FEM simulations have been utilized to study the dependence of the filament coupling on the physical and geometrical parameters of the conductors.

Version abrégée

Cette thèse a pour thème la modélisation numérique des supraconducteurs à haute température critique (HTS). Le but de cette modélisation est de calculer précisément les distributions de courant et de champ magnétique à l'intérieur de dispositifs HTS (rubans, câbles) ainsi que les pertes AC correspondantes, ces dernières étant un des plus importants facteurs limitants des applications à grande échelle de ce type de matériaux.

Du point de vue électrique, les supraconducteurs sont caractérisés par une relation courant-tension fortement non linéaire, qui décrit la transition de l'état supraconducteur à l'état normal. Dans le cas des HTS, la rapidité de cette transition est plus modérée que pour les supraconducteurs à basse température critique (LTS), donc le modèle d'état critique souvent utilisé pour les LTS donne une représentation trop simplifiée de leur comportement electro-magnétique et ne peut être utilisé que pour une description qualitative.

Dans ce mémoire la méthode des éléments finis (FEM) a été utilisée pour calculer précisément les distributions de courant et de champ, ainsi que pour évaluer les pertes AC des différents dispositifs. La transition supraconductrice est modélisée grâce à une loi de puissance, $E(J) = E_c(J/J_c)^n$, obtenue par interpolation de mesures en transport de courant.

En premier lieu, les résultats obtenus avec le logiciel FLUX3D pour des rubans multi-filamentaires ont été validés par une comparaison avec ceux obtenus par un logiciel plus ancien et en deux dimensions (FLUX2D). Les résultats de FLUX2D - eux-mêmes solidement validés par des mesures expérimentales dans le cadre de deux thèses précédentes au LANOS - ont été utilisés comme référence.

En second lieu, le modèle de la loi de puissance a été implementé dans FLUX3D en considérant la variation spatiale de la densité de courant critique dans les rubans HTS et sa dépendance fortement anisotropique au champ magnétique. Dans la plus part des cas, cette dernière dépendance est extrêmement importante, car la capacité de transport du supraconducteur est considérablement réduite (et ses pertes AC sensiblement augmentées) par la présence d'un champ magnétique.

En troisième lieu, la modélisation FEM des rubans HTS a été étendue aux câbles. En général, les câbles HTS sont composés de différentes couches, elles mêmes composées de différents rubans, conduisant à une géométrie complexe : les couches sont torsadées autour d'un support cylindrique avec différentes longueurs et directions de pas, ceci afin d'obtenir une répartition de courant entre les couches la plus uniforme possible, minimisant ainsi les pertes AC. Pour surmonter les difficultés d'une simulation FEM directement en 3D, souvent trop coûteuse en temps de calcul, on a développé un modèle électrique simple, qui permet de trouver les longueurs de pas optimales et dont les résultats sont utilisés pour l'évaluation des pertes AC dans les simulations FEM en 2D. Les calculs FEM ont été aussi utilisés pour étudier l'influence de la non uniformité des propriétés individuelles des rubans (résistance de contact, courant critique, index de puissance) sur la performance globale et les pertes d'un câble HTS mono-couche.

Comme alternative aux simulations FEM, on a également utilisé un modèle de circuit électrique équivalent pour des câbles HTS. Ce modèle décrit le câble d'un point de vue macroscopique et permet de calculer la répartition du courant entre les couches et les pertes AC

correspondantes, sans avoir à calculer ces informations détaillées pour chaque ruban.

Dans le cadre du projet européen BIG-POWA, j'ai collaboré à l'assemblage d'un tronçon de câble de puissance HTS, qui a eu lieu dans les laboratoires Pirelli, en Italie.

Enfin, on a réalisé des simulations 3D pour étudier en détail l'effet de couplage entre deux filaments supraconducteurs via une matrice résistive. C'est un cas typique où des solutions analytiques n'existent que pour des géométries et des conditions physiques simples et bien déterminées. En particulier, on a utilisé les simulations FEM pour déterminer la dépendance du couplage aux paramètres physiques et géométriques des conducteurs.

Riassunto

Questa tesi di dottorato è incentrata sulla modellizzazione numerica di superconduttori ad alta T_c (HTS), operanti alla temperatura di 77 K (azoto liquido). Lo scopo della modellizzazione numerica è calcolare precisamente le distribuzioni di campo e corrente all'interno di dispositivi HTS (nastri, cavi) e le perdite AC corrispondenti. Queste ultime costituiscono uno dei fattori limitanti più importanti per un'applicazione a larga scala di questo tipo di materiali.

Dal punto di vista elettrico, i superconduttori sono caratterizzati da una relazione tensione-corrente fortemente non lineare, che definisce la transizione dallo stato superconduttore allo stato normale. Nel caso dei superconduttori HTS, la ripidità di tale transizione è meno accentuata rispetto ai superconduttori a bassa temperatura critica (LTS); ne segue che il modello di stato critico (CSM) comunemente usato fornisce una rappresentazione troppo semplificata del loro comportamento elettromagnetico e può essere usato solamente per una descrizione qualitativa.

In questo lavoro il metodo a elementi finiti (FEM) è stato utilizzato per calcolare precisamente le distribuzioni di campo e di corrente in dispositivi HTS e per valutarne le perdite AC. La transizione superconduttiva è modellizzata per mezzo di una relazione di potenza, $E(J) = E_c(J/J_c)^n$, che è stata derivata dal fit di misure di trasporto.

In primo luogo, i risultati ottenuti con il programma FLUX3D su un nastro multi-filamentare sono stati validati mediante un confronto con quelli ottenuti con un altro programma (FLUX2D). I risultati di FLUX2D, essendo già stati paragonati con successo con le misure sperimentali nell'ambito di due tesi precedenti al LANOS, sono stati usati come riferimento.

In secondo luogo sono stati implementati due modelli della legge di potenza, che tengono in considerazione la variazione spaziale della densità di corrente critica nei nastri HTS e la dipendenza fortemente anisotropica dal campo magnetico. In molti casi quest'ultima dipendenza è estremamente importante, dato che la capacità di trasporto del superconduttore viene considerevolmente ridotta (e le sue perdite AC sensibilmente aumentate) dalla presenza di un campo magnetico.

Successivamente, la modellizzazione FEM dei nastri HTS è stata estesa ai cavi. I cavi HTS sono in generale costituiti da differenti strati di nastri e hanno una struttura tridimensionale piuttosto complessa: in particolare, gli strati vengono avvolti attorno a un supporto cilindrico centrale con lunghezze di pitch e orientazione relativa differenti, al fine di avere una ripartizione di corrente uniforme e minimizzare le perdite AC. Per superare le difficoltà di una simulazione diretta FEM 3D, è stato sviluppato un semplice modello elettrico, che permette di trovare le lunghezze di pitch ottimali e i cui risultati vengono utilizzati per una valutazione delle perdite AC per mezzo di simulazioni FEM 2D. Le simulazioni FEM sono state anche utilizzate per studiare l'influenza della non uniformità delle proprietà dei nastri (resistenza di contatto, corrente critica, indice di potenza) sulla prestazione globale in termini di perdite AC di un cavo HTS mono-strato.

Come alternativa alle simulazioni FEM, si è utilizzato un circuito elettrico equivalente per i cavi HTS. Questo modello descrive il cavo dal punto di vista macroscopico e permette di valutare la ripartizione di corrente tra gli strati e le perdite AC, senza la necessità di calcolare informazioni dettagliate per ciascun nastro.

Nell'ambito del progetto europeo BIG-POWA, ho collaborato all'assemblaggio di un power-

link HTS, realizzato nei laboratori Pirelli, in Italia.

Infine, sono state eseguite simulazioni 3D per studiare dettagliatamente l'effetto di accoppiamento tra i filamenti superconduttori attraverso una matrice resistiva: è questo un tipico caso per cui le soluzioni analitiche esistono solo per ben determinate geometrie e condizioni fisiche. In particolare, le simulazioni FEM sono state utilizzate per determinare come l'accoppiamento dipenda dai parametri fisici e geometrici dei conduttori.

Acknowledgments

There are several persons who, directly or not, have contributed to this thesis work and whom I would like to thank.

First of all, Prof. Martin Hasler, my thesis director, for accepting me as Ph.D. assistant at the Laboratory of Nonlinear Systems. Then, Dr. Bertrand Dutoit, my thesis supervisor, for the useful discussions and for keeping awake my point of view of physicist on superconductivity. I would like to thank the other members of the "Supra Group": Dr. Svetlomir Stavrev and Mr. Joseph Duron. To Svet I am particularly grateful, for his support, for the stimulating discussions and also for his patience as precious English reference.

Amongst the other LANOS members, I would like to thank our secretaries, Ms. Christiane Good and Ms. Erika Raetz; then Dr. Thomas Schimming, for his continuous availability in solving problems associated to computers and software, and Dr. Oscar De Feo, for his technical support, especially concerning the use of LaTeX and Matlab.

In the past three years, I have collaborated with several colleagues from other institutes, who deserve a particular mention. First of all, Dr. Giovanni Grasso (INFM), the supervisor of my diploma work in Genoa. He is the person who made this experience in Switzerland possible for me. Then, Dr. Yifeng Yang (University of Southampton) for the friendly collaboration in the study of the coupling effect; Dr. Yann Le Floch (Cedrat) for guiding me through the world of FLUX3D; Mr. Sergio Spreafico (Pirelli Labs) for giving me useful details about cable manufacturing and for sharing with me the experience of assembling the BIG-POWA power-link; Dr. Mårten Sjöström (Mid-Sweden University) for the collaboration in the application of his equivalent circuit model to HTS cables; Dr. Fedor Gömöry (Slovak Academy of Sciences) for the collaboration on the study of the cable with non-uniform tape properties and the useful discussions.

On a more personal level, I am grateful to my parents for supporting me in this experience abroad, as they have always done during all my studies. A special memory is to my grandparent Silvio, who would have been very proud of this achievement.

Finally, I would like to thank my friends Chiara and Eros, for keeping always in touch with me during these years.

"O frati", dissi "che per cento milia
perigli siete giunti a l'occidente,
a questa tanto picciola vigilia
d'i nostri sensi ch'è del rimanente,
non vogliate negar l'esperienza,
di retro al sol, del mondo sanza gente.
Considerate la vostra semenza:
fatti non foste a viver come bruti,
ma per seguir virtute e canoscenza".
(Dante, Inf. XXVI, 112)

Dai diamanti non nasce niente
dal letame nascono i fior.
(Fabrizio De André, Via del Campo)

Contents

Chapter 1

Introduction

Since the discovery of high-T_c superconducting materials in 1986 [1], an intense research activity started to look for economically reliable solutions for exploiting their properties.

In order to improve the effectiveness of the use of HTS, there are different directions where the research activity must be primarily focused [2]:

1. the understanding of AC loss mechanisms, in order to be able to reduce the losses;
2. the increase of the cross-section area of the superconductor (fill factor) carrying the current;
3. the reduction of the price, by increasing the production rate;
4. the improvement of the $I_c(B)$ characteristics.

HTS materials can be utilized for different purposes: superconducting magnetic energy storage (SMES), power transmission, transformers, rotating machines, fault current limiters.

This thesis work is dedicated to the aspect of power transmission, which is performed by means of HTS cables. They are composed by different layers of several HTS tapes, which, in their turn, are composed by different filaments of HTS material.

For the transport of power energy, one of the most promising materials appeared to be the $Bi_2Sr_2Ca_2Cu_3O_{10+x}$ ceramic compound (Bi-2223), which is usually manufactured in the form of flat tapes and, having a critical temperature of about 110 K, can be cooled with liquid nitrogen, instead of other more traditional and expensive cryogenic liquids.

Unfortunately, for Bi-2223 the zero-resistance behaviour is observed with DC transport currents only. In fact, due to the peculiar structure of this material, several dissipative mechanisms appear with AC transport currents or when the superconductor is subjected to an external AC magnetic field. Therefore, for a large-scale commercial application, the reduction of AC losses constitute a key point.

The transport capacity of Bi-2223 depends on many parameters: in particular, it is extremely sensible to the presence of AC magnetic fields, either self-generated by the transport current or created by neighbouring conductors. In addition, the AC losses strongly depend on the geometrical structure of the considered device. For example, a wrong alignment of the superconducting filaments inside a wire can drastically enhance the AC losses.

From the design point of view, it is therefore important to be able to precisely calculate the current/field distributions inside superconductors in order to make a fair estimate of the AC losses for given geometrical configurations and working conditions.

The simpler approach is to use analytical models. Unfortunately, such models are valid for very peculiar geometries (often involving infinite dimensions) and are usually based on the critical state model (CSM) for the description of the electrical behaviour of such materials, which is a too rough approximation.

Numerical models are a reliable tool for overcoming these difficulties. In particular, finite element method (FEM) simulations can give very accurate results for electromagnetic problems. In this thesis, a new FEM software package, FLUX3D, has been tested and extensively used to solve 2D and 3D problems involving HTS tapes and cables.

The thesis is structured as follows:

Chapter 2 contains a brief introduction to high-T_c superconductivity from the phenomenological point of view, with particular attention to the properties and manufacturing of Bi-2223/Ag tapes.

Chapter 3 shows two examples for which analytical solutions based on the critical state model can be found. The advantages coming from the use of finite element method technique are pointed out. The implementation of the non-linear voltage-current relation into FLUX3D is explained, both for 2D and 3D formulations. The series of steps for solving a FEM problem is described.

Chapter 4 contains the results of 2D FEM simulations of multi-filamentary Bi-2223/Ag tapes. The results have been validated by means of a comparison with the ones obtained with the software package FLUX2D and with an analytical method originally developed by Brandt. Presented is also a refinement of the $E - J$ relation, with the dependence of two parameters of the power-law - the critical current density J_c and the power index n - on the lateral position of the filaments inside the tape and on the local magnetic field experienced by the superconductor. The differences in the current distribution and in the AC losses with respect to the constant J_c and n model are discussed. At the end of the chapter, a recently developed 3D formulation for problems coupled with circuit equations is validated and tested.

Chapter 5 is dedicated to the extension of modelling from tapes to cables. 2D FEM calculations are integrated with an electrical model, which, considering the cable from the macroscopic point of view, allows to find the optimal pitch lengths of the layers leading to a uniform repartition of the current and to a minimization of the total AC losses. The influence of the non-uniformity of the properties of the individual tapes on the global loss performance of a single-layer HTS cable is discussed. Presented is also an equivalent circuit model of the cable, which allows to determine the current repartition and the different contributions to the AC losses (hysteretic, resistive) in a very quick way, without computing in detail the current and field distributions inside superconductors. Finally, the manufacturing process and the characterization of a HTS power-link assembled in the framework of the European project BIG-POWA is described.

Chapter 6 investigates the coupling effect between two superconducting filaments via the resistive matrix induced by an external varying magnetic field. 3D FEM simulations are used to overcome the limits of analytical calculations, which are valid in the peculiar case of fully penetrated infinite slabs only.

Finally, chapter 7 presents the conclusions of this thesis work, outlining the most interesting contributions and indicating possible future developments for the modelling of superconductors.

Chapter 2

High-T_C superconductors

2.1 A very brief introduction

Nowadays superconductivity has an almost one century long history[1], which began in 1908 with the possibility of obtaining very low temperatures by liquefying helium.

The first experimental evidence of this phenomenon dates back to 1911, when Kamerlingh Onnes [5] discovered that the resistivity of mercury fell sharply to zero at about 4 K. This behaviour is not a peculiarity of mercury, but it is quite diffused: among the elements of the periodic table, more than twenty become superconducting at sufficiently low temperature, several semiconductors can become superconducting under suitable conditions, whereas the number of alloys with superconducting properties is in the order of thousands [6]. The temperature below which a material becomes superconducting is called *critical temperature* and is usually indicated as T_c, see Fig. 2.1. The measured zero resistance seems to be an intrinsic property of the material and not only a matter of sensibility of the experimental measurements. One of the consequences of the zero resistance is the existence of permanent currents: if a current is let flow in a superconducting ring whose inductance is L, the current decays according to

$$i(t) = i(0)e^{-Rt/L}, \tag{2.1}$$

where R is the resistance of the ring. The measurement of the generated magnetic field allows to detect the decay of the current. Some experiments have proved the existence of permanent currents over years, so that the resistance of superconducting materials seems to be actually zero. Superconductors have also interesting properties in the presence of a magnetic field. Not only they oppose to any variation of the magnetic flux at their interior, but they try to avoid any penetration of the magnetic flux itself. This property is known as *Meissner effect* and was discovered in 1933 [7]. The value of the magnetic field above which the flux penetrates the material is called *critical field* and is usually indicated as H_c. In reality, this description is true only for the so-called *type-I* superconductors. Another group of superconductors is in fact represented by *type-II* superconductors, which preserve the zero resistivity behaviour but let the magnetic flux partially penetrate into their interior. The peculiarity of this state, which is called *mixed state*, is that the magnetic flux penetrates the material in the form of quanta. Each flux quantum has a value $\Phi_0 = h/e^*$, where h is the Planck constant and e^* the effective electric charge. The experimental value of Φ_0 gives e^* a value two times higher than the electron charge: this is in agreement with the microscopic theory of Bardeen, Cooper and Schieffer (BCS) [8], according to which the superconducting electrons are coupled in pairs (*Cooper pairs*), which

[1] This chapter is dedicated to high-T_c superconductors, with particular attention to the properties of Bi-2223/Ag tapes. Details about the microstructure and manufacturing process of the tapes are given. They are mostly derived from my diploma work at the University of Genoa, Italy [3]. For general notions about superconductivity, a very good introduction can be found in [4].

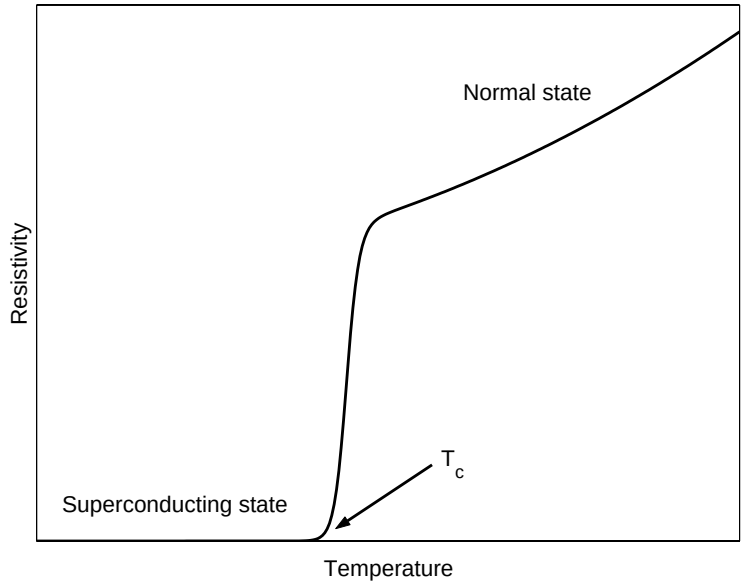

Figure 2.1: Resistivity of a superconducting material as a function of the temperature. In the case of metals, the purer the material the steeper the transition.

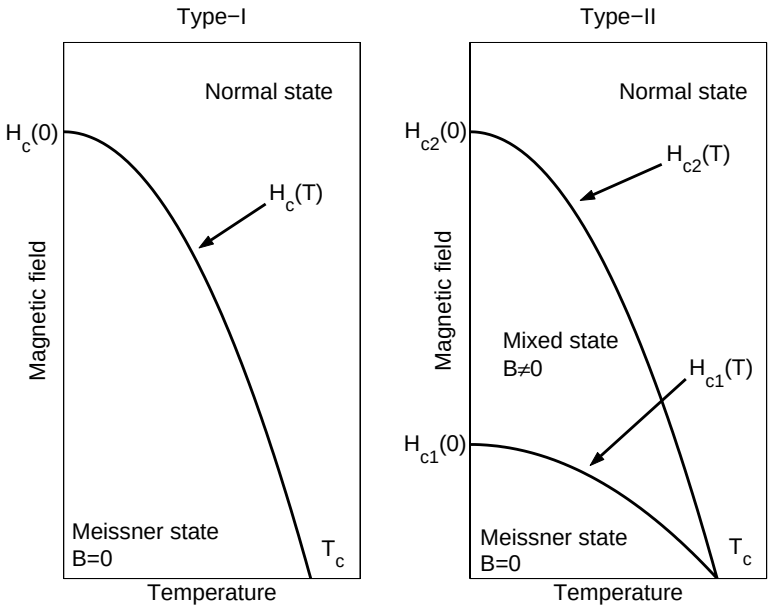

Figure 2.2: Dependence of the critical field(s) on the temperature for type-I and type-II superconductors.

carry the current without dissipation. Figure 2.2 depicts the dependence of the critical field(s) on the temperature for the two types of superconductors.

2.2 Theory of superconductivity

2.2.1 The London Theory

The first phenomenological theory of superconductivity was formulated by the brothers F. and H. London [9]. One of the consequences of the zero resistance is that the variation of the magnetic field dies away exponentially inside the superconductors, as can be easily derived from Maxwell's equations. In fact, if n_s is the number of "superelectrons" per unit volume moving with velocity $\mathbf{v_s}$, one has:

$$\mathbf{J_s} = n_s e \mathbf{v_s} \tag{2.2}$$

$$\dot{\mathbf{J}}_\mathbf{s} = \frac{n_s e^2}{m}\mathbf{E}, \tag{2.3}$$

where m and e are the electron mass and the electric charge, respectively. Maxwell's equations allow to find a relation between the current and magnetic field in superconductors.

Starting from

$$\dot{\mathbf{B}} = -\nabla \times \mathbf{E}, \tag{2.4}$$

$$\nabla \times \mathbf{H} = \mathbf{J} + \dot{\mathbf{D}} \tag{2.5}$$

and assuming $\mu_r = 1$ (non-magnetic material) and $\dot{\mathbf{D}} = 0$ (negligible displacement current), one can obtain, after few manipulations,

$$\nabla^2 \dot{\mathbf{B}} = \frac{1}{\alpha}\dot{\mathbf{B}}, \tag{2.6}$$

where $\alpha = m/(\mu_0 n_s e^2)$ is a constant. This condition, for a mono-dimensional geometry with uniform applied field B_a, gives

$$\frac{\partial^2 \dot{B}}{\partial x^2} = \frac{1}{\alpha}\dot{B}, \tag{2.7}$$

whose solution is[2]

$$\dot{B}(x) = \dot{B}_a \exp(-x/\sqrt{a}). \tag{2.8}$$

This means that changes in flux density do not penetrate too far inside the material, so that at a sufficient distance from the surface the flux density does not change with time, irrespective of what is happening to the external applied field.

The assumption made by F. and H. London was that, for superconductors, the relation (2.6) was valid not only for $\dot{\mathbf{B}}$, but also for $\mathbf{B}$ itself, according to the observed Meissner effect:

$$\nabla^2 \mathbf{B} = \frac{1}{\alpha}\mathbf{B}. \tag{2.9}$$

As a consequence, the flux density dies away exponentially inside the superconductor and the distance at which it falls to $1/e$ of the value at the surface is called the *London penetration depth* (λ_L), as sketched in Fig. 2.3. The London penetration depth is given by the formula $\sqrt{m/\mu_0 n_s e^2}$ and typical values for metals are in the order of 10^{-8} m.

With further manipulations of Maxwell's equations, one can summarize the general London equations as follows:

$$\begin{cases} \mathbf{J} & = \mathbf{J_n} + \mathbf{J_s} \\ \mathbf{J_n} & = \sigma' \mathbf{E} \\ \nabla \times \mathbf{J_s} & = -\mu_0^{-1} {\lambda_L}^{-2} \mathbf{B} \\ \dot{\mathbf{J}}_\mathbf{s} & = \mu_0^{-1} {\lambda_L}^{-2} \mathbf{E}. \end{cases} \tag{2.10}$$

[2]The solution $\dot{B}(x) = \dot{B}_a \exp(x/\sqrt{a})$, which has no physical meaning, is neglected.

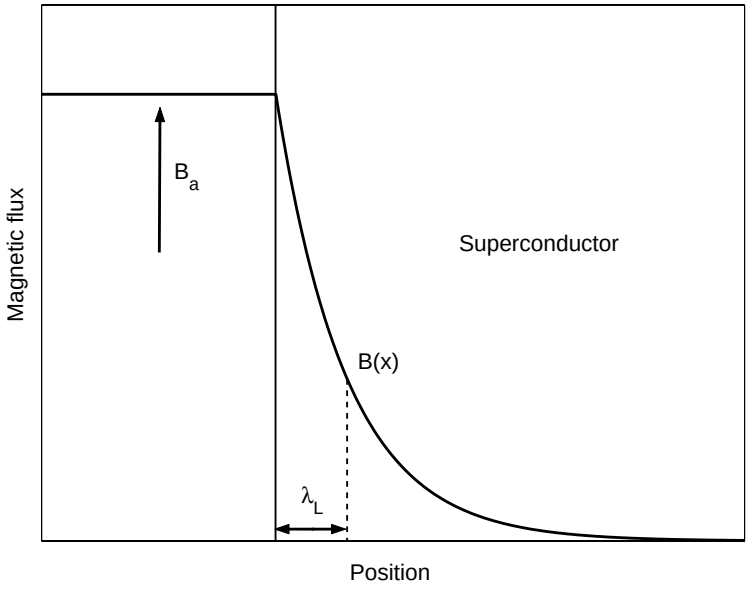

Figure 2.3: Magnetic flux penetration inside a superconductor. The London penetration depth λ_L is indicated.

The first equation describes the total current as sum of the "normal" current and the "supercurrent". The second one is Ohm's law referred to the normal current, where σ' is the conductivity associated with normal electrons. The last two equations describe the relation between the supercurrent and the magnetic and electric field. In principle, the set of equations (2.10) allows to compute the current and field distributions inside superconductors under different conditions. In reality, the equations are derived starting from the assumption that the relation (2.9) holds, which is only a guess for describing the experimental evidence that superconductors tend to repulse the magnetic field from their interior. Therefore, the London equations are only approximations, which for several purposes are sufficiently accurate, especially for a qualitative description. For example, a small penetration depth is observed in the reality, but the quantitative values are different from the predictions based on this theory.

2.2.2 The Ginzburg-Landau Theory

The Ginzburg-Landau theory [10], based on quantum mechanics instead of classical electromagnetism, is alternative to the London theory. Nevertheless, similarly to the latter, it is a phenomenological theory in the sense that it makes certain *ad hoc* assumptions for describing the state transition.

According to this theory, the behaviour of superconducting electrons can be described by a wave function Ψ, whose square modulus gives the density of superconducting electrons. Another assumption is that the free energy of the superconducting state differs from that of the normal state by an amount which can be written as a power series in $|\Psi|^2$. Near T_c it is sufficient to retain the first two terms of such expansion. In addition, non-constant values of Ψ in the space give rise to kinetic energy of the same kind of the term in Schrödinger's equation. In order to take into account the effects of such space gradient of Ψ, an additional term, proportional to the square of the gradient, is added to the expression for the energy. Finally, the effects of a magnetic field are taken into consideration by replacing the momentum $\mathbf{p}$ with $\mathbf{p} - q\mathbf{A}$ in all the

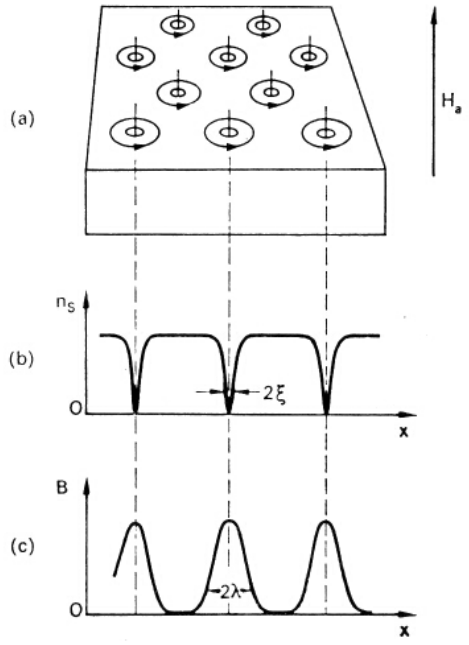

Figure 2.4: Illustration of the flux vortex lattice, the coherence length and the London penetration depth for a superconductor in the mixed state.

expressions involving the kinetic energy, where **A** is the magnetic vector potential.

The central problem of the theory is to find the functions $\Psi(x, y, z)$ and $\mathbf{A}(x, y, z)$ minimizing the free energy for given boundary conditions. In general, the problem is soluble for the limit cases of thick plates or thin films and for weak magnetic fields. In the most general cases the equations are soluble only by numerical means.

The Ginzburg-Landau theory uses another important parameter, the *coherence length* ξ, which describes the typical spatial range within which the superconducting electrons are aware of the existence of each other and modify their behaviour accordingly. In pure metals typical values of ξ are in the order of 10^{-6} m.

In Fig. 2.4 the flux vortex lattice (a), the density of superconducting electrons (b) and the magnetic flux inside the superconductor (c) are schematically shown for a superconductor in the mixed state. Abrikosov [11] showed that the distinction between type-I and type-II superconductors could be put into relation with the ratio between the London penetration depth and the coherence length:

$$\kappa = \frac{\lambda_L(T)}{\xi(T)}. \tag{2.11}$$

Type-I superconductors have $\kappa < 1/\sqrt{2}$, type-II have $\kappa > 1/\sqrt{2}$.

2.3 Flux vortices and dissipative phenomena

Type-II superconductors are characterized, as stated before, by the partial penetration of the magnetic field in the form of flux vortices. The magnetic field acting on the material (either self-generated or externally applied) interacts with the transport current causing energy dissipation. In fact, the Lorentz force $\mathbf{F} = \mathbf{J} \times \mathbf{B}$ tends to make the flux vortices move perpendicular to the current and the field, creating an electric field $\mathbf{E} = \mathbf{v} \times \mathbf{B}$ parallel to $\mathbf{J}$, which gives rise to dissipation. This dissipative mechanism is opposed by the pinning of the vortices in

some energetically favorite zones. The pinning centres can be of different nature, e.g. defects of the lattice, twinning planes or grain boundaries. They can also be artificially created by irradiation and they are responsible for the irreversibility of the magnetic properties in type-II superconductors. As long as the Lorentz force, which is directly proportional to the current density $\mathbf{J}$, is less than the pinning force of the centres, the vortices do not move and no dissipation occurs. The transport capability of the superconductor is therefore linked to the strength of the pinning centres. As a consequence, an ideal superconductor without defects acting as pinning centres would have $J_c = 0$.

The flux vortices can hop out of the pinning centres by thermal activation. For evaluating such effect, the depth U_0 of the potential well of the centres has to be compared with the thermal energy kT. For low-T_c superconductors, the ratio U_0/kT is quite large, so that the vortices are confined in the pinning centres up to temperatures close to T_c. This is not the case for high-T_c materials: the working temperature is much higher, so that for the same pinning energy U_0 the ratio U_0/kT is much smaller.

For giving a more quantitative description of this mechanism, one can suppose that the flux quantum is pinned on the bottom of a potential well U_0. It can hop out of the well by thermal agitation with probability

$$P = \omega_0 \exp(-U_0/kT), \tag{2.12}$$

where ω_0 is the frequency of the hop attempts. Since there is no favorite direction, after a temporal average there will not be any effective movement. In the presence of an external driving force, on the contrary, there will be a privileged direction. In the case of a mono-dimensional problem with triangular potential well, the probability of hopping according or against the driving force is given by

$$P_+ = \omega_0 \exp(-U_0 + \Delta W/kT) \tag{2.13}$$

$$P_- = \omega_0 \exp(-U_0 - \Delta W/kT), \tag{2.14}$$

where ΔW is the energy necessary to bring the vortex from the bottom of the potential well to the nearest equilibrium position.

The effective probability of hopping according to the driving force is given by the difference of the previous two expressions:

$$P^* = 2\omega_0 \exp(-U_0/kT) \sinh(\Delta W/kT). \tag{2.15}$$

When a flux vortex moves with velocity $\mathbf{v}$, it generates an electric field $\mathbf{E} = \mathbf{v} \times \mathbf{B}$. If one supposes that P^* is the same for all the flux vortices, the vortex lattice moves for a distance A_0, so that the modulus of the generated electric field is

$$E = P^* A_0 B = 2A_0\omega_0 B \exp(-U_0/kT) \sinh(\Delta W/kT). \tag{2.16}$$

This electric field is responsible for the energy dissipation. There are two different limit cases:

1. $\Delta W/kT \gg 1$
2. $\Delta W/kT \ll 1$.

The first corresponds to the Thermally Activated Flux Creep (TAFC), characterized by a large driving force and/or low temperature. In this case $P^* \simeq P^+$ and it is possible to show that the flux creep can explain the existence of a line in the $H - T$ plane separating the reversible and hysteretic behaviour. The second corresponds to the Thermally Activated Flux Flow (TAFF), characterized by low intrinsic pinning energies and sufficiently high temperatures, so that the flux vortices can hop out of the well quite easily.

In the TAFC regime, the voltage created by the flux creep mechanism can be written as $V = V_0 \exp(-U/kT)$, where U is the effective energy barrier. Assuming that this quantity decreases with the logarithm of the carried current, one has $U = U_0 \ln(J_0/J)$, where J_0 is the current at which $U = 0$ and depends, in general, on the magnetic field and the temperature. Combining the two relations, one finds

$$\ln V = U_0/kT \cdot \ln I + \text{constant}, \tag{2.17}$$

which justifies the power-law relation used for describing the voltage-current characteristics, see section 2.6. In particular, the power index n results to be linked to U_0, the depth of the potential well of the pinning centres.

2.4 The Bi-2223 system

The family of superconductors includes very different materials, from pure elements to complex ceramic alloys. For large scale application of superconductors, it is necessary that their critical temperature is not too low. In this sense, the discovery of oxide cuprates ($T_c > 30\ K$) in 1986 [1] was fundamental and paved the way for an intense research activity for increasing the temperature limit. One year later, the $YBa_2Cu_3O_{7-x}$ oxide (YBCO), which has a critical temperature of about 92 K, was sintered. With such critical temperature, the liquid nitrogen can be used as cryogenic liquid. With respect to other cryogenic liquids, nitrogen is less expensive (approximately \$0.5 per liter vs. \$5 per liter for helium), easier to handle and has better cooling properties (its volumetric latent heat is 160.6 kJ/dm^3 vs. 2.6 kJ/dm^3 for helium [12]). After the discovery of the Bi-Sr-Ca-Cu-O and Tl-Ba-Ca-Cu-O systems, the highest reproducible critical temperature (156 K) was obtained with mercury-based compounds [13].

For power energy transmission, one of the most promising compounds appeared to be the Bi-Sr-Ca-Cu-O system. This family of superconductors can be expressed by the general formula $Bi_2Sr_2Ca_{n-1}Cu_nO_{2n+4}$, with n=1, 2, 3. The critical temperature of these materials increases with the number of Cu-O planes in the crystalline structure. The compound with only one plane (n=1) has the critical temperature between 7 K and 22 K, depending on the oxygen content. The compound with n=2 has the critical temperature between 50 K and 95 K (again depending on the oxygen content) and is usually referred to as Bi-2212. Both these compounds can be sintered very purely, differently from the compound with n=3, which needs a partial substitution of bismuth with lead to be stable. The critical temperature of this third compound, known as Bi-2223, varies between 105 K and 115 K and has a weak dependence on the oxygen content. Figure 2.5 displays the crystalline structure of Bi-2212 and Bi-2223, which is characterized by a strong anisotropy [14]. The different length between c and a, b axes helps the growth of the grains in the ab plane, giving rise to the typical layered structure of this compound, which is shown in Fig. 2.6. The a and b axes are about 5.4 $\AA$ long in all the compounds of the family, whereas the c axis varies from 24.6 $\AA$ to 30.9 $\AA$ to 37 $\AA$ for n=1, 2, 3, respectively.

2.5 Manufacturing of Bi-2223/Ag tapes

Due to the strong anisotropy of Bi-2223 phase and in order to exploit the favorite transport direction along the Cu-O planes, conductors based on the use of this compound are usually manufactured in the form of flat tapes. The manufacturing procedure, known as Oxide-Powder-In-Tube (OPIT), is based on the following steps:

- Calcination and first chemical reaction of the basic powders.
- Cold deformation of the silver (or silver alloy) tube containing the powders.

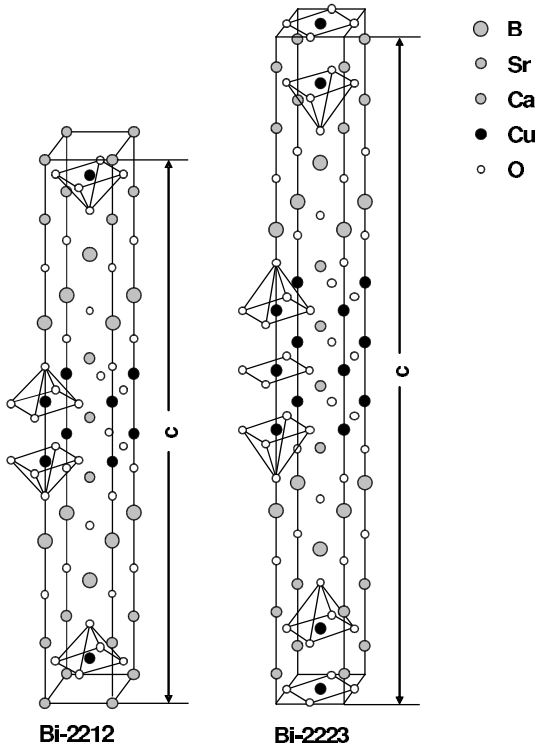

Figure 2.5: Crystalline structure of Bi-2212 and Bi-2223.

- Thermal treatment for the formation of Bi-2223 phase.

The first two steps are schematically shown in Fig. 2.7. The initial calcination of the basic powders has the following purposes:

1. To reduce carbon impurities. It has been observed [15] that the presence of such impurities has a negative effect on the transport properties. During the initial calcination, carbon reacts with oxygen, evaporating as CO_2.

2. To form the Bi-2212 phase as principal phase, which is necessary before the cold deformation.

3. To downsize the dimension of the grains to 2–5 μm. This is the optimal range since larger grains would cause non-uniformities in the tape, whereas smaller ones would adsorb too many impurities from the air.

Before undergoing the thermal treatment, the powders are usually compressed in the form of pastilles in order to better mix up all the ingredients for obtaining a quicker formation of the Bi-2212 phase.

For eliminating the carbon impurities, few calcination processes have to be run, with a final thermal treatment at 820 $°C$: at this temperature the dominating phase is the 2212, whereas the 2223 is absent and will be formed during the final treatment, after the cold mechanical deformation. The so formed 2212 phase already shows an anisotropic structure, which will be increased by the mechanical deformation. Superconducting tapes consist of an internal part, formed by the superconductor, surrounded by normal metal, usually silver or silver alloy. The

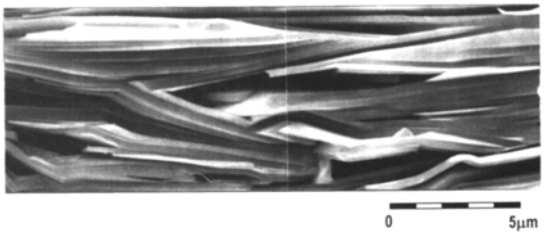

Figure 2.6: Longitudinal section of a mono-filamentary Bi-2223 tape. The layered arrangement of the individual grains is clearly visible.

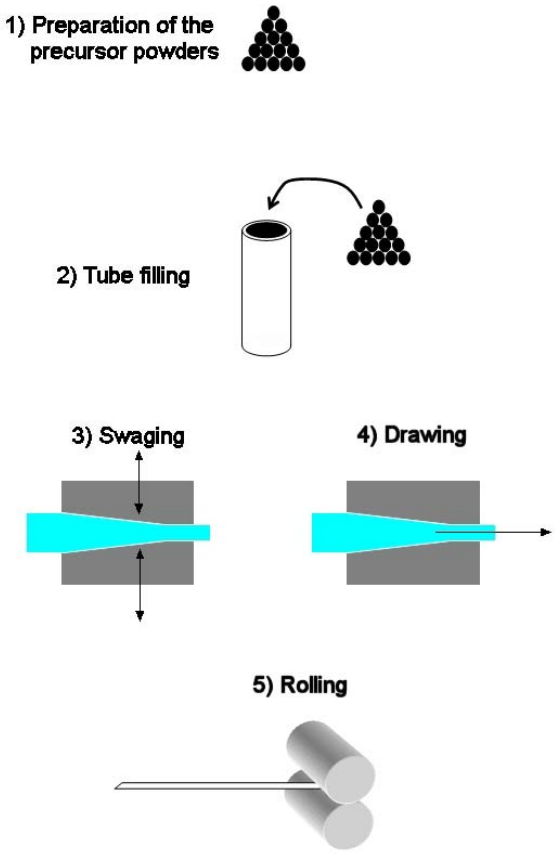

Figure 2.7: Presentation of the first two steps of the OPIT technique.

reason of the choice of the silver lies in the fact that it is very ductile and does not react chemically with the superconducting phase. In addition, it is permeable to oxygen, which can therefore penetrate for forming the superconducting phase with the correct stoichiometry. In order to enhance the resistance to mechanical deformations, silver alloys are usually utilized instead of pure silver. They are characterized by the presence (in the order of few percent) of elements such as manganese, magnesium or titanium, all scarcely reacting with the superconducting phase.

The simplest kind of tapes are the mono-filamentary ones, which consist of a single superconducting core. Unfortunately, they have two great disadvantages, especially for large-scale applications: they are mechanically weak and they have large AC losses. The multi-filamentary tapes, formed by several superconducting filaments embedded in a silver matrix, are mechanically stronger and, thanks to the twisting of the filaments and to the insertion of resistive barriers,

Figure 2.8: Transverse cross-section of a mono- and of a 19-filamentary tape, obtained by scanning electron microscope (SEM). The width is about 2.5 mm, the thickness is about 90 μm and 250 μm, respectively.

Ramp speed ($°C/h$)	Final T ($°C$)	Permanence time (h)
200	600	0
80	750	0
30	815	0
15	832	0
5	837	0
0.5	837.5	50

Table 2.1: Final thermal treatment.

have lower losses in the presence of AC magnetic fields. The typical transverse cross-section of the two kinds of tape is shown in Fig. 2.8.

The OPIT technique is utilized for manufacturing multi-filamentary tapes, too. When the silver tube (with the superconducting core) has been deformed to a sufficiently small diameter, it is drawn through a hexagonal die and cut into several pieces of the same length, which are then assembled in a second silver tube. This assembling procedure is crucial for obtaining a uniform distribution of the filaments. The reason for the hexagonal cross section is that the hexagon is the most regular polygon for covering a circular surface minimizing the voids. The filling-factor does not depend on the number of initial starting wires, provided that they are assembled with a pseudo-hexagonal structure, as displayed in Fig. 2.9. With the "magic numbers" 1, 7, 19, 37, 61, 91, 127, etc., which are given by different m values in the general formula $\sum_{x=1}^{m} 6(x-1)+1$, the filling factor is about 82%. A higher filling factor (about 86%) can be obtained by eliminating the six wires situated in the corners, as in the 55-filamentary tape. Once the multi-filamentary structure has been created, it undergoes a first heat treatment at 600 $°C$ for one hour, for making the softened silver fill the voids. Therefore, a second longer thermal treatment (8–10 hours) has the purpose of soldering the silver of the external tube with the internal wires. After this, the tube is mechanically deformed as in the mono-filamentary case, by means of a drawing and a rolling process. This latter process consists of different steps and must be carried out very carefully. In fact, a too rapid thickness reduction has obvious negative consequences on the tape uniformity; on the other hand, a too slow reduction has negative effects as well, since it would act only on the outer part of the tapes, not aligning the internal grains. Pressing is an alternative technique to rolling: in this case the alignment of the grains is obtained by means of a pressing force in the order of 10 tons. The tapes prepared with the two techniques are called *rolled* and *pressed*, respectively. The final thermal treatment is carried out at a temperature of 837.5 $°C$, which proved to be the optimal one [16] and which is reached in several steps: an example is shown in Table 2.1. After this, the tape is mechanically rolled and finally treated

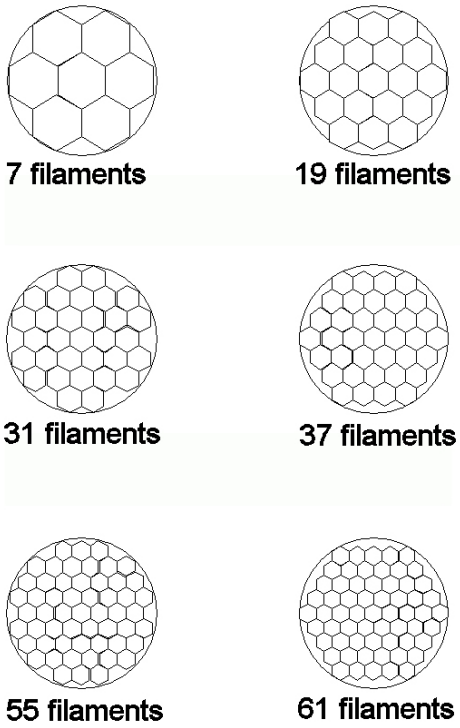

Figure 2.9: Arrangement of the hexagonal wires in the second silver tube for obtaining a multi-filamentary tape. All the configurations have the same filling factor of about 82%, except the 55-filament one, which is about 86%.

at 837.5 $^{\circ}C$ again, but for a longer interval, about 100 h. The final thermal treatment lasts therefore about 150 h.

2.6 Characterization of Bi-2223/Ag tapes

The fundamental quantity characterizing Bi-2223/Ag tapes is the *critical current*, i.e. the maximum transport current the tape can carry without dissipation (in DC). It can be determined by measuring the voltage between two contacts situated on the tape transporting the current. Usually the critical current I_c is defined as the value at which a voltage corresponding to a critical electrical field $E_c = 10^{-4}\ V/m$ is reached, as displayed in Fig. 2.10.

For $V - I$ measurements, the transition from superconducting to normal state can be described by a simple non-linear power-law

$$V = V_c(I/I_c)^n, \tag{2.18}$$

where the power index n defines the steepness of the transition and usually varies between 10 and 30. In general, the higher the n value the better the sample, because with a steep transition the tape can carry a current very close to I_c generating a very low voltage. For numerical modelling of HTS materials, a local constitutive relation of the material is needed, so that the power-law

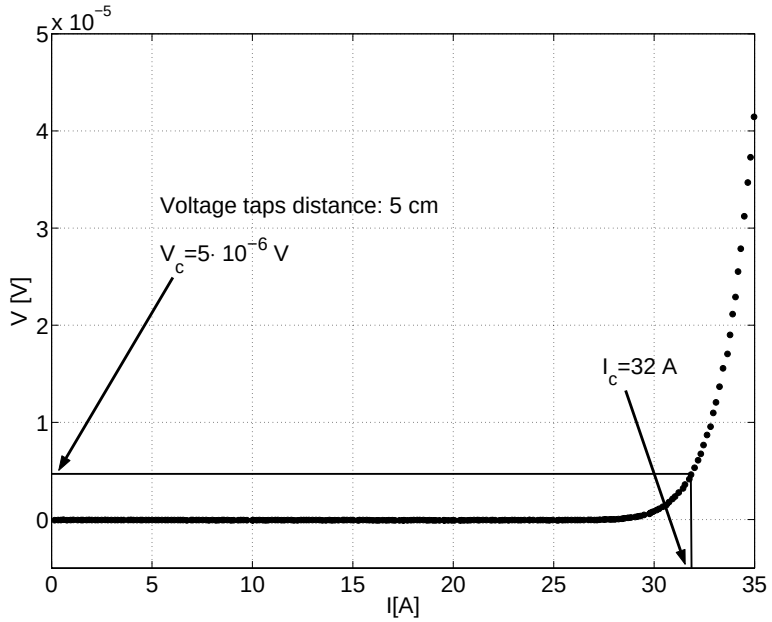

Figure 2.10: Determination of the critical current from voltage-current measurements.

(2.18) is rewritten in terms of the electric field and of the current density:

$$E = E_c(J/J_c)^n. \tag{2.19}$$

At this point a remark is necessary about the meaning and the link between the critical current and the critical current density. The critical current I_c is a *global* property, which describes the transport capacity of the tape averaged on all the internal current paths. From the finite element method point of view, the superconductor needs to be described by a *local* property J_c. In this context, "local" means that it is defined at every point of the discretized geometry, without taking into account the microstructure. The critical current density J_c is a local parameter (varying for example with the position inside the tape or according to the the magnetic field experienced by the material), which cannot be determined by the (global) measured I_c. This means that the relation $J_c = I_c/S$, where S is the superconducting section of the tape, is in general not true, due to the local variations of J_c inside the tape.

Chapter 3

Finite element method modelling of superconductors

The transport properties of HTS are strongly related to their microstructure and to the manufacturing process. As a consequence, their performance is influenced, even drastically, by geometrical and physical effects. For example, by the position and the orientation of the filaments inside the tape; or by the magnetic field, which can strongly decrease the transport capacity of the superconductor.

From the modelling point of view, this means that for obtaining a sufficiently accurate description of the electromagnetic behaviour, the developed models must take into account the internal structure of the devices (tapes, wires, cables), whereas a macroscopic description is more useful to solve problems on a larger scale (e.g. a grid of superconducting devices).

This chapter firstly illustrates the critical state model (CSM), which gives a qualitative description of the behaviour of superconducting materials. The fundamental assumptions and the limits of such model are pointed out. Secondly, the finite element method (FEM) technique is introduced. The most important steps in the construction and the solution of a FEM problem are discussed. The formulations used to solve Maxwell's equations with the software package FLUX3D are described.

3.1 The critical state model

Several models exist for calculating current/field distributions and evaluating the AC losses of superconductors in different working conditions. The simplest and most widely known is the critical state model (CSM), originally proposed by Bean in the early sixties [17, 18], which is based on the assumption that the current density inside superconductors is either zero or equal to $\pm J_c$, in the regions where the magnetic field is zero or different from zero, respectively. The critical current density J_c is considered independent of the magnetic field. In the framework of the power-law description of the superconducting transition, the critical state model corresponds to a power index $n = \infty$. This model, even if very simple, is sufficiently accurate for describing superconductors with a very steep transition to the normal state, for example low-T_c superconductors, which typically have n-factors larger than 50. This is not the case for HTS materials, which present a smoother transition: in this case, the critical state model can be used for a qualitative description only.

The critical state model allows to find analytical solutions for the current distribution inside conductors in few cases, where the geometry is simple and often involves infinity approximations, as in the case of the slab and strip.

Figure 3.1 illustrates the critical state model in the case of a slab in parallel applied magnetic field. A slab is a parallelepiped with two dimensions much larger than the third. Shown in the

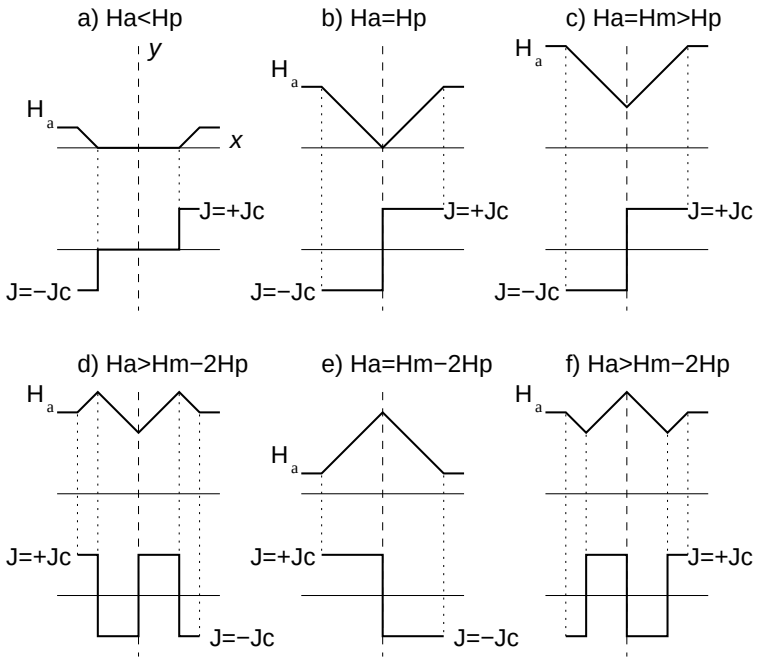

Figure 3.1: Magnetic field and current density profiles in a superconducting slab according to the CSM model.

figure are the profiles of the magnetic field and of the current distribution along the x-axis of a slab of width $2a$ with infinite length along the y- and z- directions. The magnetic field is applied along the y-direction.

Let the magnetic field be of amplitude H_a and let it start to increase. Screening currents will be induced at the edges of the slab, with a direction such as to oppose the variation of the field and to screen the interior of the slab. In the illustrated case, the field has only the y-component and the curl of **H** in Ampere's law is reduced to a scalar term. In particular, the field profile inside the slab is a straight line with slope

$$\partial H_y/\partial x = \pm J_c. \tag{3.1}$$

The field will partially penetrate the slab and in the penetrated region the current density will be $\pm J_c$, as indicated in Fig. 3.1a. This will continue up to a certain value H_p of the applied field, when the flux penetrates to the centre of the slab and each half width of the slab carries a current density $\pm J_c$, respectively, see Fig. 3.1b. The value H_p is referred to as *penetration field*. When the external field has an amplitude larger than H_p, the screening currents' density cannot exceed J_c (according to the model) and cannot oppose any longer to the field penetration inside the superconductor. The field pattern will simply shift upwards, see Fig. 3.1c, the difference between the value of the field at the edge and at the centre remaining constant and equal to H_p.

Let now the external field start to decrease. The screening currents oppose this variation and areas with inverted current will appear near the edges of the slab. In the rest of the slab nothing changes, see Fig. 3.1d. When the magnetic field has decreased by $2H_p$ from its peak value, the field and current patterns have completely reversed, see Fig. 3.1e. When the external magnetic field starts to increase again, new regions with inverse current will appear at the edges, see Fig. 3.1f. The most important result of this simple analysis is that once the field has penetrated the slab (partially or completely), there always exist screening currents in the superconductor, even when the external field passes through zero during its oscillations. This means that the superconductor has a *hysteretic* behaviour.

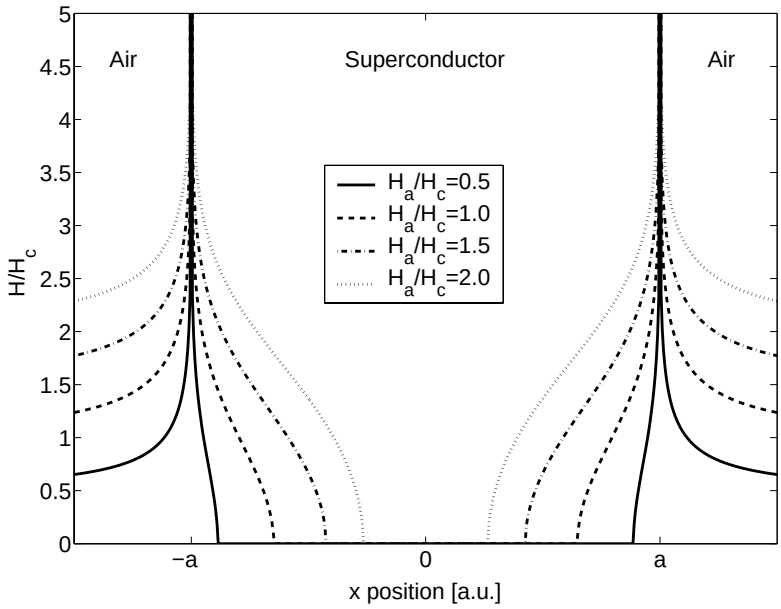

Figure 3.2: Magnetic field profile in a strip of width $2a$ for different amplitudes of the magnetic field ($H_c = J_c/\pi$), computed according to Brandt's theory.

Another peculiar geometry for which analytical solutions exist is the strip, i.e. a rectangle of width $2a$, infinitesimal thickness and infinite length. The solutions for the current and field distributions with applied transport current and/or perpendicular magnetic field have been obtained by Brandt and Indenbohm [19], with the assumption of a constant J_c.

With respect to the CSM applied to the slab geometry, two are the most important differences: firstly, the screening currents flow along the entire width of the specimen, even if the flux penetration has not reached the centre yet. Secondly, the shape of the penetration profile along the x-axis is no longer linear, but rather quadratic. An example of the magnetic field distribution in the strip, computed by Brandt, is given in Fig. 3.2. It is interesting to note that, due to the strong demagnetizing effect, the magnetic field at the superconductor-air interface ($x = \pm a$) is much higher than the applied one. This will be confirmed by FEM simulations and discussed in chapter 6.

3.2 Finite element method modelling

The critical state model and the analytical solutions found by Brandt deal with peculiar geometries, such as slabs and strips, which in most cases are very far from the actual structure of the superconducting devices. The computations based on the finite element method (FEM) technique are a reliable tool for investigating current and field distributions in complex geometries. FEM computations are used to solve a wide class of problems, involving different physical effects. In general, this technique consists in drawing the geometry of the problem, dividing it in many discrete elements and solving the corresponding set of differential equations for each element. The main advantage is that the physical quantities can be locally calculated and the obtained results are therefore very precise. In the case of superconductors, the set of differential equations is given by Maxwell's equations, appropriately written in order to take into account the non-linear $E - J$ relation of HTS materials.

The FEM technique has been and is currently used for investigating the current and field

distributions inside superconductors. Most of the groups use homemade codes (see for example [20],[21]). These codes usually require a long time to be developed and cannot be utilized by other users. This is the reason why the use of a commercial software package, with hundreds of users around the world, has been preferred.

In this thesis work, the FEM software package FLUX3D, developed by the French company Cedrat[1], has been used. This software package was originally created and developed for solving general electromagnetic problems (e.g. motors, magnets, transformers, etc.). Recently [22], as the result of a collaboration between Cedrat and the Swiss Federal Institute of Technology - Lausanne, the 2D version of the software, FLUX2D, has been equipped with a module for superconductors, which is now available in the commercial versions of FLUX2D-FLUX3D. Details on the use of the software package can be found in the user's guides published by Cedrat. A very well documented description of the 3D formulation, with particular attention to the problem of the coupling with circuit equations can be found in [23].

It is beyond the purpose of this thesis to give a detailed description of the finite element method technique, which can be found in dedicated books. Listed below are simply the basic steps for solving a FEM problem with FLUX3D:

1. To draw the geometry to be simulated with a CAD-like interface.
2. To mesh the geometry.
3. To choose an appropriate physical model, assigning the desired boundary conditions.
4. To define the materials and to assign them to the geometrical regions.
5. Eventually, to draw an electric circuit and to couple it with the appropriate geometrical regions.
6. To set the solving parameters. For transient problems, to choose the desired time interval and the time steps. To solve the problem and to analyze the results.

3.2.1 Drawing the geometry

The first step in a FEM problem is constructing the geometry, which is made by using a CAD-like interface. The first thing to be created is the domain, which can be different according to the type of problem to be simulated. Contrary to other domains of physics (i.e. mechanics), the physical quantities of electromagnetism are not zero in air or in vacuum, so that it is necessary to "model the infinity". The finite element method is based on the meshing of a complete study domain with finite elements, which makes it impossible to model the infinity by classical finite elements (contrary, for example, to the boundary integral equations method). The solution is to simulate the infinity with a sufficiently large air box, so that the effects of the infinity approximation with a closed and remote boundary can be considered negligible. Typically, an air box at least 10 times larger than the simulated geometry has been utilized. The disadvantage of such approach is the cost in terms of nodes, but their number can be reduced with an appropriate choice of the mesh, see for example Fig 4.18.

The eventual presence of symmetries and/or periodicities has to be taken into consideration during the definition of the domain properties. Then, the coordinate system has to be defined: for complex geometries, it is useful to use local coordinate systems. After that, one can create the geometrical points, connect them with the lines, construct the faces and the volumes. In general, for creating the points it is preferable to use parameterized coordinates, so that the geometry can be successively modified without too much effort. Especially for the creation of

[1]Chemin de Pré Carré, Zirst 38246, MEYLAN Cedex, France. http://www.cedrat.com

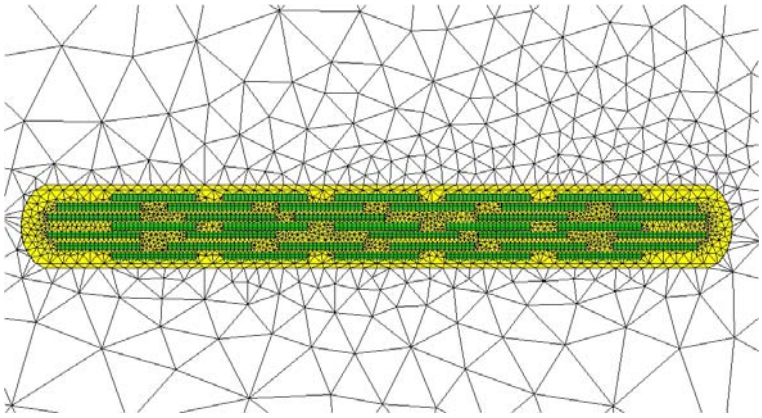

Figure 3.3: Mesh of a 37-filamentary tapes. A mapped mesh (20×3) has been used in each superconducting filament.

the volumes, it is particularly useful to use geometrical transformations: this allows, for example, to propagate the mesh properties of the initial 2D geometry along the corresponding volume.

3.2.2 The mesh

The mesh is the key-point of FEM computations. For obtaining detailed results it has to be fine enough, yet without increasing too much the size of the problem and, consequently, the computation time. The mesh density must be assigned by distinguishing the regions where there are rapid spatial variations of the variables and where one is interested in having detailed results from those where a precise description is not required. For example, it is not interesting to know precisely the spatial distribution of the magnetic field in the air very far from the simulated device; therefore, in that region it is not necessary to put many mesh points. On the contrary, the magnetic field can vary drastically at the material interfaces, so that the mesh density must be concentrated there. Usually the regions where one wants to obtain detailed results are assigned a *mapped* mesh, i.e. a mesh composed by rectangular elements, which divide the region into a regular grid. The other regions are meshed "automatically" with triangular elements.

For the mesh of the volumes, it has been recently introduced the possibility of meshing the volume according to the geometrical transformation used to create the volume itself. In this way, the mesh assigned to the initial 2D geometry is automatically extruded during the creation of the volume. Compared to the "normal" way of meshing the volumes (i.e. constructing first the volumes and then assigning the mesh), this way is faster and allows to obtain a more regular mesh. This mesh tool is particularly useful in the case of twisted volumes: an example is reported at the end of chapter 4. Figure 3.3 provides an example of the mesh for a 37-filamentary tape in 2D. The superconducting filaments are assigned a mapped mesh.

3.2.3 The physical model

In FLUX3D different physical models are available, according to the type of problem to be solved. In this thesis, the behaviour of HTS devices in AC regime has been investigated, so that a transient 2D or 3D formulation has been used.

Different physical formulations can be used for solving Maxwell's equations in the simulated domain and computing the desired electromagnetic variables [24]. In particular, there exist the $\mathbf{A} - V$ and the $\mathbf{T} - \Phi$ formulations, the names referring to the electromagnetic potentials used as state variables.

The $\mathbf{A} - V$ formulation uses the magnetic vector potential $\mathbf{A}$ (defined by $\mathbf{B} = \nabla \times \mathbf{A}$) and the electric scalar potential V.

The electric field is expressed as

$$\mathbf{E} = -\frac{\partial \mathbf{A}}{\partial t} - \nabla V \tag{3.2}$$

and the general equation to be solved is Ampere's law:

$$\nabla \times \frac{1}{\mu_0} \nabla \times \mathbf{A} + \sigma(\frac{\partial \mathbf{A}}{\partial t} + \nabla V) = 0. \tag{3.3}$$

In the superconducting regions, σ is a non-linear conductivity describing the transition from superconducting to normal state, see Eq. 3.6.

The $\mathbf{T} - \Phi$ formulation uses the electric vector and magnetic scalar potentials, defined by $\nabla \times \mathbf{T} = \mathbf{J}$ and $\mathbf{H} = \mathbf{T} - \nabla\Phi$, respectively.

With the use of the constitutive equation $\mathbf{B} = \mu_0 \mathbf{H}$ (see also Fig. 3.5), Faraday's and Gauss' laws to be satisfied are re-written as follows:

$$\nabla \times \mathbf{E} = -\frac{\partial \mathbf{B}}{\partial t} \quad \Longleftrightarrow \quad \nabla \times \mathbf{E} + \frac{\partial}{\partial t}(\mu_0(\mathbf{T} - \nabla\Phi)) = 0 \tag{3.4}$$

$$\nabla \cdot \mathbf{B} = 0 \quad \Longleftrightarrow \quad \nabla \cdot (\mu_0(\mathbf{T} - \nabla\Phi) = 0. \tag{3.5}$$

In order to assure the uniqueness of the solution of Eqs. 3.4-3.5, a gauge condition $\nabla \cdot \mathbf{T} = 0$ is also added [25].

The $\mathbf{A} - V$ formulation is usually utilized for solving two dimensional problems, where the conductors' length is considered infinite and only the transverse cross-section is analyzed. The boundary conditions are assigned on the lines composing the domain boundary. For 2D problems, the magnetic vector potential has only one component, A_z. For the self-field case, when no magnetic field is externally applied, the condition $A_z = 0$ is assigned on the whole boundary. On the contrary, for imposing a given uniform magnetic field, the appropriate value of $\mathbf{A}$ has to be chosen, taking into consideration that the relation $\mathbf{B} = \nabla \times \mathbf{A}$ is reduced to $B = \Delta A_z / d$, where ΔA_z is the difference between the value of A_z on two sides of the boundary and d is the distance between the sides. This is schematically shown in Fig. 3.4. For example, for imposing a vertical sinusoidal field, the conditions $A_z = \pm A_0 sin(\omega t)$ on the two vertical sides and $A_z = 0$ on the two horizontal ones have to be applied. The resulting magnetic field is $B_y = 2A_0/d \; sin(\omega t)$.

The $\mathbf{T} - \Phi$ formulation is mostly utilized for three-dimensional problems in applied magnetic field. Recently, it has been refined into a new $\mathbf{T} - \mathbf{T_0} - \Phi$ formulation [26], which can handle 3D problems coupled with circuit equations, i.e. with the possibility of imposing a transport current. $\mathbf{T_0}$ is an auxiliary potential, which is used to impose the desired current flowing through the conductor. The validation of this new formulation and the results on typical 3D geometries are described at the end of chapter 4.

3.2.4 The materials and the geometrical regions

Superconducting materials are described by a non-linear resistivity derived by the power-law $E - J$ relation[2]:

$$\rho(\mathbf{E}) = \frac{1}{\sigma(\mathbf{E})} = \frac{E_c^{1/n}}{J_c} |\mathbf{E}|^{(n-1)/n} + \rho_0. \tag{3.6}$$

[2]The soundness of the use of a resitivity without upper limits, as the one given by Eq. 3.6, is discussed in appendix A.

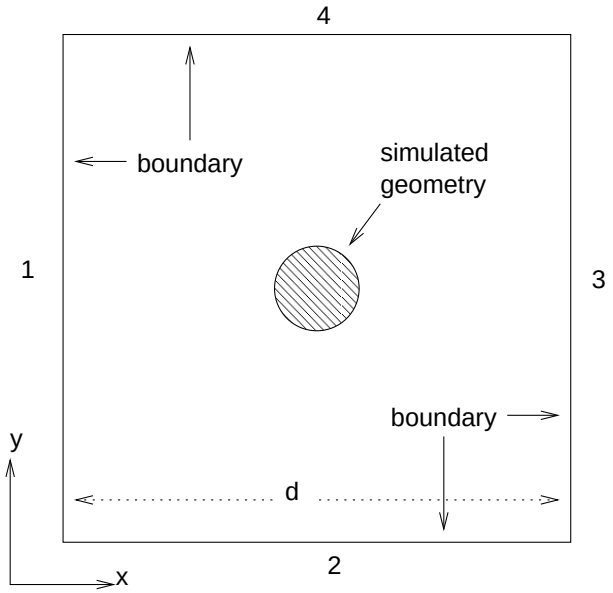

Figure 3.4: Application of boundary conditions in a 2D square domain with $\mathbf{A} - V$ formulation. For producing a uniform vertical AC magnetic field, the condition $A_z = \pm A_0 sin(\omega t)$ has to be imposed on the boundary lines 1 and 3, respectively. On the lines 2 and 4, the condition $A_z = 0$ is imposed.

The parameter ρ_0, which has been added in order to avoid numerical divergences when the electric field is zero, is very small (between 10^{-15} and 10^{-14} $\Omega \cdot m$), it does not influence the numerical results and can be physically interpreted as the term corresponding to the residual resistance of the superconductor [27].

Therefore, the electrical properties of HTS materials are defined by four parameters: the critical current density J_c, the power index n, the critical electrical field E_c and the residual resistivity ρ_0.

The other constitutive equation for HTS materials is the relation between $\mathbf{B}$ and $\mathbf{H}$. The relation

$$\mathbf{B} = \mu_0 \mathbf{H} \tag{3.7}$$

proved to be a good approximation for type-II superconductors, provided that $H > H_{c1}$, which is always the case for practical applications (see Fig. 3.5 and [28] for further details). The normal metal composing the matrix of the tapes is defined by a constant conductivity σ (usually $5 \cdot 10^8$ S/m for silver at 77 K), whereas the air surrounding the device is defined as an insulator.

The different parts of the geometry have to be assigned to geometrical regions, which can be surface (2D) or volume regions (3D). Each of them is assigned the corresponding material. For example, in a multi-filamentary tape, all the filaments usually constitute one single region, whose properties are described by the superconducting material. On the contrary, if one has to simulate regions with different superconducting properties, the use of different geometrical regions is necessary. An example with two different superconducting regions is the square wire described in paragraph 4.3.2. Finally, the coupling with the electric circuit is made in terms of geometrical regions and not in terms of surfaces or volumes.

3.2.5 Coupling with circuit equations

In order to impose a given transport current flowing through a device, the FEM geometry has to be coupled with circuit equations. In the FEM software, the circuit is drawn separately

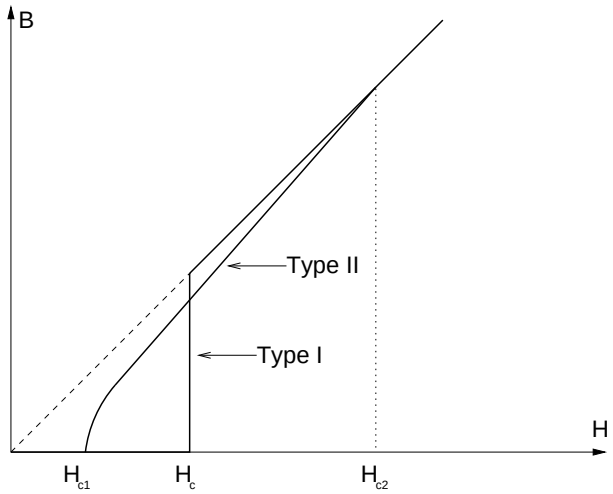

Figure 3.5: Typical $B - H$ characteristic for type-I and type-II superconductors. Due to the small value of H_{c1}, the approximation $B = \mu_0 H$ can be considered valid for all the practical applications with type-II superconductors.

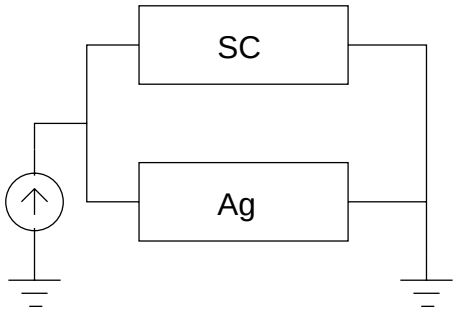

Figure 3.6: Electrical circuit for a HTS tape. The superconducting and silver regions are assigned to two parallel massive conductors. A voltage or current source can be used to inject the transport current.

and it is in general composed by a current/voltage source, different massive conductors and, eventually, other circuital elements (resistances, capacitances, inductances, etc.). Then, the massive conductors are assigned to the corresponding geometrical regions and finally the entire structure is meshed for coupling the geometrical/physical description with the electrical one.

As an example, one can consider a HTS tape, carrying a transport current injected by a current source. From the electrical point of view, the tape can be modelled as two resistances in parallel: one of them, the normal metal matrix, is determined by the (constant) resistivity of the metal at a given temperature and by the geometry; the other one, the superconducting part, is varying and its value depends on the current flowing through it. In the electrical circuit model, two massive conductors are drawn and assigned to the superconducting and normal metal regions, as displayed in Fig. 3.6.

3.2.6 Solving parameters and post processing

Another important step in the solution of a FEM problem is the setting of the solving parameters. First of all, for transient problems one has to choose the length of the simulated time interval and to divide it in time steps. Usually, for AC problems two cycles have been simulated and

the second has been used to evaluate the current and field distributions and to compute the AC losses. In fact, the first cycle contains some transient terms due to the initial conditions and cannot be used to evaluate the physical quantities in the steady state.

The time interval is divided into many time steps: the division must be sufficiently fine for avoiding the divergence of the algorithm, yet keeping the computation time to a reasonable value. Usually the two cycles have been divided into 200 linear time steps. It has to be mentioned that for certain simulations, such as the application of a magnetic field ramp at high frequency, it is preferable to use a logarithmic division of the interval, with the points concentrated in the initial part.

Other options allow to choose the linear and non-linear solvers and to fix their parameters (tolerances, number of iterations, etc.), which may influence the accuracy and the speed of the solution. More details about the Newton-Raphson algorithm used for solving the system of non-linear equations are given in appendix B.

The solution of each time step can be saved in a separate file for post processing. In the case of huge problems (involving 3D geometries and/or very fine mesh), it is in general preferable to save the results of only few particular time steps (e.g. $\omega t = \pi/2$, $\omega t = \pi$ etc. in AC regime) for reducing the total space of the problem on the disk. Nevertheless, the temporal evolution of quantities such as the transport current or the AC losses can be calculated during the solving process and stocked separately, with no need of saving the entire solution of each time step.

Chapter 4

FEM analysis of Bi-2223 conductors with transport current

This chapter is mainly dedicated to 2D finite element method modelling of Bi-2223/Ag tapes and wires. Firstly, the current and field distributions and the AC losses are calculated for a 37-filamentary tape. The results are discussed and compared with the ones previously obtained with FLUX2D. A comparison with a numerical method originally formulated by Brandt is also given. Secondly, a non-linear power-law with non-constant J_c and n parameters is implemented in FLUX3D. In particular, J_c and n depend on the lateral position inside the tape and on the magnetic field experienced by the superconductor. It is shown that these dependencies lead to a significative reduction of the transport capacity of the tapes and to an enhancement of their AC losses. Therefore they must be taken into consideration for a more precise evaluation of the performance of HTS devices. Finally, a recently developed 3D formulation coupled with circuit equations is validated and tested on typical 3D geometries.

4.1 Comparison with other numerical methods

The software package FLUX3D has been utilized for the first time at LANOS within this thesis work. In order to test its efficiency, some results have been compared with the ones obtained with FLUX2D, another FEM software package already in use at LANOS. The calculations made with FLUX2D, having already been successfully compared with experimental measurements [22, 28], have been used as reference.

In this thesis work, FLUX3D has been chosen because it presents two main advantages with respect to FLUX2D. First of all, as suggested by the name, it can solve 3D problems: for some geometrical configurations (e.g. twisted or corner shaped conductors) or for studying effects involving a finite third dimension (e.g. coupling effect between filaments), the 2D approach is not sufficient. Secondly, for imposing a transport current through conductors, a voltage or current source can be alternatively used, which is not possible with FLUX2D (only voltage source). The use of a current source is more practical, because the desired transport current can be directly imposed, instead of looking for the corresponding voltage amplitude, which depends on the physical and geometrical parameters of the simulated problem. In addition, FLUX3D has improved tools for the post processing.

Despite the similarity in the name, FLUX3D works in a quite different way from FLUX2D, so that a first validation of the obtained results was necessary. For comparing the results obtained with the two software packages, the problem of a 37-filamentary tape has been simulated (in 2D), both in self-field and in externally applied AC magnetic field. The current and field distributions and the AC losses in the superconductor have been compared. With FLUX3D both a voltage and a current source have been used. Both FLUX2D and FLUX3D use the $\mathbf{A} - V$ formulation,

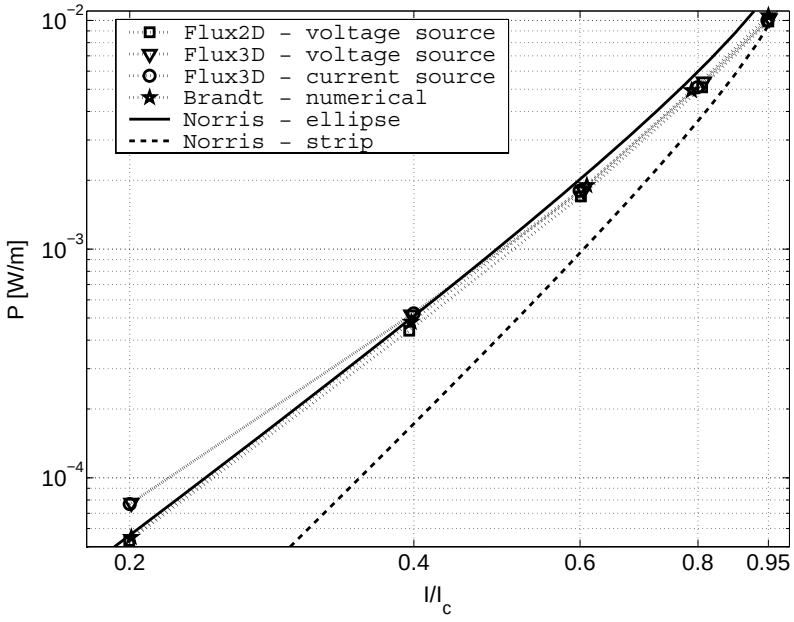

Figure 4.1: AC losses in self-field as a function of the normalized transport current, computed by the different models.

which has been described in paragraph 3.2.3. The results have also been compared with the ones obtained by an analytical model, based on the original formulation by Brandt [29] and integrated with the insertion of the power-law (2.19) [30].

The simulated tape has outer dimensions of 3.0 $mm \times 0.36$ mm, $I_c = 40$ A, $J_c = 108$ A/mm^2, $n = 15$. Different amplitudes of the transport current for the current source model (FLUX3D) at 59 Hz have been used: from 8 A to 38 A, which correspond to the range from $0.2I_c$ to $0.95I_c$. In the voltage source models (FLUX2D, FLUX3D, Brandt) the voltage gradients have been chosen so that to produce the same transport currents.

Figure 4.1 displays the self-field AC losses in the superconductor for the different models, computed according to the following expression:

$$P = f \int_T \int_S \mathbf{J} \cdot \mathbf{E} \; dS \; dt, \tag{4.1}$$

where $f = 59$ Hz is the frequency of the source, T is the second simulated period (for avoiding transient terms) and S is the cross-section of the superconductor.

Reported are also the theoretical predictions, based on the CSM, made by Norris for superconductors with elliptical and strip cross-section [31]:

$$P = \frac{f {I_c}^2 \mu_0}{\pi} \times \begin{cases} (1-i)\ln(1-i) + (2-i)\frac{i}{2} & \text{ellipse} \\ (1-i)\ln(1-i) + (1+i)\ln(1+i) - i^2 & \text{strip,} \end{cases} \tag{4.2}$$

where $i = I/I_c$ is the amplitude of the transport current normalized to the critical value.

The results from the different models are very similar, all falling close to the elliptical prediction: in fact, the ellipse is a better approximation of the actual structure of the considered multi-filamentary tape than the strip. The self-field AC losses are proportional to $i^{3-3.5}$. A good agreement among the models has been observed for the current density distributions, too. An example is given in Fig. 4.2, which displays the distribution of the current density at $\omega t = \pi$

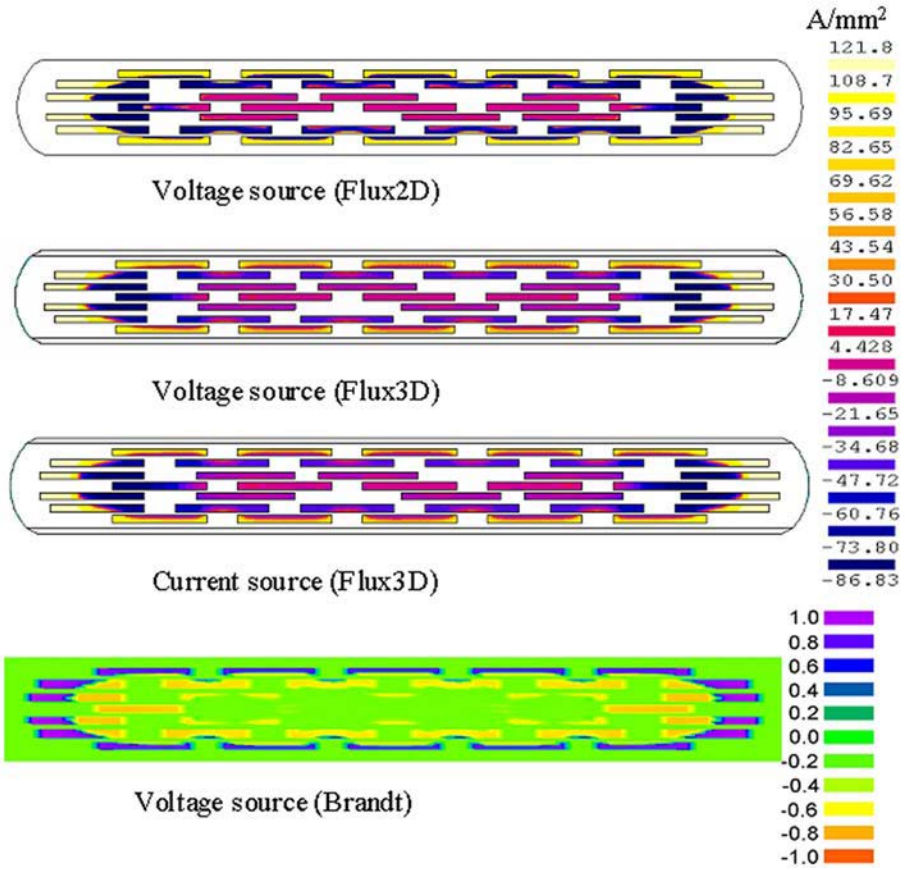

Figure 4.2: Current density distribution at $\omega t = \pi$ and $I = 0.6 I_c$ computed by the different models. The critical current density is 108 A/mm^2. The grey scale for the Brandt method is normalized with respect to the extreme values.

and $I = 0.6 I_c$. At this particular instant ($\omega t = \pi$), the integral of the current density over all the section is zero, but the current density varies between positive and negative values. In particular, the outer filament layer carries positive current and gets saturated: even if the total applied current is well below I_c, the current density locally exceeds J_c (108 A/mm^2). The inverse current is carried by the inner filaments, which do not saturate completely, even at $I \sim I_c$. The central filaments are current free, and this happens up to $I < 0.8 I_c$. Figure 4.3 contains the same kind of plot as Fig. 4.1, but for applied AC magnetic field, parallel to the wide side of the tape, with amplitude 3 mT and 70 mT. The losses for $B = 3$ mT are very close for the four models. They are higher than the self-field ones and are proportional to i^2. This means that the applied magnetic field has smoothed the dependence of the losses on the transport current. The losses for $B = 70$ mT, computed by FEM simulations, practically coincide and are lower than the ones computed with Brandt's method by about 10%. At such value of B, the magnetic field has completely penetrated the superconductor and the magnetization losses are the dominant term. This is the reason why the losses are almost independent of the applied transport current.

The current density distributions for $I = 0.6 I_c$ at $\omega t = \pi$ and external field $B = 0$ mT, 3 mT, and 70 mT are shown in Fig. 4.4. The applied AC magnetic field generates screening currents, which try to avoid the penetration of the field inside the tape. With a field applied parallel to the wide face of the tape, these screening currents flow in opposite directions in the top and in the bottom halves of the tape. Therefore, the total current through the cross section, which is a superposition of the transport current and of the induced screening current, has an

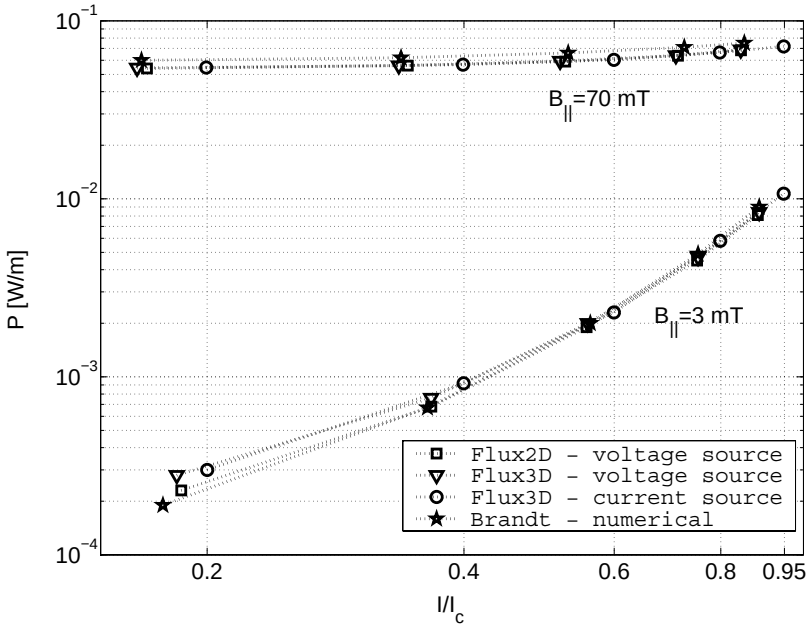

Figure 4.3: AC losses in applied parallel field as a function of the transport current, computed by the different models.

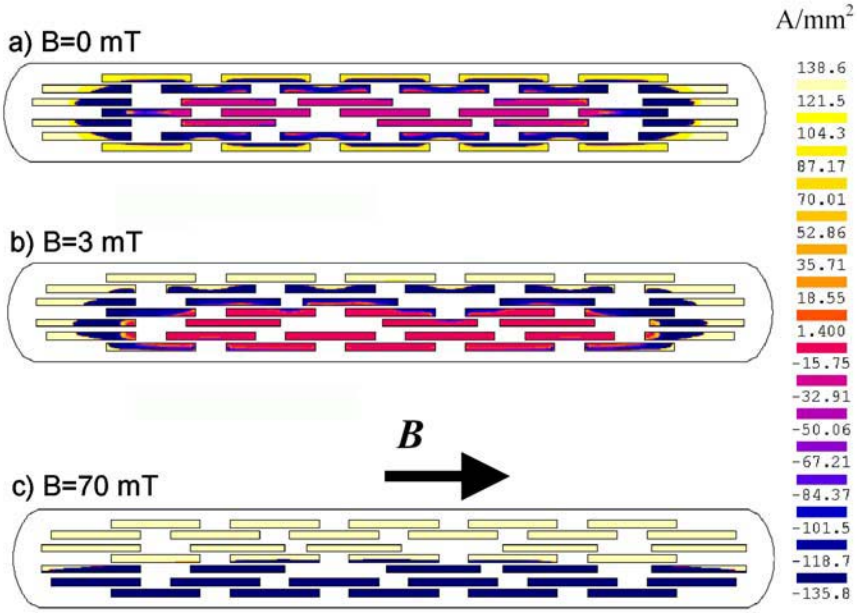

Figure 4.4: Current density distribution at $\omega t = \pi$ and $I = 0.6 I_c$ in self and applied field (3 mT and 70 mT). The critical current density is 108 A/mm^2.

asymmetric pattern with respect to the line dividing the tape into two halves along its width, see Fig. 4.4b. At high applied magnetic fields, the induced currents dominate the transport ones and the pattern is symmetric again. In this case the current density exceeds J_c in all filaments,

see Fig. 4.4c.

Finally, it is interesting to note that in Fig. 4.3 the losses have been computed at different values of the transport current. In fact, for the models with voltage source, the voltage gradient has been kept the same as in the self-field case. On the other hand, the induced currents decrease the transport-current capacity of the superconductor, which results in a lower effective transport current. For this reason, the points corresponding to the voltage source models are situated to the left (i.e. at lower transport current) of the ones for the current source model, yet on the same loss curves.

4.2 Lateral position dependence of J_c and n

There is certain experimental evidence that, due to several factors in the manufacturing process, the critical current density J_c and the power index n are not homogeneous along the width of multi-filamentary Bi-2223 tapes. Among the main factors causing such effect there are the non-uniform rolling process and uneven oxygen diffusion in the different filaments [32].

The internal distribution of J_c and n can be determined by the strip-cutting technique [33] or by non-destructive methods, such as the scanning Hall probe microscopy [34], the magnetization hysteresis loop [32] or the magnetic field gradient [35]. Despite some contradictory results, it has been demonstrated that the central filaments have a better alignment of the grains, resulting in a higher critical current density and n factor than the outer filaments. The variation of J_c from the centre to the periphery reaches a factor of 2-3.

The dependence of J_c and n on the lateral coordinate x has been derived from experimental data provided by Nordic Superconductor Technology. The adopted technique consisted in incrementally cutting off a multi-filamentary tape from one edge to the other by a high precision dimpling instrument. Before and after each cut, the DC voltage-current characteristics have been measured. The corresponding values of I_c and n along the width have been obtained from the measured $V - I$ curves. The local critical current densities have been determined after electronic scanning of the remaining section of the tapes. Figure 4.5 shows the obtained lateral distribution of J_c and n, normalized by the values at the centre of the tape, J_{c0} and n_0, respectively. Both the quantities are highest in the central filaments and lowest in the outer ones: the variation reaches a factor of 3.3 and 1.5, respectively.

In order to introduce the $J_c(x)$ and $n(x)$ dependence in FLUX3D, the experimental data have been fitted with a continuous Gaussian model, as follows:

$$J_c(x)/J_{c0} = e^{-x^2/1.6^2} \tag{4.3}$$

$$n(x)/n_0 = 0.4 + 0.6e^{-x^2/1.8^2}, \tag{4.4}$$

where the values of x (distance from the centre of the tape) are in mm. The fit of the experimental measurements is displayed in Fig. 4.5.

The implementation of Eqs. 4.3-4.4 into FLUX3D has been made with an external Fortran subroutine, where J_c and n can be defined as x-dependent. This means that the local values of J_c and n are calculated at each FEM node according to the position inside the tape. The FEM simulations have been performed on a 19-filamentary tape, with $I_c = 36.6\ A$. With the constant J_c model, this critical current is obtained by using $I_c = J_c \times S$ with $J_c = 7.13 \cdot 10^7\ A/m^2$; with the $J_c(x)$ model, by integrating $J_c(x)$ along the tape width with $J_{c0} = 1.06 \cdot 10^8\ A/m^2$.

Due to the symmetric arrangement of the filaments inside the tape, only one fourth of the real geometry has been simulated, in order to reduce the computation time and the size of the problem on the disk. Symmetry conditions of normal magnetic field have been applied on the symmetry lines of the geometry, i.e. the x- and y-axis, see Fig. 4.6 for reference. The figure displays the instantaneous power loss density in each filament for an applied transport current

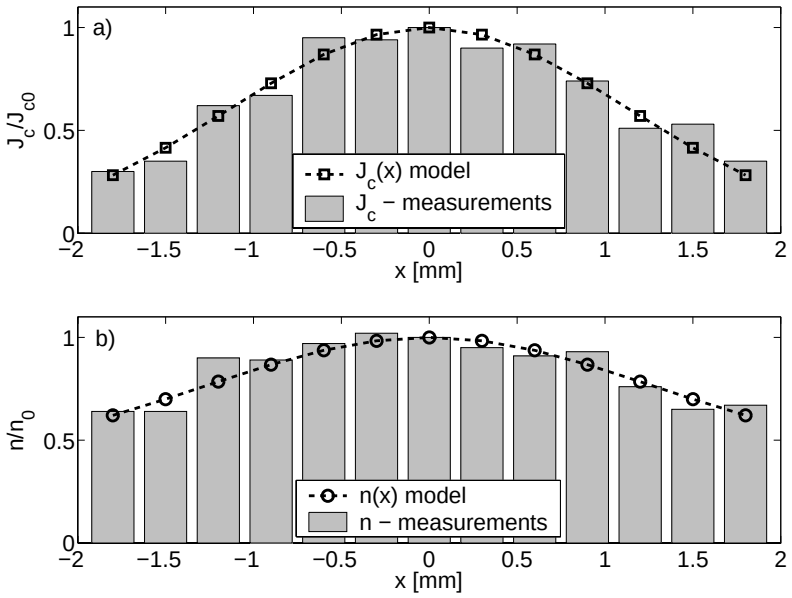

Figure 4.5: Normalized lateral distributions of J_c (a) and n (b) obtained from measurements and the Gaussian-type models from Eqs. 4.3 and 4.4.

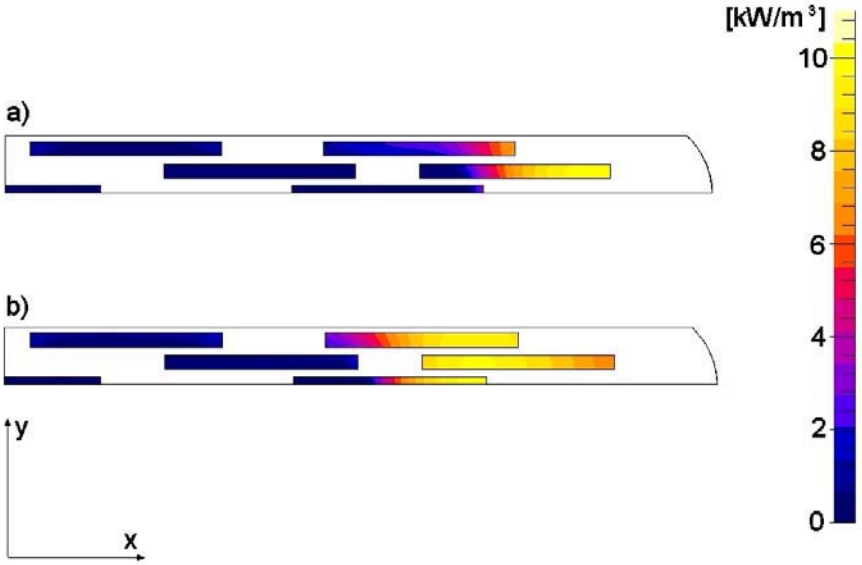

Figure 4.6: Instantaneous power loss density for $I = 0.6I_c$ at $\omega t = \pi/2$ for the models with constant J_c (a) and $J_c(x)$ dependence (b). In (a) the peak of the dissipated power (brightest zone) is near the edge of the tape, in (b) it is shifted towards the centre. The picture refers to 1/4 of the whole geometry.

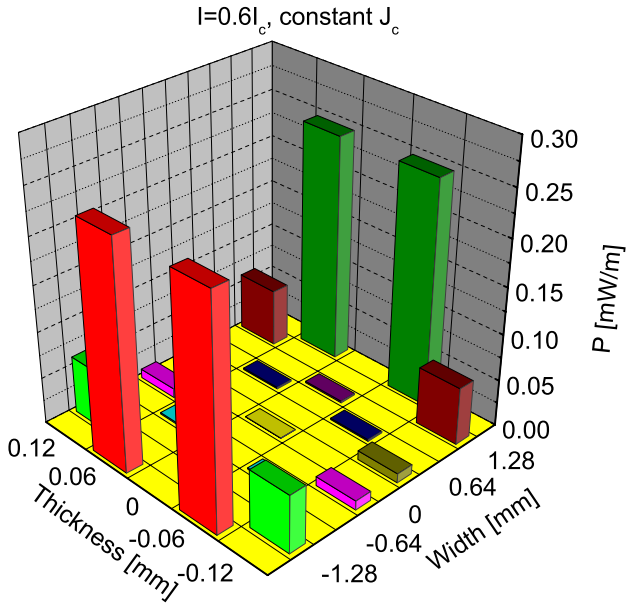

Figure 4.7: AC losses in the individual filaments at $0.6I_c$, computed with the constant J_c model. Most of the power dissipation occurs in the outermost filaments.

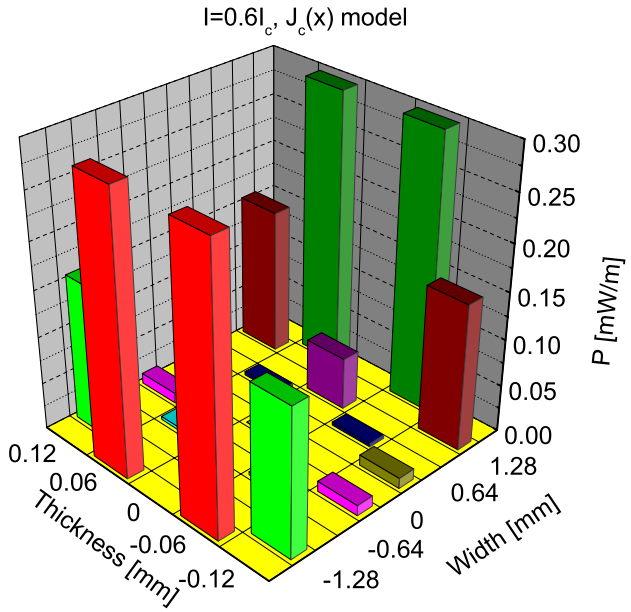

Figure 4.8: AC losses in the individual filaments at $0.6I_c$, computed with the $J_c(x)$ model. The losses are higher than the ones computed with the constant J_c model.

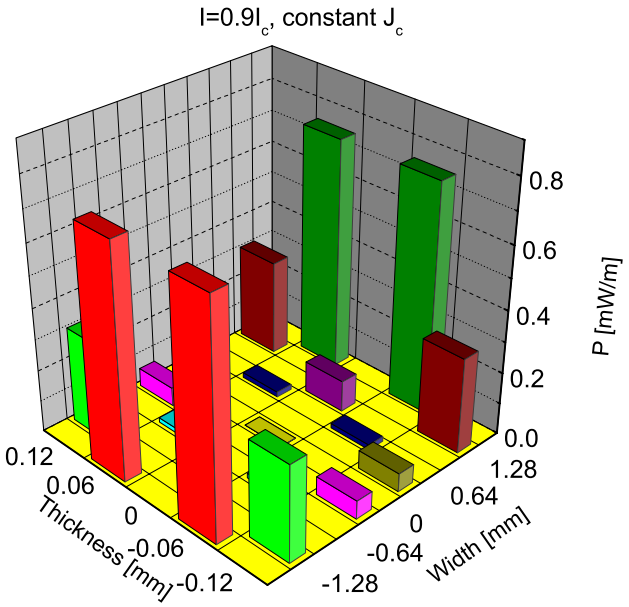

Figure 4.9: AC losses in the individual filaments at $0.9I_c$, computed with the constant J_c model.

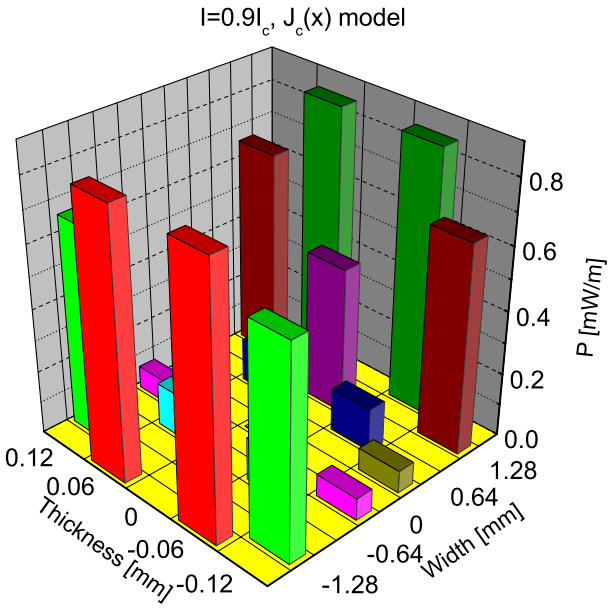

Figure 4.10: AC losses in the individual filaments at $0.9I_c$, computed with the $J_c(x)$ model. The filaments situated half-way between the edge and the centre of the tape dissipate considerably, since most of the transport current flows there, see Fig. 4.11.

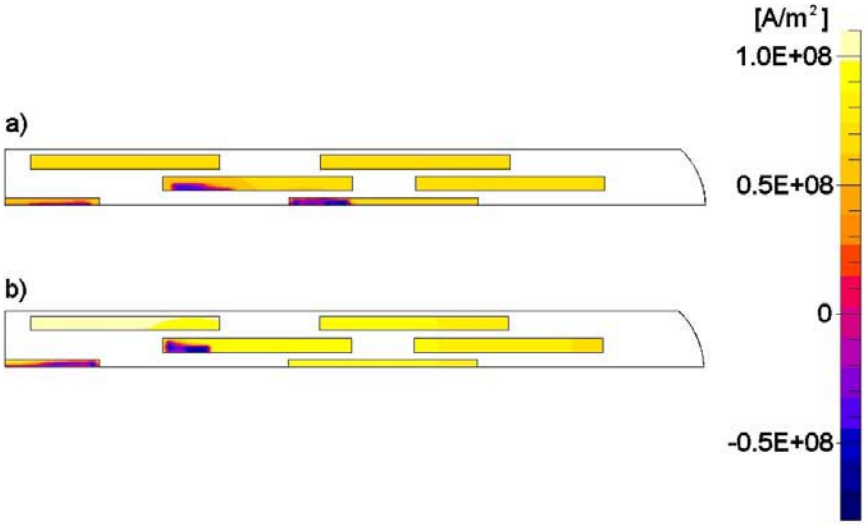

Figure 4.11: Current density distribution at $0.9I_c$, computed with the constant J_c (a) and $J_c(x)$ (b) models. In (b) most of the current is no longer carried by the outer filaments, but by the filaments situated in a more central position.

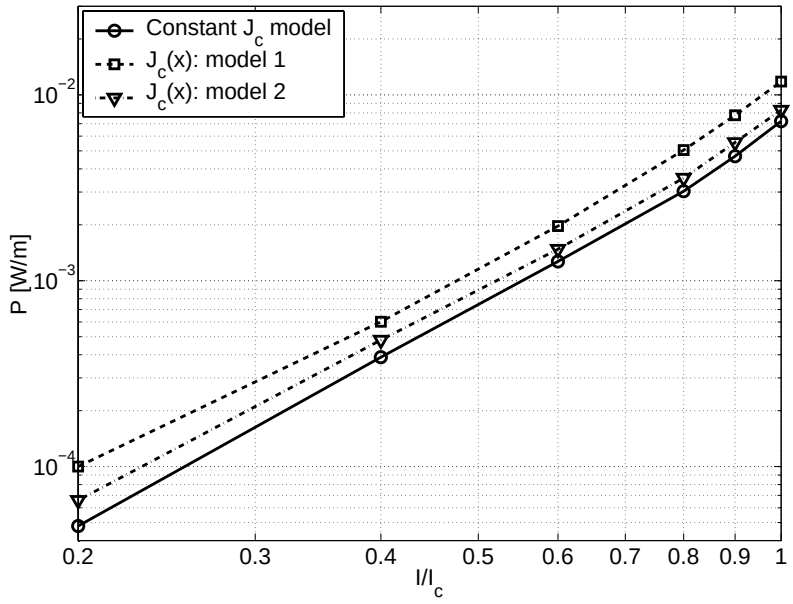

Figure 4.12: AC losses as a function of the normalized transport current, computed with the constant J_c model and with two $J_c(x)$ models, given by Eq. (4.3) and (4.5), respectively.

of $0.6I_c$, for the constant J_c and $J_c(x)$ model, respectively. In general, the current tends to flow in the outer part of the tape: with the $J_c(x)$ model, the current finds there a lower critical current density, so that the outer filaments immediately saturate and give rise to large power dissipation. With the $J_c(x)$ model the maximum of the power loss density is no longer near the

edge, but shifted towards the centre because it is where most of the current flows. The losses for the $J_c(x)$ model are higher than the corresponding losses for the constant J_c model, due to the lower J_c found near the edge with the $J_c(x)$ model and to the rapid increase of the electric field in the $E-J$ curve, once the J_c limit has been exceeded. In both cases the outer filaments dissipate more than 90% of the total losses, see Figs. 4.7-4.8.

When the amplitude of the applied current is increased, the internal filaments start to saturate as well. The losses in individual filaments at $0.9I_c$ are shown for the two models in Figs. 4.9-4.10. Again, the losses are higher with the $J_c(x)$ model than with the constant J_c model. With the $J_c(x)$ dependence the filaments situated half-way between the edge and the centre dissipate considerably, since they carry most of the transport current, see Fig. 4.11.

Figure 4.12 reports the AC losses as a function of the transport current, normalized to I_c, computed by different models. Displayed are also the results of simulations performed with a smoother $J_c(x)$ dependence (model 2 in the figure), the same dependence of the power index n given by Eq. 4.4:

$$J_c(x)/J_{c0} = 0.4 + 0.6e^{-x^2/1.8^2}, \tag{4.5}$$

with $J_{c0} = 8.81 \cdot 10^7\ A/m^2$.

With the constant J_c model, the current is more evenly distributed among the filaments. The outer filaments, which are the main source of AC power dissipation, are less saturated and have lower AC losses than when J_c decreases towards the edges of the tape. The losses computed by model 2 (Eq. 4.5) fall between the ones computed by model 1 (Eq. 4.3) and the constant J_c model, since the effects of the decrease of J_c near the edges of the tape are less pronounced. The AC losses with the constant J_c model are lower by about 50% compared to the losses obtained with model 1 and by about 25% than the ones computed by the smoother model 2.

In summary, the lateral non-uniformity of the critical current density plays an important role in the current distribution inside the tape. The losses result to be sensibly enhanced (about 50%) with respect to the constant J_c distribution. Since the outer filaments are the place where the current tends to flow and where most of the energy dissipation occurs, the optimal situation for minimizing the AC losses would be to have a lateral distribution of J_c as uniform as possible, or, even better, just opposite to the considered one, i.e. with a U-like profile, see also [36].

4.3 Magnetic field dependence of J_c and n

It is well known that the critical current of Bi-2223 tapes is reduced by the presence of a magnetic field. Due to the anisotropy of the material, the reduction is much stronger when the field is perpendicular to the flat face of the tapes than when it is parallel to it, see for example [16]. In fact, the density and the depth of the pinning centres depends on the orientation of the flux lines. It has been shown by Bulaevskii *et al.* [37] that the field dependence of the critical current, including the initial drop at low fields, can be well described when the imperfect texture of the grains is taken into account.

4.3.1 Implementation of a B-dependent $E-J$ model in FLUX3D

From the modelling point of view, it is very important to take into consideration this dependence, since HTS devices are often operating in the presence of magnetic field. A first example are the superconducting magnets: basically they are solenoids producing a strong magnetic field along their axis. Nevertheless, the flux lines at the ends of the solenoid are no longer straight, but inclined with respect to the tapes, thus having a not negligible perpendicular component acting on the tapes and reducing their I_c. Another example are HTS cables, which are usually composed by different superposed layers of superconducting tapes. Due to the large involved transport currents, the outer layers are subjected to the magnetic field produced by the inner

ones, which, even if directed almost parallel to the tapes, can sensibly reduce the effective critical current of the cable and enhance the AC losses.

One of the first models used to describe the field dependence of J_c was proposed by Kim [38]:

$$J_c(B,T) = \frac{J_{c0}(T)}{1+|B|/B_0}, \tag{4.6}$$

where $|B|$ is the magnitude of the flux density, B_0 is a constant and $J_{c0}(T)$ is the critical current density at zero field, which in general depends on the temperature. This model, based on measurements of low temperature superconductors, was interpreted by Anderson in terms of the thermally activated flux creep [39], so that it is known as Kim-Anderson model.

The Kim-Anderson model has been used for modelling the $J_c(B)$ and $n(B)$ dependence of HTS in parallel or perpendicular fields [40, 41]. However, it does not always fit well the experimental data. Better results can be obtained using polynomial fits, see [42], but these fitting laws do not take into account the orientation of the field with respect to the tape. A model for describing the angular dependence of I_c, based on a Gaussian distribution of the misalignment angles of the grains, has been proposed in [43] and the following model describing the $I_c(\alpha, B)$ dependence has been derived [44]:

$$\frac{I_c(B)}{I_c(0)} = \frac{1+(B/B_1)^{p_1}+(B/B_3)^{p_3}F(\alpha,z_1)}{1+(B/B_2)^{p_2}+[(B/B_4)^{p_4}+(B/B_5)^{p_5}]F(\alpha,z_1)}, \tag{4.7}$$

where F is a smoothing function linking the data in parallel and perpendicular field. This model gives a very good fit of experimental data, but it is very complicated and needs the identification of 10 parameters (B_1, ... , B_5, p_1, ... , p_5) and of the additional function F.

Recently, our group has proposed a new and much simpler model for the anisotropic $J_c(\mathbf{B})$ and $n(\mathbf{B})$ dependence [45, 46]. The models of $J_c(\mathbf{B})$ and $n(\mathbf{B})$ are based on measurements in applied magnetic field of varying orientation and magnitude up to 350 mT.

These models, which are suitable for HTS tapes with elliptical or rectangular cross-section with aspect ratio of $10-15$, are based on the assumption that the critical current density and the power index are reduced from their value in the absence of any magnetic field (self or external) acting on the superconductor:

$$J_c(\mathbf{B}) = J_{c0}F_J(\mathbf{B}) \tag{4.8}$$

$$n(\mathbf{B}) = n_0F_n(\mathbf{B}), \tag{4.9}$$

where J_{c0} and n_0 are material characteristics, which have always been taken for given in this thesis. The functions $F_J(\mathbf{B})$ and $F_n(\mathbf{B})$ have been derived from experimental measurements of the $I_c(\mathbf{B})$ and $n(\mathbf{B})$ dependence, so that $J_c(\mathbf{B})$ and $n(\mathbf{B})$ are modelled as follows:

$$J_c(\mathbf{B}) = J_{c0}\frac{I_c(\mathbf{B})}{I_c(0)} = \frac{J_{c0}}{48-6.8e^{-B_\parallel/B_0}-40.2e^{-B_\perp/B_0}} \tag{4.10}$$

$$n(\mathbf{B}) = n_0\frac{n(\mathbf{B})}{n(0)} = \frac{n_0}{30.8-7.5e^{-B_\parallel/B_0}-22.3e^{-B_\perp/B_0}}, \tag{4.11}$$

where $B_\parallel$ and $B_\perp$ are the absolute values of the magnetic field components (in Tesla), respectively parallel and perpendicular to the wide side of the tape, and $B_0 = 1\ T$ is a normalizing constant, formally needed to obtain dimensionless exponent. It has to be pointed out that the experimental measurements have been performed in applied field, whereas Eqs. 4.10-4.11 refer to the magnetic field experienced by the material, including the self-field. The parameters J_{c0} and n_0 cannot be directly measured, because when no magnetic field is externally applied, there is always the self-field acting on the superconductor. The following assumption has been made: the intrinsic $J_c(\mathbf{B})$ dependence is of the same kind of the measured $I_c(\mathbf{B})$ dependence

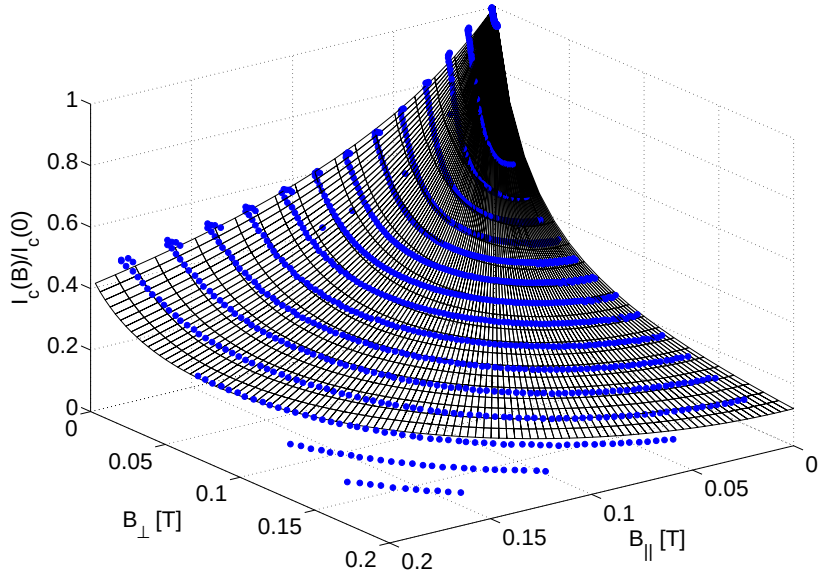

Figure 4.13: Field dependence of the critical current: experimental points (dots) and fitting function $F_J(\mathbf{B})$ used in Eqs. 4.8 and 4.10 (meshed surface).

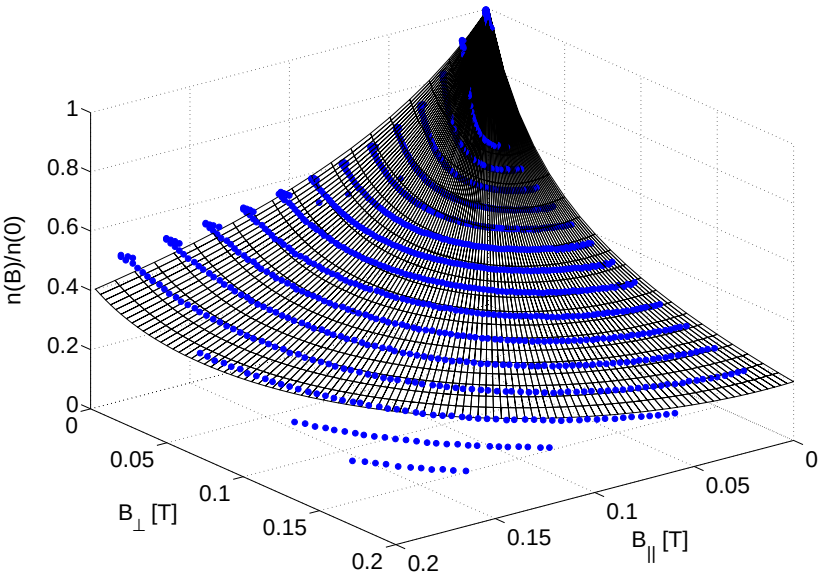

Figure 4.14: Field dependence of the power exponent n: experimental points (dots) and fitting function $F_n(\mathbf{B})$ used in Eqs. 4.9 and 4.11 (meshed surface).

and the parameter J_{c0} takes the place of $I_c(0)$, which is the critical current measured without applying any external magnetic field. This assumption is reasonable, since the characterization has been made on samples with critical current of about 19 A, which produces a maximum local self-field of about 7 mT near the edge and even lower inside the tape, as can be obtained by

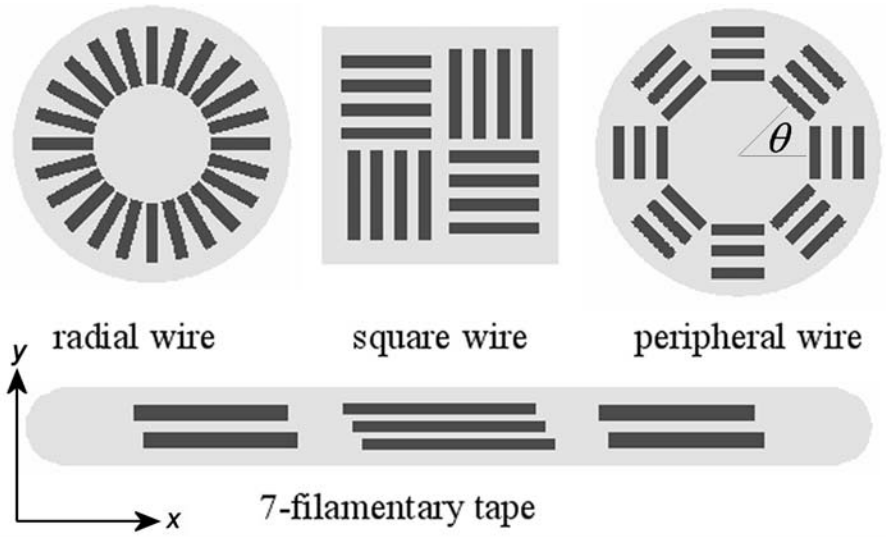

Figure 4.15: Transverse cross-section of the different wires.

FEM simulations. This means that in the fit of experimental data the error due to the presence of the self-field can be neglected.

Figures 4.13 and 4.14 show the decrease of the critical current and of the power exponent n (normalized to their value in zero applied field) as a function of the parallel and perpendicular components of the applied magnetic field. The dots are the experimental points, the meshed surfaces represent the functions $F_J(\mathbf{B})$ and $F_n(\mathbf{B})$ used in Eqs. 4.8-4.11.

4.3.2 Local effects of the magnetic self-field in HTS wires

The B-dependent models (4.10) and (4.11) will be extensively used in chapter 5, in order to take into consideration the effects of the self-field on the transport properties of the tapes in multi-layer HTS cables. Given here is an example of the effects of the magnetic self-field combined with the different arrangement of the filaments inside HTS wires.

Compared are four different wires with the same superconducting section but with a different filament arrangement, as displayed in Fig. 4.15. Their outer dimensions and fill factor are given in Table 4.1. The $J_c(\mathbf{B})$ model has been modified in order to compute the effective parallel and perpendicular components of the field, according to the different arrangement of the filaments inside the wires. In the case of the flat tape, the two components are simply the x- and y-components of the field computed by FLUX3D, see Fig. 4.15 as reference. In the case of the square geometry, two superconducting regions have to be defined for FEM computations: the first, corresponding to the horizontal filaments, has the two local components defined as in the case of the tape. The second, corresponding to the vertical filaments, has the parallel and

Conductor	Outer dimensions (mm)	Fill factor
Radial wire (24)	1.4 ∅	0.28
Peripheral wire (24)	1.6 ∅	0.21
Square wire (16)	1.2×1.2	0.30
Flat tape (7)	4.0×0.4	0.26

Table 4.1: Geometry of the conductors shown in Fig. 4.15.

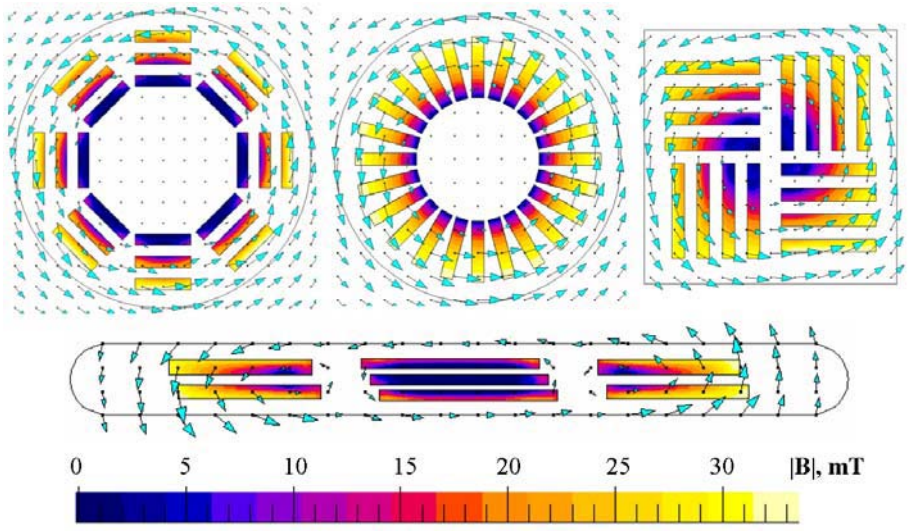

Figure 4.16: Field distribution inside different wires with the same $J_{c0} = 3 \cdot 10^8\ A/m^2$ and transport current $I = 90\ A$ (peak value). The grey scale represents the modulus of the magnetic self-field, the arrows its direction.

perpendicular components given by the computed B_y and B_x, respectively (i.e. inverted with respect to the case of the tape). Finally, in the case of the radial and peripheral wire, the two components are computed by taking into account the orientation of the filaments, which is given by the azimuthal angle θ (see Fig. 4.15). The computation of the effective local components of the magnetic field is made in an external subroutine where the $J_c(\mathbf{B})$ dependence is implemented, similarly to the $J_c(x)$ dependence.

For all the wires the following values have been used: $J_{c0} = 3 \cdot 10^8\ A/m^2$, $n_0 = 25$. The produced self-field has different local components for the different filament arrangements, as displayed in Fig. 4.16, which refers to an applied transport current of 90 A. The grey scale represents the magnitude of the magnetic field in the superconductor, the arrows represent its direction, their size being proportional to the modulus of the field. It can be seen that the filaments of the radial wire are subjected to a local magnetic field perpendicular to them, whereas the ones of the peripheral wire are subjected to an almost parallel field. The square wire is in an intermediate situation: the magnetic field has both the parallel and perpendicular components. The flat tape has a small perpendicular component only near the edge. The local decrease of the critical current density strongly depends on the direction of the field, so that the decrease of the transport capacity is much more important in the radial than in the peripheral configuration. In order to make a comparison between conductors with different critical current, the transport current AC losses of the three wires and of the tape have been normalized by the quantity $f\mu_0 I_c^2/\pi$, see Eq. 4.2, where I_c is the effective critical current calculated for each conductor by means of the following expression:

$$I_c(\mathbf{B}) = \int_S J_c(\mathbf{B})\ dS. \tag{4.12}$$

The normalized losses are plotted in Fig. 4.17 as a function of the reduced transport current and compared to Norris's theoretical predictions. The normalized AC losses do not depend on the choice of J_{c0} and the loss comparison remains valid for other J_{c0} values as well. The square wire and the radial wire exhibit similar self-field losses, falling onto Norris's elliptical prediction. They have transport current loss behaviour comparable to mono-filamentary wires of square and round shape. The AC losses of the peripheral wire, however, are lower by nearly 50% in the

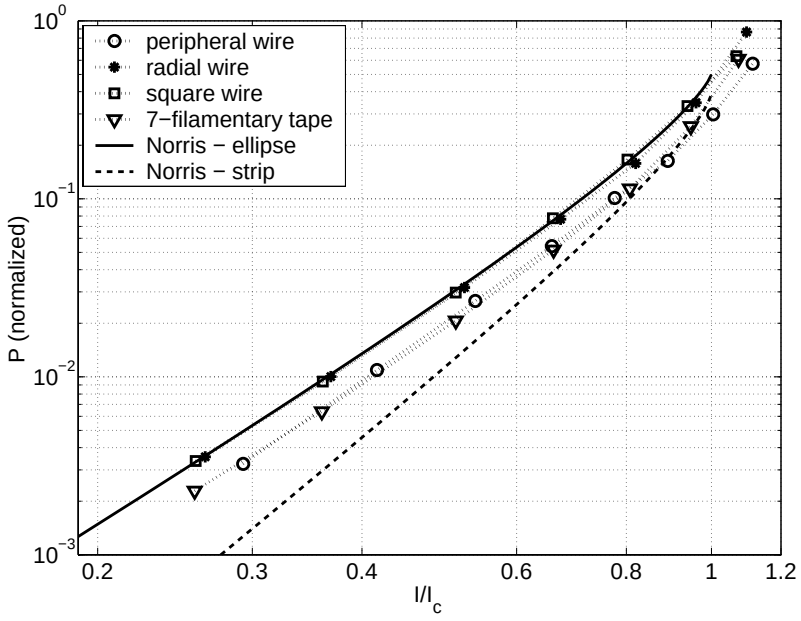

Figure 4.17: Self-field AC losses as a function of the reduced transport current for different wires. The losses at 59 Hz are normalized by the quantity $f\mu_0 I_c^2/\pi$ to make them independent of the effective critical current of each conductor. The theoretical predictions by Norris are displayed as well.

whole current range, and are similar to those of the 7-filamentary tape, whose large aspect ratio (width/thickness) makes it a-priori more favorable in transport current applications. It should be noted that the low self-field losses of the 7-filamentary tape are also due to its sectioned filament configuration, which prevents deep flux penetration into the internal section, whereas multi-filamentary tapes with interleaved filaments behave in general like a mono-filamentary one with elliptical shape and have higher self-field losses.

The low self-field loss of the peripheral wire can be explained by the higher $J_c(\mathbf{B})$ in that conductor compared to the $J_c(\mathbf{B})$ of the other wires. As mentioned before, this is due to the specific configuration of its filaments, which are almost parallel to the self-field, and as a result the decrease of $J_c(\mathbf{B})$ in the peripheral wire is least significant.

4.4 3D problems coupled with circuit equations

A new non-linear circuit coupled $\mathbf{T} - \mathbf{T_0} - \Phi$ formulation has been recently proposed [26] for solving problems with solid conductors. This means that it is in principle possible to solve 3D problems with applied transport current. The $\mathbf{T_0}$ term in the name of this formulation refers to an auxiliary potential used to impose the desired current through the conductor, so that the magnetic flux continuity equation and Faraday's law are written as

$$\nabla \cdot (\mu_0(\mathbf{T} + \mathbf{T_0} - \nabla\Phi)) = 0 \tag{4.13}$$

$$\nabla \times \mathbf{E} + \frac{\partial}{\partial t}(\mu_0(\mathbf{T} + \mathbf{T_0} - \nabla\Phi)) = 0. \tag{4.14}$$

This new formulation is still at an initial stage of development and further improvement of the convergence of the solving algorithm is needed. Nevertheless, the test on a couple of simple problems with superconductors has given positive results.

In the $\mathbf{T}-\Phi$ formulation, used for problems in applied field only (see chapter 6), the simulated geometry is drawn inside an air domain, which completely surrounds it. In this case, the end effects (due to the finiteness of the length) are taken into consideration, see for example the coupling current in Fig. 6.6, where the current loop is closed at the ends of the filaments. This is not the case with the $\mathbf{T}-\mathbf{T_0}-\Phi$ formulation, where the electric terminals between which the current (or the voltage) is imposed must lie on the domain boundary. As a consequence, the end effects are not taken into consideration: for example, the application of an external magnetic field perpendicular to the direction of the transport current in a straight wire will give the same results of the 2D case, where the third dimension is considered infinitely long.

The new formulation has been firstly validated by comparing the results obtained in 2D for a straight geometry; therefore, it has been tested on two problems which cannot be simulated in 2D: a bulk superconductor with meander geometry and a conductor composed by different twisted filaments.

4.4.1 Comparison with 2D results

For the comparison with 2D results a simple geometry has been used, two superconducting square filaments separated by a silver matrix. The conductors are fed with an AC current source. Because of the symmetry of the problem, in the simulations only one fourth of the full geometry has been considered and the appropriate symmetry conditions (i.e. normal magnetic field) on the xz and yz symmetry planes have been applied.

With reference to the complete geometry, the transverse section of each filament is $0.2\ mm \times 0.2\ mm$ and the length along the z-direction is $2\ mm$. The frequency of the current source is $50\ Hz$. Figure 4.18 displays the 3D FEM geometry and the corresponding mesh used for the simulations (a), with a detailed view of the conductor region around the point A (b). On the domain boundary (lines BC and CD) the mesh density is quite coarse (15 points). The lines connecting the domain corners B and D to the conductor region have been assigned a logarithmic mesh, in order to have a sufficiently fine mesh near the conductor. The superconducting and silver regions have been assigned a mesh 15×7 and 7×7, respectively, as shown in Fig. 4.18b. Both regions have been meshed with a mapped mesh, i.e. composed by a regular grid of rectangular elements, which allows to obtain more precise results. The rest of the domain has been meshed automatically, i.e. with triangular elements. For the 2D problem the same mesh density as it appears in the ABCD plane has been used. With the 3D model there is the possibility to mesh the geometry along the z-axis. This is a key issue, which strongly depends on the particular simulated problem. In the considered case, the current source is applied on the boundary of the domain (more precisely on the conductor surface AEFG and on the corresponding surface on the A'B'C'D' plane), so that the current is forced to flow along the z-direction. In addition, the formulation is implemented in such a way that the current can leave the solid conductor only through the terminals where the current is imposed [26]. Since there are no changes in the physical and/or geometrical properties along the z-direction, this means that in this case there is in principle no need of intermediate mesh points along that direction. Nevertheless, as it will be shown later, the fact that assigning mesh points along the length does not influence the numerical results has been verified.

In order to make a quantitative comparison between 2D and 3D simulations, in 3D a transverse section (parallel to the xy plane) has been chosen for the evaluation of the current distribution and of the AC losses. The AC losses are computed as usual with the integral of the product $\mathbf{J} \cdot \mathbf{E}$. In 3D the AC losses in the superconductor are computed both as surface integral on a transverse cross-section and as volume integral (and then divided by the sample length).

The comparison has been made in self field, i.e. without applying any external magnetic field, for different transport currents, from $0.2I_c$ to $1.2I_c$. Figure 4.19 shows the AC losses as a function of the applied current in 2D and 3D. In 3D the losses computed with the surface and

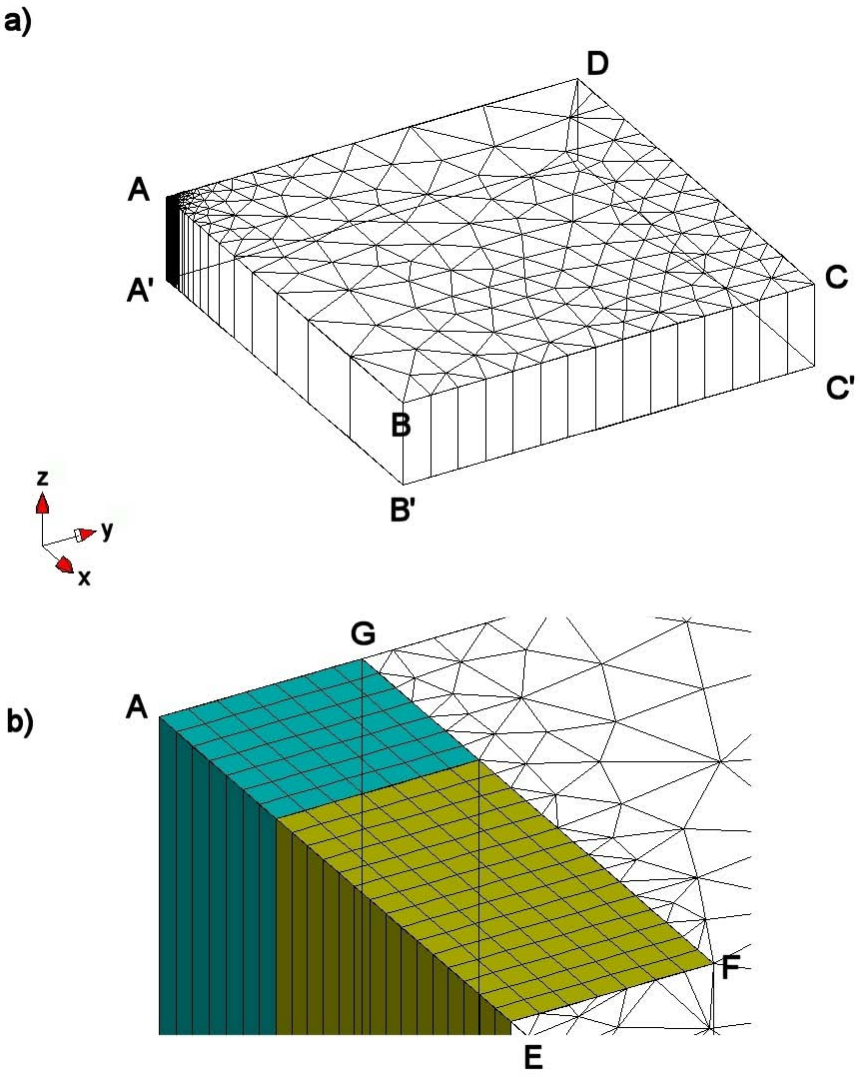

Figure 4.18: 3D geometry and mesh utilized for FEM simulations (a), with a detailed view of the conductor region (b).

volume integral are exactly the same and they are slightly lower than in 2D, on average by 10%.

The slight difference between 2D and 3D can be imputed to the different way of using the electric variables $\mathbf{J}$ and $\mathbf{E}$ in the two formulations. In fact, the $\mathbf{A} - V$ formulation uses the electric field as variable and the conductivity $\sigma(\mathbf{E})$ for describing the electrical properties of the superconductor, see Eq. 3.6. The $\mathbf{T} - \mathbf{T_0} - \Phi$ formulation uses the current density $\mathbf{J}$ as variable (derived from the potential $\mathbf{T}$) and the resistivity $\rho(\mathbf{J})$ is expressed as follows:

$$\rho(\mathbf{J}) = E_c/J_c \ (|\mathbf{J}|/J_c)^{n-1} + \rho_0. \tag{4.15}$$

In addition, in both cases the electric variables $\mathbf{J}$ and $\mathbf{E}$ are not computed directly, but they are derived from the state variables by means of differential relations (computed in a discrete way), which can be the cause of additional numerical differences.

The current density distributions look very similar in 2D and 3D: an example is shown in Fig. 4.20. As mentioned before, the mesh point density along the z-direction has been varied, in order to see if this has an influence on the AC losses. Table 4.2 lists the losses per unit length obtained with the 3D model by assigning 0, 5, 10 and 20 points to the mesh along

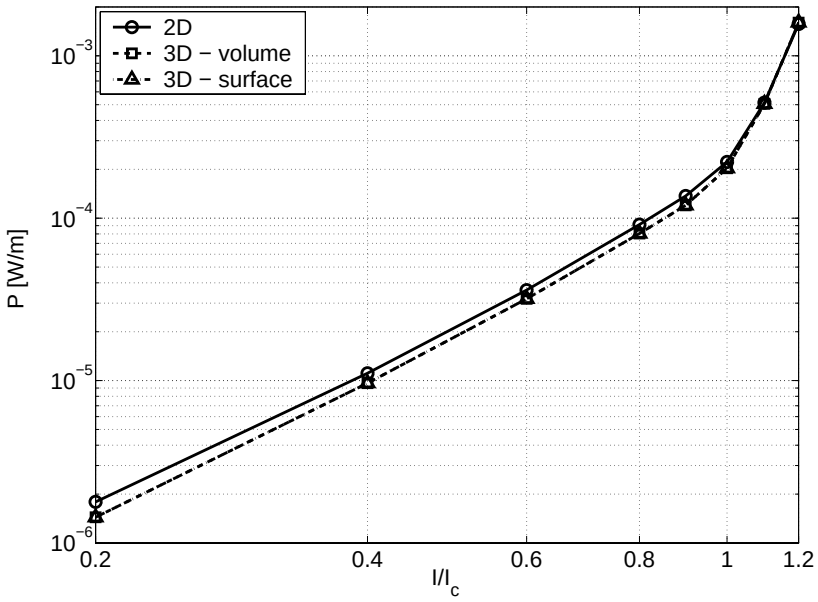

Figure 4.19: Transport current AC loss comparison at 50 Hz for different reduced current ratios

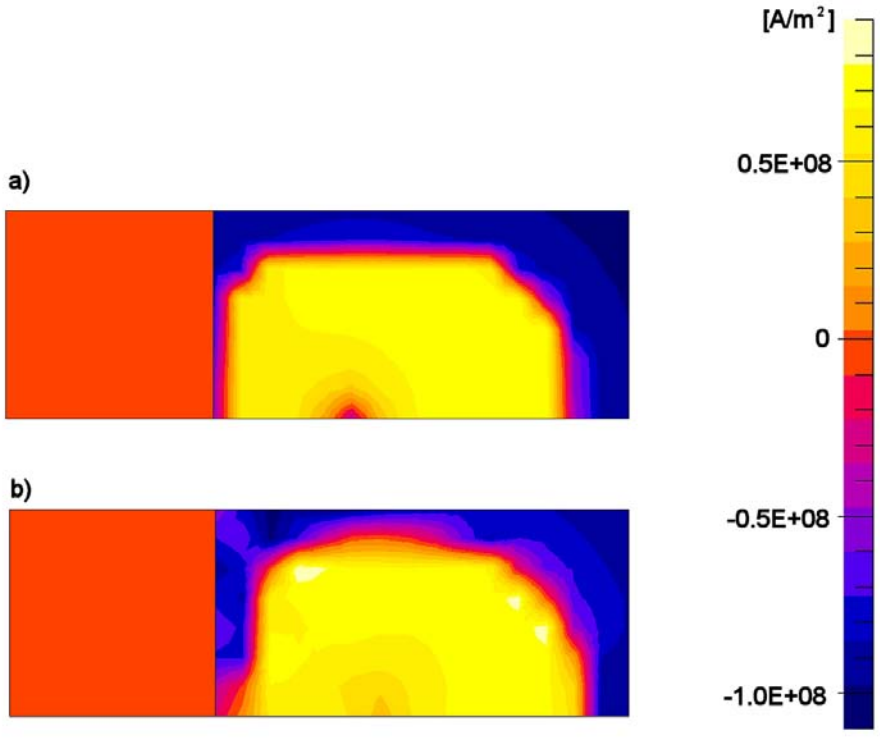

Figure 4.20: Current density distribution (in A/m^2) in 2D (a) and 3D (b), $J_c = 10^8 A/m^2$, $I = 0.8I_c$, $\omega t = \pi$. One fourth of the full geometry is displayed.

the third dimension, respectively, for a transport current of $0.8I_c$. The results are practically the same. The only difference is that, by inserting mesh points along z, the number of nodes and consequently the computation time increase a lot, roughly by a factor proportional to the

Mesh points	AC losses [W/m]
No mesh	$8.05 \cdot 10^{-5}$
5 points	$8.11 \cdot 10^{-5}$
10 points	$8.11 \cdot 10^{-5}$
20 points	$8.12 \cdot 10^{-5}$

Table 4.2: AC losses with different mesh densities for $I = 0.8I_c$.

number of inserted mesh points along the third dimension.

4.4.2 Test results on typical 3D geometries

Once the model has been validated, it has been tested on typical 3D geometries, which the existing 2D models cannot investigate: a conductor with meander geometry and one composed by twisted filaments.

The meander geometry is not just a test geometry, but corresponds to the real case of fault current limiters, which are usually designed as long meander conductors in order to dissipate the power on a surface as large as possible (see for example [47]). The current density distribution for an applied current equal to $0.8I_c$ is displayed in Fig. 4.21. As expected, the current tends to flow following the lowest resistance path, i.e. along the internal side of the conductor. It is interesting to note that, due to the sharp curvature (90°) of the internal corner, the current density has there a very high local value, reaching two times J_c.

Figure 4.22 shows the current density distribution in a conductor composed by eight twisted superconducting tapes with an applied current equal to $0.6I_c$, with a zoom of the upper end. This kind of geometry is created by drawing the initial geometry in 2D (xy plane) and then by extruding it in the third dimension by means of a helical transformation; according to the extrusion, not only the faces and the volumes are created, but also the mesh elements. This is a new tool developed in FLUX3D. It represents a great advantage with respect to building first

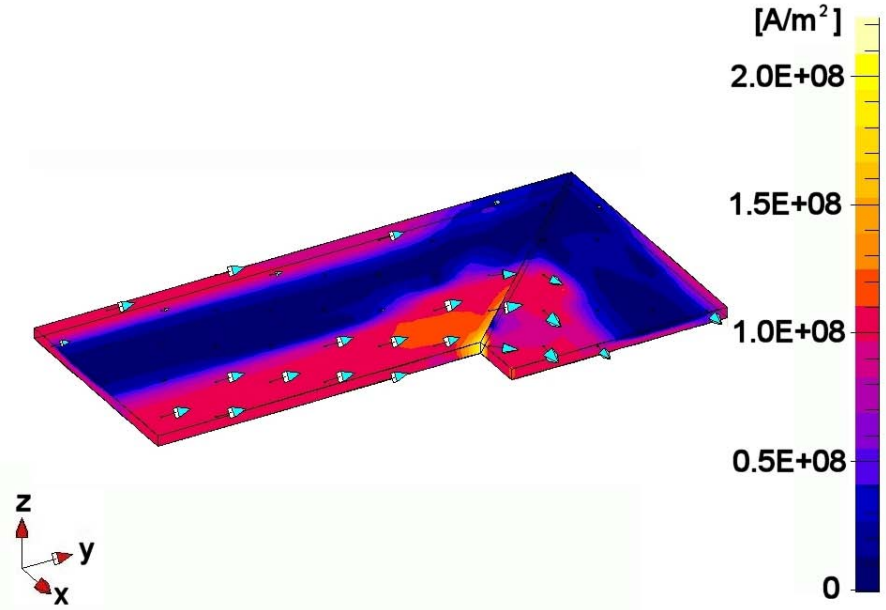

Figure 4.21: Current density distribution in a superconductor with meander geometry, $J_c = 10^8\ A/m^2$. Even if the total current is $0.8I_c$, the current density exceeds locally $2J_c$.

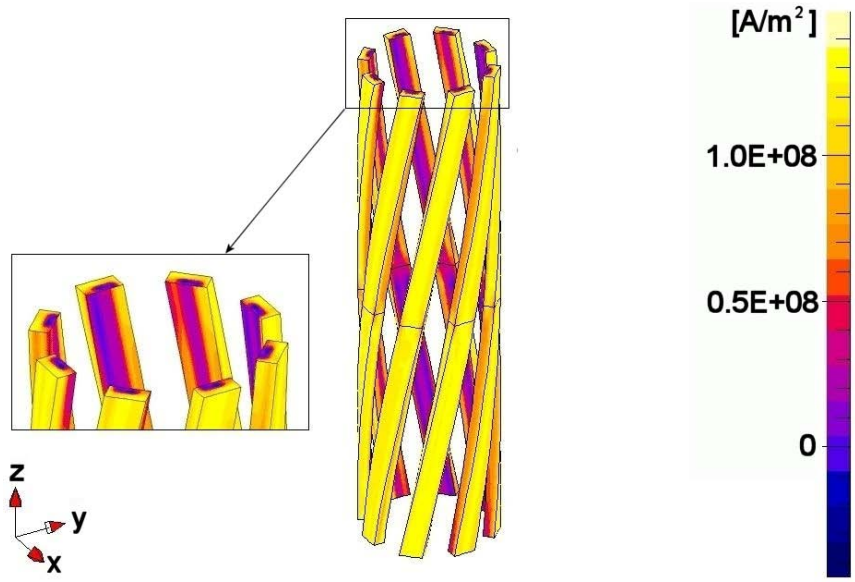

Figure 4.22: Current density distribution in twisted superconductors, $I = 0.6I_c$, $J_c = 10^8 A/m^2$. The twisted volumes are obtained by extruding the rectangular section of the filaments with an helical transformation along the z-axis.

the 3D geometry and then defining the mesh, for in this way the mesh, defined automatically by the extrusion, is composed by tetrahedral elements of high quality.

4.5 Original contributions of this thesis

- Comparison of the results obtained by FLUX3D with the ones obtained with FLUX2D and with another analytical model for simulating multi-filamentary HTS tapes in different working conditions.
- Refinement of the $E - J$ model with the introduction of the lateral $J_c(x)$ and $n(x)$ dependence.
- Implementation of a B-dependent $E - J$ model in FLUX3D.
- Validation and testing of a recently developed 3D formulation for problems coupled with circuit equations.

Chapter 5

From tapes to cables

In this chapter different methods for computing the current repartition and the AC losses of multi-layer HTS cables are presented.

Firstly, the typical structures of HTS cables are described and the problem of their numerical modelling is discussed. Secondly, a simple electrical method, which considers the cable from the macroscopic point of view, is used to find the optimal pitch length of the different layers for obtaining an even current repartition among the layers. Thirdly, 2D FEM computations are used to precisely evaluate the AC losses. It is shown that the effects of the magnetic self-field are not negligible: they cause a reduction of the effective critical current and an enhancement of the AC losses with respect to the situation where the reduction of J_c due to the magnetic field is not taken into consideration. Discussed are also the effects of the field on the individual layers. The electrical model and the 2D FEM computations constitute a complete model for finding the optimal pitch lengths and for evaluating the AC losses. The two models have been applied to a three-layer HTS cable, but they can be used with an arbitrary number of layers: it is a just a matter of computation time.

Afterwards, FEM computations have been used to study the influence of the non-uniformity of the parameters of the individual tapes (contact resistance, I_c, n) on the global performance of a single-layer HTS cable. Analyzed is the case of a single-layer HTS cable composed by straight tapes. This configuration has been chosen in order to compare the results of the loss computation with the values measured on a real sample, which has been assembled by Pirelli and the Slovak Academy of Science.

After this, a model of the cable based on an equivalent circuit model is presented: for a given configuration of the cable, this method allows to find the current repartition among the layers and to evaluate the resistive and hysteretic contributions to AC losses. Analyzed is a four-layer HTS cable, but, again, the developed method can be applied to a cable with an arbitrary number of layers.

Finally, the manufacturing process and the loss characterization of a HTS power-link assembled within the European project BIG-POWA are presented.

5.1 Why superconducting cables?

The superconducting properties of HTS materials can be exploited for manufacturing HTS cables, which can offer several advantages with respect to conventional cables:

- reduced loss during power transmission;
- reduced dimension and weight due to the large carried current densities;
- environmental compatibility: no temperature increase in the surrounding soil.

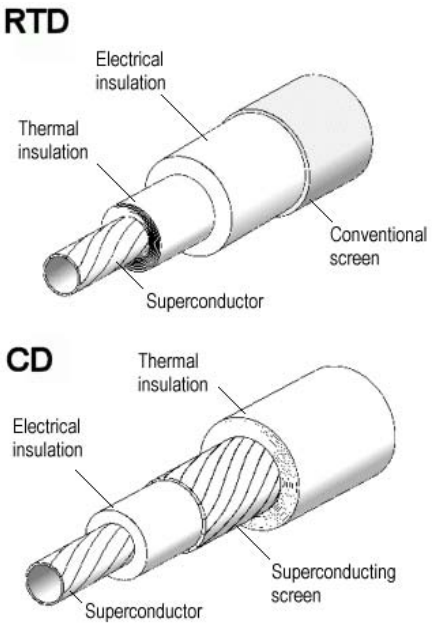

Figure 5.1: Basic designs of HTS cables: Room Temperature Dielectric (RTD) and Cryogenic Dielectric (CD).

Two basic designs for superconducting AC cables exist: room temperature dielectric (RTD) design and cryogen dielectric (CD) design. They are schematically represented in Fig. 5.1. The manufacturing of RTD cables is simpler and has the advantage of having a room temperature dielectric (outside the cryostat), which also makes the cable less expensive. Therefore, for future RTD cables, the only technology to be developed is related to the superconductor itself. On the contrary, CD cables have the dielectric operating at cryogenic temperatures (which may constitute a problem), but, thanks to an arrangement with three phases within the same cryostat (see [48]), can carry a larger amount of current than RTD. In this thesis work the main goal was not the precise design of HTS cables but the development of general methods for the computation of the current repartition among the different layers and the evaluation of the AC losses.

5.2 Difficulties of a direct FEM approach

HTS cables have a quite complex structure. Basically, they consist of different superposed layers of superconducting tapes, wound around a central cylindrical support, called *former*. The tapes are wound both for mechanical reasons and for equalizing the impedance of each layer, in order to have a repartition of the transport current among the layers as uniform as possible. As a matter of fact, a cable with straight layers would behave similarly to a mono-core superconducting wire: the current would flow in the outer layer as long as possible, rapidly saturating it, and then would pass in the second internal layer, then in the third and so on. This is not a good behaviour from the point of view of the losses. In fact, even at transport currents well below the critical current of the cable, the outer layers would be immediately saturated. This would cause a large power dissipation, due to the rapid increase of the voltage once the critical current of the outer layers has been exceeded.

In order to have a more even repartition of the current among the layers, their impedance should be as similar as possible. This can be obtained acting either on the value of the contact

resistance between the cable and the current source [49] or on the self and mutual inductance of the layers, which depend on the pitch length and relative direction they are wound with (see for example [50], [51]). The first solution, even if very simple in principle, is not very practical, because, especially for long cables, the necessary value of the contact resistance would be very high, which would cause a large additional ohmic dissipation in the resistances themselves. In practice the second solution is adopted.

The simulation of a HTS cable with the FEM technique presents several obstacles. First of all, it involves a 3D geometry. The 3D models coupled with circuit equations for injecting a transport current are at an initial stage of development and the solving process is not completely stable. Secondly, the size of the problem is rapidly increasing. In the previous chapter some 2D problems with superconducting tapes have been shown, whose solution typically takes few hours. A HTS cable is composed by many tapes (few tens), so that the necessary memory, space and computing time resources become enormous. Finally - and this is the most substantial difficulty - HTS cables involve geometries (the different layers) twisted in opposite direction and/or with different pitch lengths. At this moment, this causes connection problems between the elements of differently twisted regions and the continuity of the physical quantities (e.g. the magnetic field) across the different regions is not guaranteed. Therefore a simpler approach is necessary.

The idea is to use a simple electrical model, which describes the cable from the macroscopic point of view, for finding the current repartition for a given geometrical configuration of the cable. Due to the simplicity of the model, the simulation can be run for different geometrical configurations in order to find the ones leading to a repartition of the current among the layers as uniform as possible, for minimizing the AC losses. This model takes into account the 3D structure of the cable, but not the internal structure of the tapes. For this reason, it cannot be used for computing the AC losses, which, as it has been shown in the previous chapter, strongly depend on local effects. For this purpose, 2D FEM simulations can be utilized, with the use of independent current sources (as many as the layers) for imposing the desired current in each layer.

5.3 Electrical model

The analysis has been carried out for a three-layer cable, but this method can be applied to a cable with an arbitrary number of layers. The radius of the former has been chosen equal to 14 mm, which is a good compromise between the reduction of the conductor volume and the possibility of having a sufficiently high total critical current. Such a diameter allows to have sufficiently short pitch lengths (without damaging the transport properties of the tapes), which is important for obtaining an even current repartition among the layers. In particular, the radius of the layers (in the centre of the superconducting tapes) is 14.88 mm, 15.6 mm and 16.32 mm, respectively, and it has been considered as a fixed parameter. The different layers are referred to with numbers from 1 to 3, from the inner to the outer one. The geometry of the cable is sketched in Fig. 5.2. Each layer is composed by 20 superconducting tapes, so that the total number of tapes is 60, providing a total effective critical current for the cable of about 4.2 kA. The main physical and geometrical parameters of the cable are summarized in Table 5.1.

From the macroscopic point of view, a multi-layer HTS cable can be modelled as an electric parallel of different branches, one for each layer of superconducting tapes. Each branch consists of a non linear resistance, taking into account the typical voltage-current relation for HTS superconductors, and a self and mutual inductance, depending on the geometrical configuration. In this model the contact resistance between the cable and the current source can be easily inserted, but for long lengths its influence on the current repartition can be neglected [52]. In addition, the influence of the inductive part on the current repartition is the main subject of investigation. The self and mutual inductances can be computed by means of a spatial

Cable length l $[m]$	1
No. of layers n_l	3
Radius layer 1, r_1 $[m]$	$14.88 \cdot 10^{-3}$
Radius layer 2, r_2 $[m]$	$15.60 \cdot 10^{-3}$
Radius layer 3, r_3 $[m]$	$16.32 \cdot 10^{-3}$
Radius of return path, D $[m]$	$32.64 \cdot 10^{-3}$
Minimal pitch length, layer 1–3, ${l_p}^{min}$ $[m]$	$22 \cdot 10^{-2}$
Maximal pitch length, layer 1–3, ${l_p}^{max}$ $[m]$	$76 \cdot 10^{-2}$
Critical current, layer 1–3, I_{ci} $[A]$	1400
Power index, layer 1–3, n	21
Frequency of the current source, f, $[Hz]$	50

Table 5.1: Parameters of the three-layer cable simulated with electrical and FEM model.

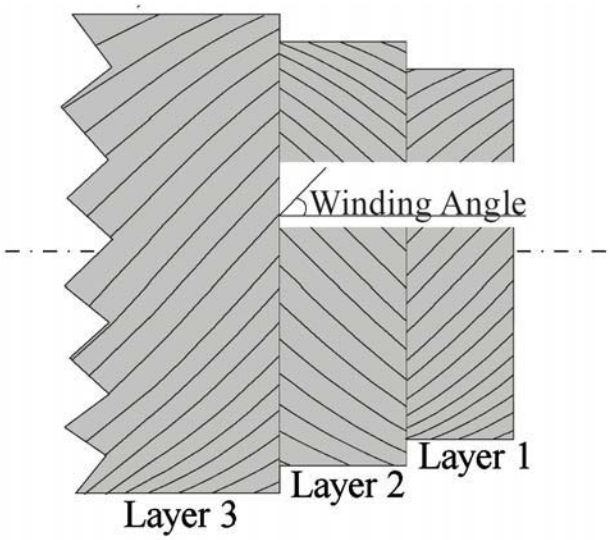

Figure 5.2: Longitudinal view of a 3-layer HTS cable. The winding angle α_i between the tapes of one layer and the axis of the cable is indicated.

integration of the magnetic energy in the different regions of the cable [53, 54]. In particular they can be expressed as follows (per unit length):

$$L_i = \mu_0 \frac{\pi r_i^2}{l_{pi}^2} + \mu_0 \frac{ln(D/r_i)}{2\pi} \tag{5.1}$$

$$M_{ij} = M_{ji} = \mu_0 \frac{a_i a_j}{l_{pi} l_{pj}} \pi r_i^2 + \mu_0 \frac{ln(D/r_j)}{2\pi} \qquad r_j > r_i. \tag{5.2}$$

In Eqs. 5.1-5.2 the indices i and j identify the layer, a_i and a_j are constants (+1 or -1) taking into account the relative winding direction (clockwise or anti-clockwise); D is the radius of the shield confining the magnetic field and l_{pi} is the winding pitch of the i-th layer. The pitch length and the winding angle are linked by $l_{pi} = 2\pi r_i / \tan(\alpha_i)$, where α_i is the angle between the winding direction of the tapes in the i-th layer and the longitudinal axis of the cable, see Fig. 5.2. Figure 5.3 gives a graphical representation of this model. It has to be mentioned that the impedance of the layers is mostly determined by the inductive part. In fact, the resistive

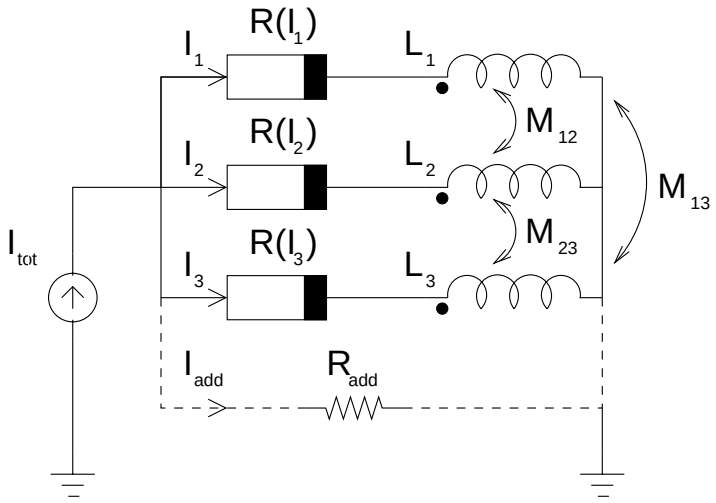

Figure 5.3: Electric model of the cable. Each layer consists of a non-linear resistance, depending on the current flowing through it, and a self and mutual inductance, depending on the geometry of the cable. The additional resistance R_{add}, used for the current source model, is shown as well.

term is given by the non-linear resistance derived from the power-law (2.18)

$$R(I) = \frac{V_c}{I_c}\left|\frac{I}{I_c}\right|^{n-1}, \tag{5.3}$$

with the following typical orders of magnitude: $V_c = 10^{-4}\ V$ (for the simulation of 1 m of cable) and $I_c = 10^3\ A$; at $I = I_c$ the last term of Eq. 5.3 is equal to 1. Therefore the resistive term is in the order of $10^{-7}\ \Omega$.

On the other hand, the inductances computed by Eqs. 5.1- 5.2 are in the order of $10^{-7}\ H$ (per unit length), so that the corresponding impedance is in the order of $\omega L = 2\pi f L = 100\pi L = \pi \cdot 10^{-5}\ \ \Omega$, with a current source at 50 Hz. In any case, the resistive term has been kept in the implementation of the electric model, even because when the current exceeds I_c, the term $(I/I_c)^{n-1}$ in Eq. 5.3 increases very rapidly.

Kirchhoff's voltage equations are written by taking into account that the voltage drop along the branch corresponding to each layer is the same:

$$\begin{pmatrix} V_1 \\ V_2 \\ V_3 \end{pmatrix} = \begin{pmatrix} L_1 & M_{12} & M_{13} \\ M_{21} & L_2 & M_{23} \\ M_{31} & M_{32} & L_3 \end{pmatrix} \begin{pmatrix} \dot{I}_1 \\ \dot{I}_2 \\ \dot{I}_3 \end{pmatrix} + \begin{pmatrix} R(I_1) \\ R(I_2) \\ R(I_3) \end{pmatrix} \begin{pmatrix} I_1 \\ I_2 \\ I_3 \end{pmatrix} \tag{5.4}$$

This model has been implemented in the software package MATLAB[1] for solving the system of differential equations for the circuit shown in Fig. 5.3.

Two models have been implemented, one with a voltage source feeding the circuit, the other with a current source. In the latter case the set of differential equations is written in a slightly different way. In fact, the currents flowing in each branch are not independent, but are linked to the value imposed by the current source. Consequently, an additional equation has to be added in order to have the equal number of equations and unknowns. A fourth branch with a very large resistance $R_{add} = 1\ M\Omega$ has been added, so that the current flowing there is negligible and does not influence the numerical results (see Fig. 5.3). The system of differential equations

[1] http://www.mathworks.com

Layer radius (mm)	Drum radius (mm)	Angle range (°) $\epsilon_c = 0.15\%$	Angle range (°) $\epsilon_c = 0.3\%$
10	500	4-17	2-27
15	600	7-22	3-36
20	750	9-25	5-45

Table 5.2: Allowed winding angles.

is written as follows:

$$\begin{pmatrix} L_1 & M_{12} & M_{13} \\ M_{21} & L_2 & M_{23} \\ M_{31} & M_{32} & L_3 \end{pmatrix} \begin{pmatrix} \dot{I}_1 \\ \dot{I}_2 \\ \dot{I}_3 \end{pmatrix} = - \begin{pmatrix} R(I_1) & 0 & 0 \\ 0 & R(I_2) & 0 \\ 0 & 0 & R(I_3) \end{pmatrix} \begin{pmatrix} I_1 \\ I_2 \\ I_3 \end{pmatrix} + \begin{pmatrix} R_{add} I_{add} \\ R_{add} I_{add} \\ R_{add} I_{add} \end{pmatrix} \tag{5.5}$$

where I_i and $\dot{I}_i$ are the current flowing in the i-th branch and its time derivative, respectively, R_{add} and I_{add} are the resistance of the additional branch and the corresponding current, so that $R_{add} I_{add}$ represents the voltage drop along the branches.

For the correct definition of the system, the imposed current must be equal to the sum of the currents flowing in the different branches:

$$I_{tot} = \sum_{i=1}^{3} I_i + I_{add} \qquad i = 1, 2, 3. \tag{5.6}$$

The two models have been tested on the same cable configurations and they have given identical results. For the optimization process the current source model has been used, because it is more practical. In fact, the desired current flowing in the cable can be directly imposed, instead of looking for the appropriate corresponding voltage.

The optimization process consists in solving the differential equations (5.5) for many different configurations of the cable, determined by the pitch length and by the relative winding orientation of the layers. The range of the allowed pitch lengths is determined by the quality of the tapes and by their resistance to mechanical deformation. The pitch length cannot be too short, because of the strain caused by winding the tapes around the former. On the other hand it cannot be too large, because of the bending strain of the entire cable: during the manufacturing process the cable conductor has in fact to be wound on a drum with a radius of one metre or two. This is another reason (in addition to the problem of the current repartition) why long cables need helicoidal winding. American Superconductor[2] has produced tapes reinforced with a thin layer of stainless steel which can sustain a strain of 0.3% instead of usual values around 0.15% [55]. The range of possible winding angles results to be sensibly widened, as shown in Fig. 5.4. Table 5.2 reports typical ranges of the winding angles as a function of the radius of the layer, for tapes able to sustain a strain of 0.15% and 0.3%, respectively. The table also reports the radius of the drum. Data have been provided by Pirelli. In addition, there are also economic reasons to be taken into consideration for choosing the pitch length: a cable wound with short pitch lengths need longer tapes. In any case, the purpose of this analysis is not to find the really best design parameters, but to provide and test a general method for computing the optimal pitch lengths. A test range of 55 possible pitch lengths, from 22 *cm* to 76 *cm*, has been therefore chosen according to the possible winding range $[7° - 22°]$ for a former radius of 15 *mm* and standard quality tapes, see Table 5.2.

The relative orientation of the layers enters the values of the mutual inductance by means of the product $a_i \cdot a_j$, see Eq. 5.2. By indicating with the letters C and A the clockwise and anti-clockwise configuration, respectively, there are four possible combinations: CCC, CCA, CAC

[2] http://www.amsuper.com

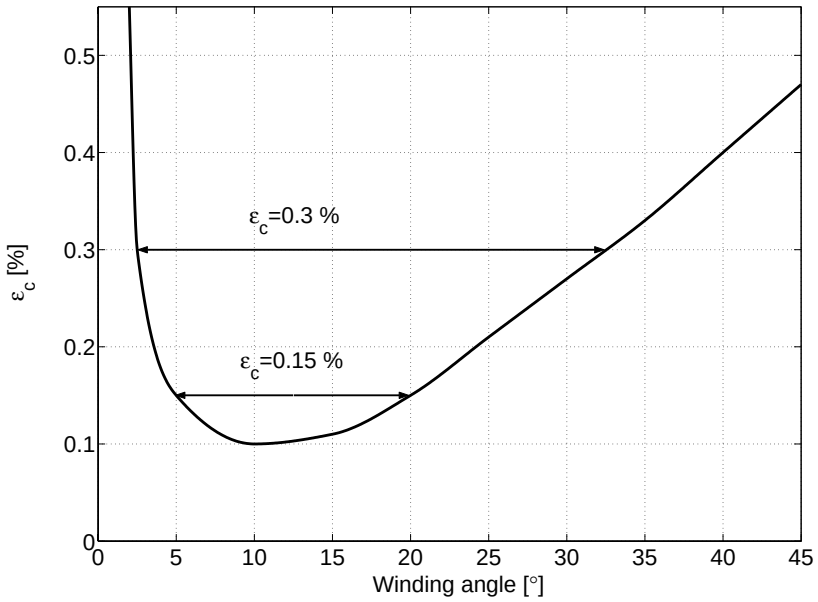

Figure 5.4: Typical curve of the critical strain as a function of the winding angle. The radius of the layer is 12.5 mm. Tapes with $\epsilon_c = 0.3\%$ allow the use of a wider range of angles.

Layer1 (cm)	Layer2 (cm)	Layer3 (cm)
61	38	22
62	38	22
65	39	22
66	39	22
67	39	22
70	40	22
71	40	22
72	40	22
75	41	22
76	41	22

Table 5.3: Ten best pitch lengths for the 3-layer cable. The absolute minimum of the parameter W is obtained with pitch lengths equal to 66 cm, 39 cm, 22 cm.

and CAA. The configurations AAA, AAC, ACA and ACC give the same values of the inductance matrix elements in Eq. 5.2 for symmetry reasons and need not be considered. In order to reduce the number of combinations to be tested, the possible pitch length in the selected range has been varied first with steps of 2 cm and it has been found that the most even current repartition occurs with the CCC orientation of the layers. Therefore, for this orientation only, the pitch length has been varied from 22 cm to 76 cm, with steps of 1 cm, which makes $55 \times 55 \times 55 = 166,375$ combinations. Simulated are two cycles of sinusoidal current at 50 Hz. On a personal computer equipped with a 2.4 GHz processor, the complete simulation of all the possible configurations lasts about three days.

The deviation of the transport current in the three layers from the perfectly uniform repar-

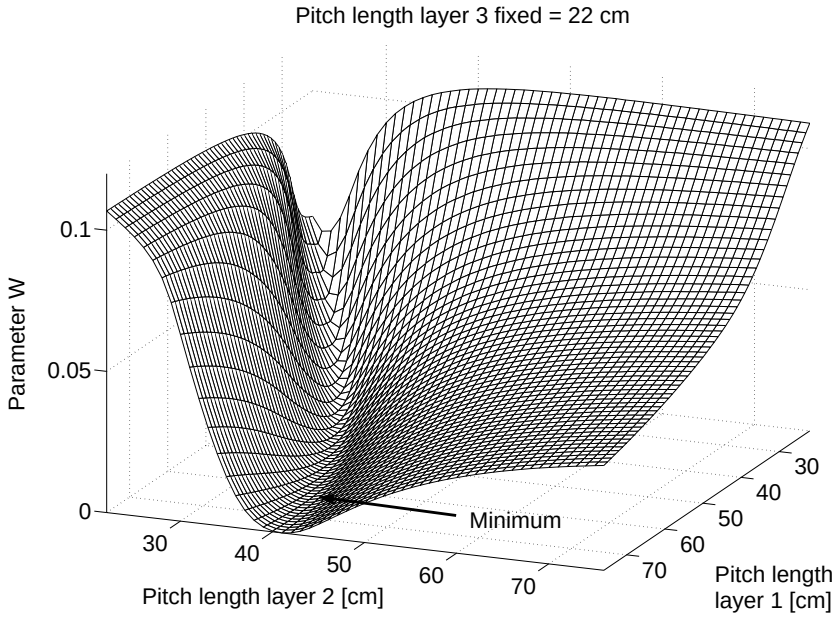

Figure 5.5: Parameter W as a function of the pitch length of the first and second layer, with the pitch length of the third layer kept fixed to 22 cm.

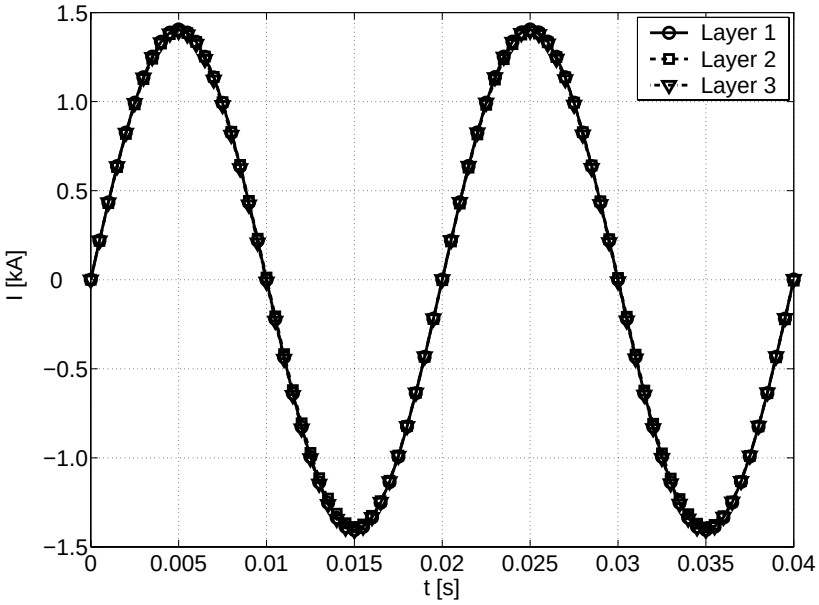

Figure 5.6: Repartition of the current in the optimal configuration (66 cm, 39 cm, 22 cm), obtained with the macroscopic model. The layers carry practically the same current, about 1.4 kA.

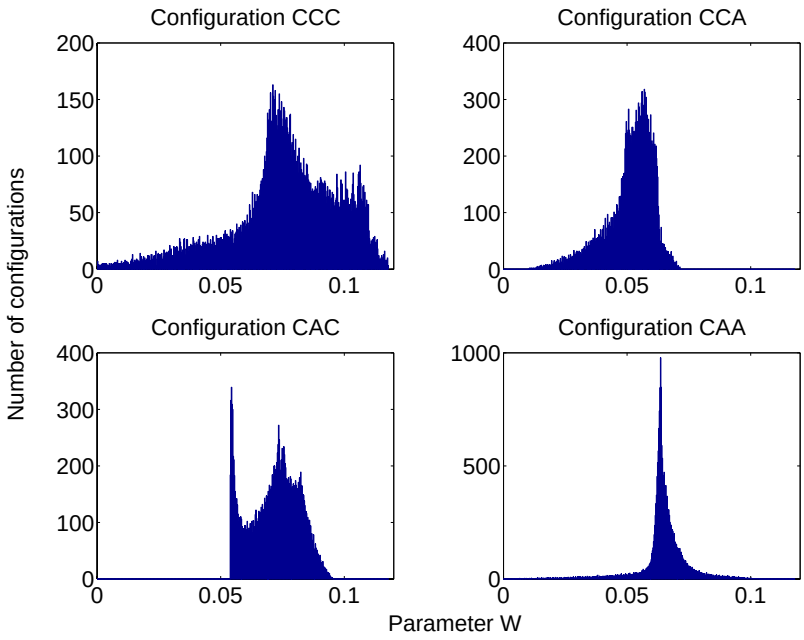

Figure 5.7: Histogram of the number of configurations as a function of the optimizing parameter W. Uniform current repartitions correspond to $W \lesssim 0.005$.

tition has been chosen as optimizing criterion, as follows:

$$W = \frac{f}{2I_{tot}^2} \sum_{i=1}^{3} \int_T (I_i(t) - \frac{I_{tot}}{3} sin(\omega t))^2 dt, \tag{5.7}$$

where I_{tot} is the amplitude of the total current, $I_i(t)$ is the current flowing on the i-th layer, f is the frequency, T is the second simulated cycle. The division by I_{tot}^2 and the multiplication by f have been added for obtaining a value of W in the range [0,1] and for normalizing to the during of one period. The optimal configuration results to have the layers oriented in the same direction (CCC), in agreement with theoretical calculations [56]. Table 5.3 lists the pitch lengths of the three layers in the ten best optimal configurations. In all cases the optimal pitch length decreases from the inner to the outer layer.

The parameter W is a function of the current distribution among the layers, which depends on the three pitch lengths. For visualizing a plot, its dependence on the pitch length of two layers can be drawn, with the pitch length of the other layer kept fixed. An example is reported in Fig. 5.5, which displays the parameter W for different values of the pitch length of the first and second layer, with the one of the third layer kept fixed to 22 cm. The optimal configuration (identified by the minimum W) is given by the lengths 66 cm, 39 cm, see also Table 5.3. With these three pitch lengths, the repartition of the current among the layers is perfectly uniform, as displayed in Fig. 5.6. The picture refers to a total transport current of 4.2 kA, which corresponds to the effective critical current of the three-layer cable analyzed in section 5.4.

Figure 5.7 shows the number of configurations corresponding to given values of the parameter W. The lowest values of W are obtained with the CCC winding. In addition, quite uniform current repartitions correspond to $W \lesssim 0.005$; this range of values can be obtained with the CCC configuration only.

Finally, the method has been tested on a four-layer HTS cable, with the same physical parameters of the analyzed three-layer cable and with an additional layer with average radius

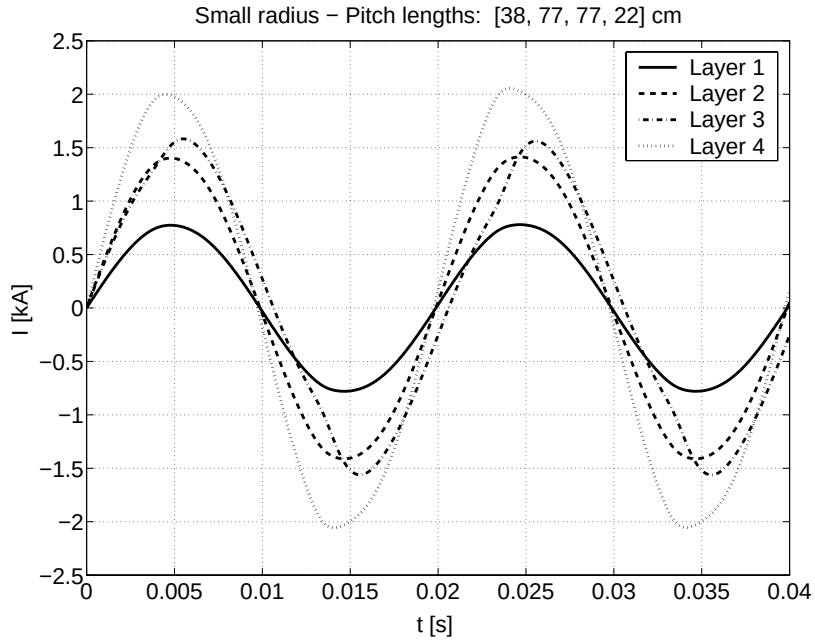

Figure 5.8: Current distribution in the optimal configuration with a former radius of 14 mm.

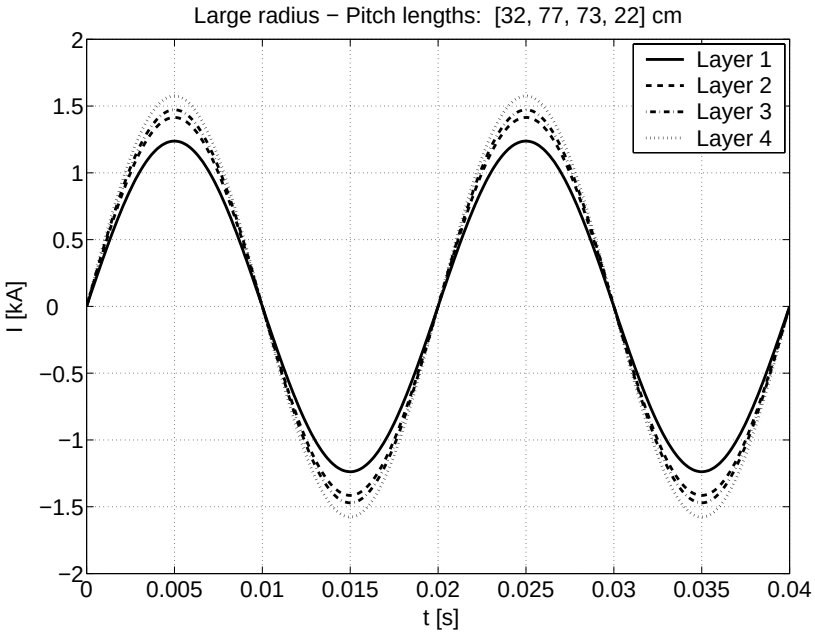

Figure 5.9: Current distribution in the optimal configuration with a former radius of 19 mm.

of 17.04 mm. It has to be noted that considering the same range of 55 possible pitch lengths increases the number of possible configurations by a factor $110 = 2 \times 55$ and consequently the total computation time. In fact, there is one more layer (with its possible 55 angles) and the number of relative orientations is 8 instead of 4. In this case a coarse range of good configurations has been determined, by making the pitch length vary from 22 cm to 77 cm with steps of 5 cm. The orientation assuring an even repartition of the current is CCAA, again in agreement with

theoretical predictions [56]. In particular, the best configuration resulted to be [37, 77, 77, 22] cm. After that, for the CCAA orientation only, the pitch lengths has been varied in the range [32 → 42, 67 → 77, 67 → 77, 22 → 32] cm. The best configuration resulted to be [38, 77, 77, 22] cm.

The results of this analysis confirm that, in the case of four-layer HTS cables, the best winding orientation is CCAA and the layers have to be wound with short pitch length at the interior and exterior (layer 1 and 4) and with long pitch length in the middle (layer 2 and 3). Actually, this is the typical configuration utilized by manufacturers, see for example [57, 58]. Nevertheless, the repartition of the current among the layers is far from being uniform, see Fig. 5.8.

In terms of current repartition, better results can be obtained by using a larger former. With the same cable properties, but with a former (and consequently a layer radius) 5 mm larger, the optimal current repartition results to be much more uniform. In this case, the optimal configuration is [32, 77, 73, 22] cm and the corresponding current repartition is displayed in Fig. 5.9.

At this point a remark is necessary about the effects of the magnetic field generated in the internal part of the cable. In the case of the three-layer cable, with the CCC configuration it is possible to have a uniform repartition of the current among the layers. Since the layers are oriented in the same direction, an axial magnetic field is produced at the interior of the cable. The variation of the flux of the field across the cable section produces a voltage $V = -d\Phi(B)/dt$ at the cable ends, which might constitute a problem, especially for long samples.

The amplitude of the axial magnetic field generated by a current $I = 1.4\ kA$ over one metre of cable is given by

$$B_{axial} = \frac{\mu_0 I}{l_p} = \frac{4\pi 10^{-7} 1.4 \cdot 10^3}{l_p}. \tag{5.8}$$

For the layer with the shortest pitch length (22 cm), the amplitude of the field is about 8 mT. The corresponding induced voltage is

$$V = \pi r^2 B_{axial} \omega. \tag{5.9}$$

With an average radius of 15 mm and a frequency of 50 Hz, the induced voltage over 1 m of cable is about 1.8 mV. This voltage is not important for short samples (few metres), but it can become relevant for very long ones (hundreds of metres).

Four-layer HTS cables do not have this problem, because the layers are wound with alternate configuration, so that the field generated in the internal part of the cable is very small, due to the compensation between the layers wound in opposite direction.

5.4 FEM simulations of a HTS cable

Once the geometrical configuration corresponding to a uniform repartition of the current has been found, 2D FEM computations can be used for evaluating the AC losses.

For FEM simulations the $J_c(\mathbf{B})$ model given by Eq. 4.10 has been used; it has been adapted by taking into consideration the circular arrangement of the tapes around the cylindrical former. In practice, the utilized model corresponds to the one used for the wire with peripheral arrangement of the filaments, see Fig. 4.15.

For the superconductor the parameters $J_{c0} = 2 \cdot 10^8\ A/m^2$, $n_0 = 21$ have been used. The product of J_{c0} times the total superconductor section gives a total critical current for the cable of 5.2 kA. As it will be shown later, the effective critical current is much lower, about 4.2 kA, due to the reduction of the local J_c caused by the self-field. The normal metal matrix of the tapes has been assigned a conductivity $\sigma_{Ag} = 5 \cdot 10^8\ S/m$. In most of the analysis which follows,

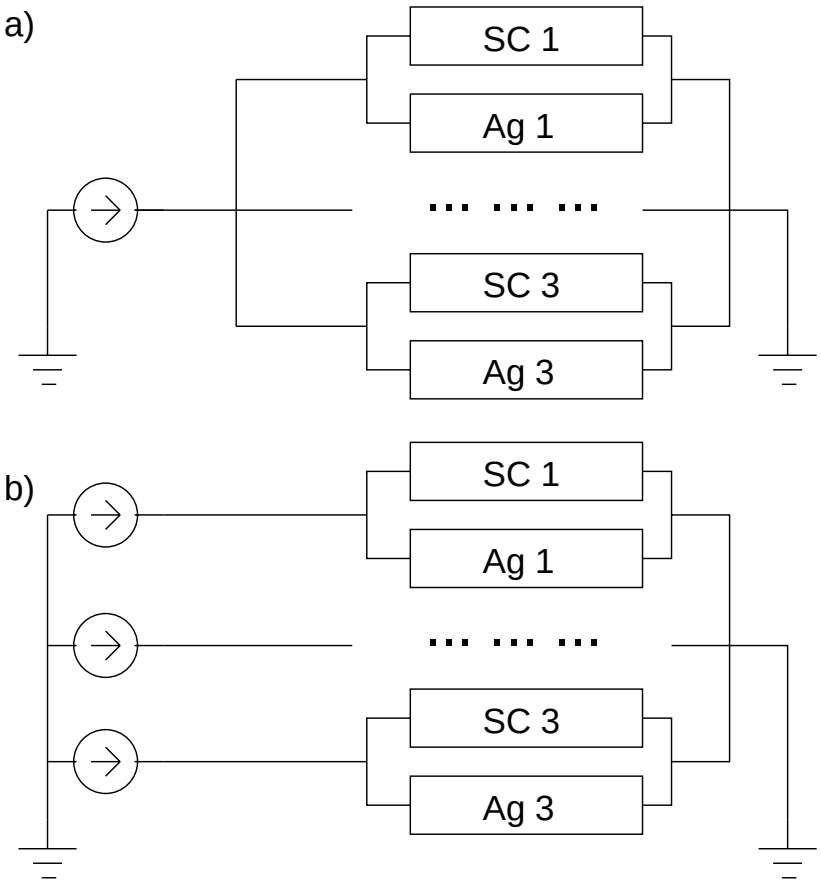

Figure 5.10: Electrical circuits used for FEM simulations. The circuit with one current source (a) corresponds to the simulation of a straight cable. The circuit with three independent current sources (b) has been used to inject the desired current in each layer.

a working condition of total transport current equal to 4.2 kA, which corresponds to the total effective critical current, has been chosen. The frequency of the source has been set equal to 50 Hz.

In order to reduce the size of the problem (number of nodes of the mesh) and the computation time, only an angular sector (1/20) of the whole cross-section has been considered for FEM simulations, see Fig. 5.12. Periodicity conditions have been applied on the domain boundary in order to take into account the full geometry.

5.4.1 Effects of the magnetic field

The total transport current has been kept constant (at 4.2 kA) and the current flowing in the individual layers has been varied by means of three independent current sources, see Fig. 5.10. In particular, more current has been forced to flow in the internal part of the cable (which has in principle a higher critical current, due to the lower experienced magnetic field), in order to see if this is more convenient from the point of view of AC losses. Table 5.4 lists the repartition of the current in the four analyzed configurations and the corresponding AC losses in the superconductor.

Due to the cylindrical structure of multi-layer cables, the external layer is always subjected to a larger magnetic field than the others. This means that even with a perfectly uniform repartition of the current, the outer layer has larger AC losses. In addition, the reduced effective transport

Name	Layer1	Layer2	Layer3	Losses (W/m)
Uniform	1400 A	1400 A	1400 A	1.88
Test 1	1500 A	1400 A	1300 A	1.85
Test 2	1550 A	1450 A	1200 A	1.85
Test 3	1600 A	1400 A	1200 A	1.98
Test 4	1700 A	1400 A	1100 A	2.34

Table 5.4: Analyzed current repartitions and corresponding AC losses in the individual layers, computed by FEM simulations.

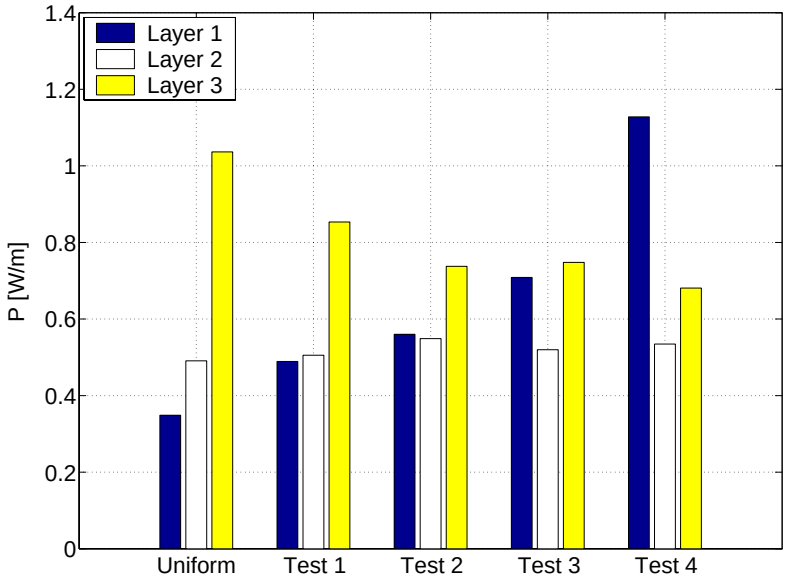

Figure 5.11: AC losses in the different layers for different repartitions of the transport current, evaluated by FEM computations. The "Test 1" and "Test 2" configurations have the most uniform repartition of the losses among the layers.

capacity of the outer layers (according to Eq. 4.10) gives a further contribution to the losses. In particular, in the case of perfect uniform repartition of the current, there is a difference of a factor three between the losses in the outermost and innermost layer, see "Uniform" configuration in Fig. 5.11. The effects of the field are visible by looking at the repartition of the losses among the layers, which is more uniform in the "Test 2" and "Test 3" configurations, when more current flows in the inner layer, as shown in Fig. 5.11. The total losses are also slightly lower than in the "Uniform" configuration, but not in a remarkable way (only about 1.5%). In fact, the higher magnetic field generated by the internal layers keeps the losses in the outer layer at a high value, so that the advantage coming from making more current flow in the inner part of the cable is compensated by the higher generated magnetic field in the outer part.

Figure 5.12 shows the magnetic field distribution on a transverse cross-section of the cable for an applied total transport current of 4.2 kA at the peak value, in the case of a perfect uniform repartition. The magnetic field is directed almost parallel to the flat face of the tapes and reaches locally a maximum value of about 50 mT in the outer layer. A magnetic field of this amplitude, even if directed parallel to the tapes, causes a reduction of the local critical current density by about 25%, according to Eq. 4.10, and a significant decrease of the transport capacity

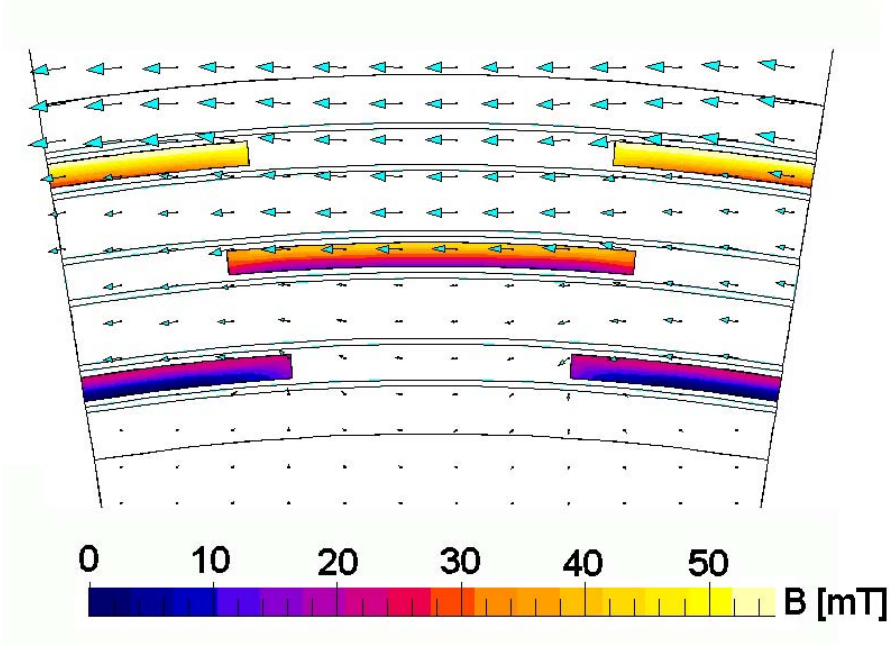

Figure 5.12: Magnetic field distribution for a transport current $I = 4.2\ kA$ at the peak value. The field is directed almost parallel to the tapes and reaches locally a value of about 50 mT in the outer layer.

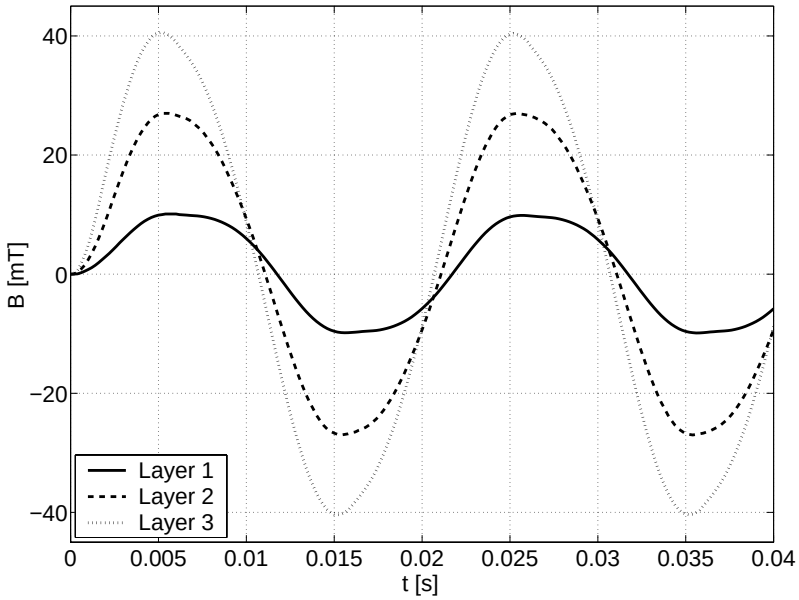

Figure 5.13: Time evolution of the average parallel magnetic field B^* in the three layers for a transport current $I = 4.2\ kA$ equally shared by the layers.

of the whole cable, as it will be shown later.

Figure 5.13 displays the time evolution of the average parallel magnetic field B_i^* in the tapes of each layer in the case of a total transport current of 4.2 kA, perfectly shared by the three

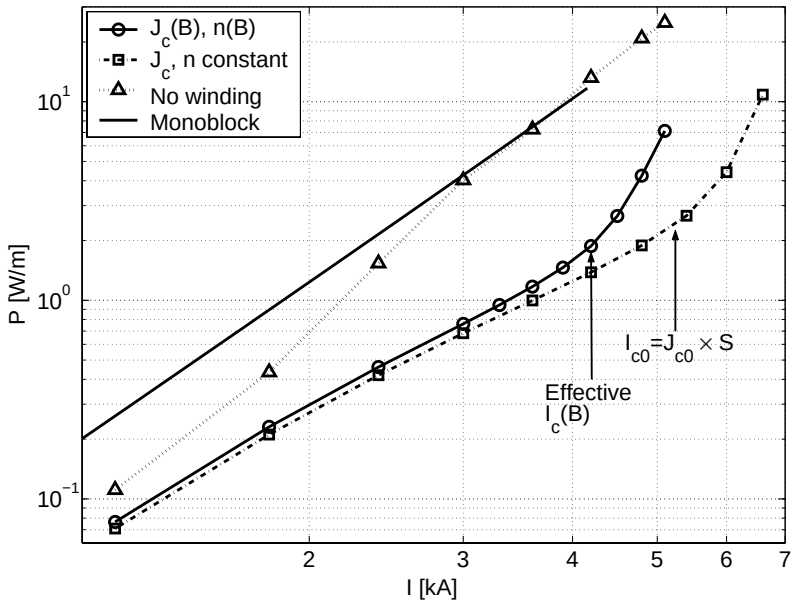

Figure 5.14: AC losses in the HTS cable computed by different models.

layers (1.4 kA each). The average parallel field acting on the surface S of one tape of the i-th layer is computed as follows:

$$B_i^* = \frac{1}{S} \iint_{tape} B_{\parallel} \cdot dS \quad i = 1, 2, 3. \tag{5.10}$$

The amplitude of the average parallel field undergone by the three layers is 10 mT, 27 mT and 41 mT, respectively.

5.4.2 Performance of the cable with a uniform current repartition

The transport capacity of the cable is strongly affected by the decrease of the critical current density due to presence of the magnetic self-field. For obtaining a uniform current repartition in the FEM simulations, three independent current sources have been used to inject the same current in each layer. Figure 5.14 displays the results obtained with different FEM models. The most important result is the significant difference of the losses between the constant-J_c and the $J_c(\mathbf{B})$ model, both in the case of perfect uniform repartition of the current. The dependence of J_c on the magnetic field causes a decrease of the effective critical current, which may be identified by the change of the slope of the loss curve [46], from 5.2 kA (given by J_{c0} times the superconducting section S) to about 4.2 kA. The difference in the losses is particularly evident at high transport currents, whereas at low currents the two models nearly coincide, since the produced self-field is not high enough to reduce significantly the critical current. In addition, the results of the FEM simulations are well below the predictions of the theoretical monoblock model [59]. This is in agreement with some experimental results found in the literature, see for example [51], [53], [60], [61]. In fact, the monoblock model considers the cable as a hollow superconducting tube with a transport current starting to penetrate from the exterior, which gives large losses.

Reported are also the losses computed with the $J_c(\mathbf{B})$ model in the case of a straight cable, without winding the layers ("no winding" in the legend). For this situation, FEM calculations

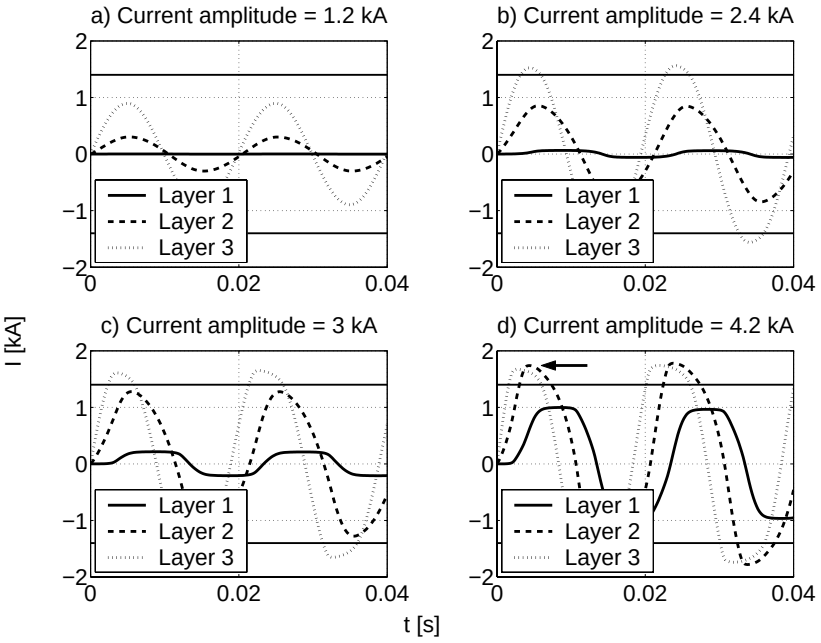

Figure 5.15: Repartition of the transport current among the three layers without winding the tapes (straight cable). Different total transport currents are displayed: 1.2 kA (a), 2.4 kA (b), 3 kA (c) and 4.2 kA (d). The critical current of the layers is approximately represented by the horizontal lines (1.4 kA).

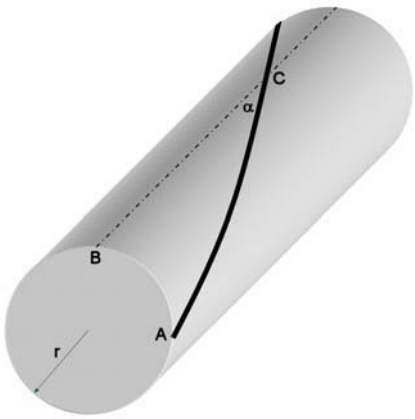

Figure 5.16: Sketch of a superconducting tape wound around a cylindrical support.

have been performed by feeding in parallel the three layers with only one current source, see Fig. 5.10a. In this case the cable behaves like a round wire: the current tends to flow in the outer part of the cable, whereas the inner part is scarcely utilized, as shown in Figs. 5.15a-d. At high transport current (3-4 kA) the losses are very close to the ones predicted by the monoblock model, which is based on the same principle of filling the cable section with current from the exterior to the interior, progressively saturating it. The agreement does not occur at low transport current (1-2 kA), because with the "no winding" model the layers are not saturated (see Fig. 5.15a-b) and the losses are consequently lower than the ones of the monoblock model.

At 4.2 kA the current in the outer layers exceeds the critical value (which is about 1.4 kA, as

marked by the horizontal line) and gives rise to very high AC losses, due to the rapid increase of the voltage for overcritical currents. In Fig 5.15d it is interesting to note that the second layer saturates at a higher value of the current than the third one (as indicated by the arrow): this is a further confirmation that the effective critical current of the external layer is more importantly reduced by the magnetic field, which is higher in the external part of the cable.

On the contrary, when the current is uniformly repartitioned, none of the layers exceeds the critical value (see Fig. 5.6) and the losses are consequently much lower.

At this point, a small remark about the quantitative evaluation of the AC losses is necessary. The losses have been computed for 1 m of cable length, which corresponds to different lengths of the tapes in the layers. Therefore, the results from 2D FEM simulations have to be multiplied by the effective length of the tape in 1 m of cable. The actual length of the tape depends only on the winding angle of the layer, as can be derived from the sketch in Fig. 5.16: the effective tape length with respect to the cable length is given by the ratio $AC/BC = 1/\cos\alpha$.

For the considered geometry, the winding angles of the three layers are 8.1°, 14.1°, 25.0°, respectively. The corresponding corrective factors $1/\cos\alpha_i$ are 1.01, 1.03 and 1.10, so that the total effective losses are not substantially different from the results obtained directly from FLUX3D.

5.5 Influence of non-uniform tape properties

The global performance of a HTS cable depends on the transport properties of the individual tapes, which in general may present different values of the critical current I_c and/or the power index n, as well as different contact resistances with the source used to inject the transport current. The contribution of such non-uniformities to the global performance of a single-layer cable has been studied separately by means of FEM computations. The FEM analysis is validated by means of a comparison with experimental measurements of the AC losses as well as with the results obtained with another simpler electrical model, which has been recently proposed in [62]. The cable has been assembled by Pirelli[3]; the experimental measurements have been performed by Fedor Gömöry's group at the Slovak Academy of Sciences[4].

5.5.1 Characterization of the cable sample

The manufactured cable consists of a single layer composed by sixteen straight superconducting Bi-2223/Ag tapes, 107 cm long. An epoxy-fiberglass mandrel was provided with trenches to house the tapes and avoid any uncontrolled movement or electrical contact between them. The transport properties of the tapes have been measured in DC experiments. DC current was supplied to the cable as a whole, and the portion passing through the tape under study was determined with the help of the brass rods connected in series to each tape, see Figs. 5.17-5.18. Plotting the voltage signal registered on a single tape with respect to the tape current allowed to determine the parameters characterizing the superconducting transition, which are summarized in Table 5.5. The table also reports the value of the contact resistances (including the resistance of the rod and the whole copper termination for each tape), which has been obtained from the initial part of the current-voltage plots. The circuit model of the cable is shown in Fig. 5.19.

[3]Pirelli Labs, Viale Sarca 222, 20126 Milano, Italy
http://www.pirelli.com

[4]Department of Superconductor Physics, Institute of Electrical Engineering, Slovak Academy of Sciences, 84104 Bratislava, Slovak Republic
http://www.elu.sav.sk

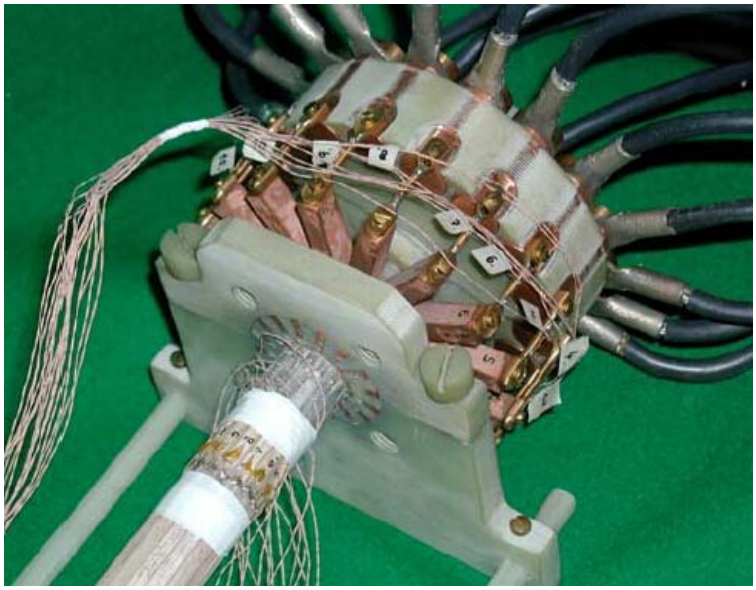

Figure 5.17: Current termination head of the cable model. Brass rods for measurement of current distribution in DC tests can be seen.

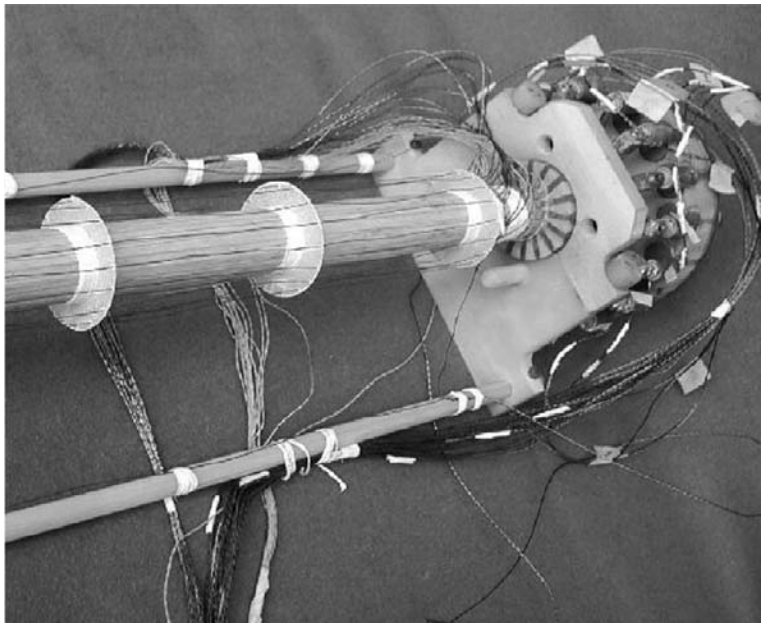

Figure 5.18: Large view of the cable sample. The thin wires used for the loss measurements can be seen, about 1 *cm* from the cable surface.

5.5.2 FEM simulations with non-uniform tape properties

In order to investigate the influence of the contact resistances, of the critical current and of the power index of the tapes by means of FEM simulations, each parameter has been varied separately and the other two have been kept equal to their average experimental value: $R^* = 89.39\ \mu\Omega$, $I_c^* = 31.74\ A$, $n^* = 23.11$, see Table 5.5. As a working condition for studying the influence of non-uniformity, a voltage amplitude of $0.13\ V$ has been chosen for the source: it corresponds to a transport current of about $500\ A$ (peak value), which is approximately the

Tape no.	R [$\mu\Omega$]	I_c [A]	n	Tape no.	R [$\mu\Omega$]	I_c [A]	n
1	95.088	32.8	23.5	9	105.94	31.0	23.0
2	94.169	30.6	22.0	10	83.741	30.8	23.0
3	89.916	31.9	22.9	11	88.395	31.2	22.5
4	92.091	31.0	23.0	12	93.696	32.6	23.5
5	90.872	31.9	23.5	13	89.937	33.6	24.5
6	74.020	32.1	23.2	14	80.449	31.7	23.0
7	76.779	31.7	23.2	15	98.130	32.2	23.0
8	84.549	31.2	23.0	16	92.425	31.5	23.0
Average values: $R^* = 89.39\ \mu\Omega$, $I_c^* = 31.74\ A$, $n^* = 23.11$							

Table 5.5: DC characterization of the cable.

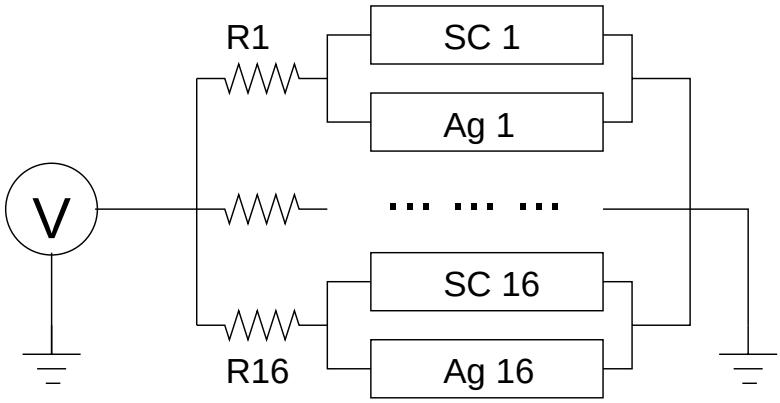

Figure 5.19: Electrical circuit of the cable used for modelling.

effective critical current of the cable, see Fig. 5.22.

Firstly, the contact resistances have been varied according to experimental values. Fig. 5.20 displays the current evolution in the first two periods, obtained by FEM simulations, in the uniform case (a) and with spread contact resistances (b), and the corresponding instantaneous AC losses. In the first case the curves fall very close to each other, practically superposing, whereas in the second case there is a spread of the current amplitude according to the value of the resistance: for example, tape no.9, which has the highest contact resistance, carries less current and has the lowest AC losses, as indicated by the arrow in the bottom-right diagram. The AC losses in the various tapes are shown in Fig. 5.21, which refers to different cases: the uniform configuration, the spread of contact resistances, the spread of critical currents, the spread of the power index and, finally, the real case, where all the three parameters have their real value, which is different for all the tapes. The AC losses are computed as usual, by using Eq. 4.1. The spread of the contact resistances causes quite different AC losses in the various tapes. However, due to a compensating effect between the tapes having higher and lower AC losses, the sum of the losses of the various tapes practically coincides with the one of the uniform case, as shown in the legend. The results are similar with the spread of the critical currents, which has been obtained by assigning different values of J_{c0} to the different tapes, according to the experimental distribution of I_c: in this case the variations about the average value are even smaller, and the total losses are again the same as in the uniform case. The spread of the power index n has no practical influence even on the behaviour of the individual tapes. Reported are also the losses of the real case (simultaneous variation of all the parameters), which give larger variations around the average value. Again, the global behaviour of the cable is not affected by such variations. According to these results, the spread of the parameters influences only the

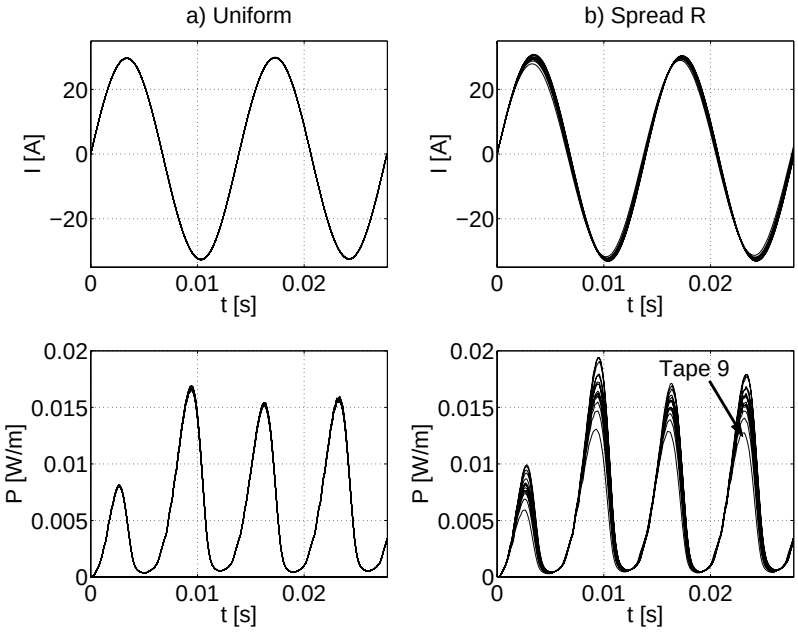

Figure 5.20: Current (top) and AC losses (bottom) evolution in each tape obtained by FEM simulations with uniform parameters (a) and with the spread contact resistances (b). The arrow indicates the losses in tape no.9, which, having the highest contact resistance, carries less current and has the lowest AC losses.

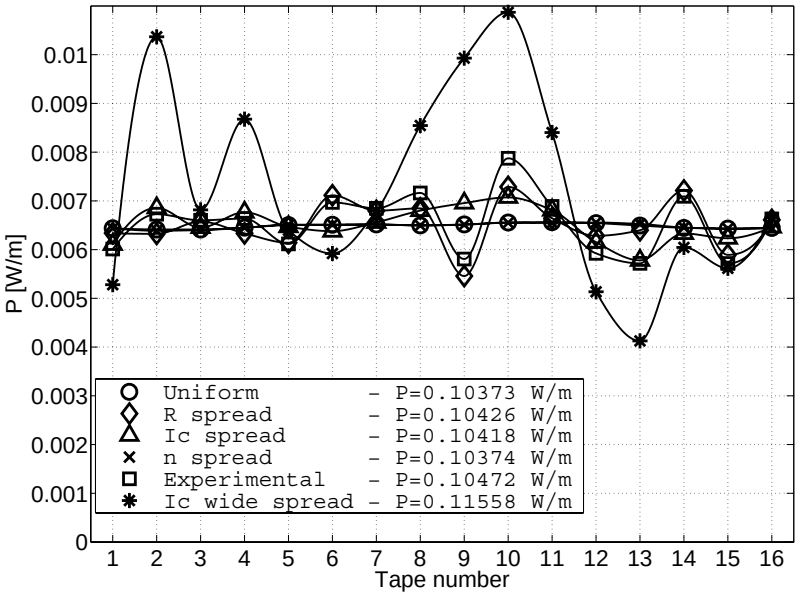

Figure 5.21: AC losses in the individual tapes for different kinds of non-uniformity, evaluated by FEM. In the legend the total AC losses in the cable are also given. The lines are just eye-guides.

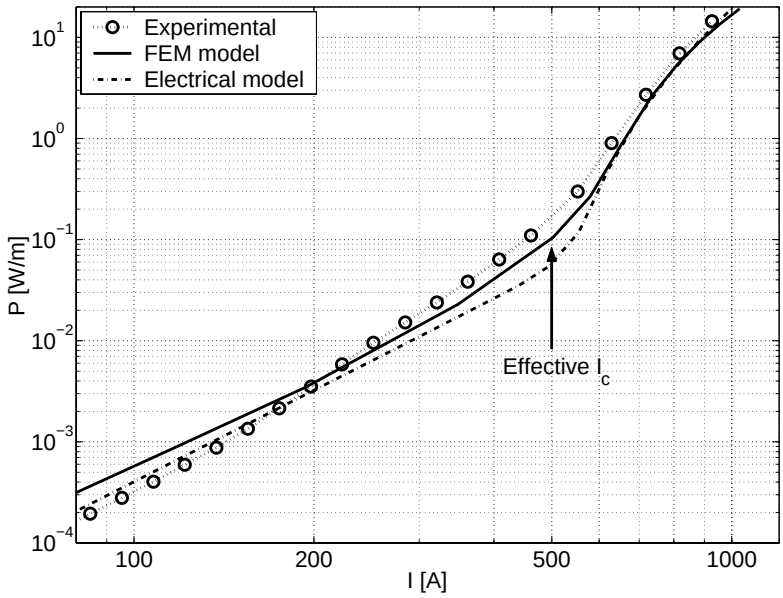

Figure 5.22: AC losses as a function of the transport current flowing in the cable (peak value). Compared are the experimental data and two numerical models, FEM and electrical. The arrow indicates the effective critical current, identified by the change of the slope of the curve.

individual behaviour of the tapes, but not the global performance of the cable. Furthermore, since the influence of the contact resistance decreases with the length of the cable [52], this means that in long samples the uniformity of the contact resistance is not a key-parameter for the current repartition and can be neglected. For long samples the most important non-uniform parameter is therefore the critical current. The simulations have shown that a variation of the critical current of the tapes of about 5% around the average value (as in the simulated case) causes variations in the losses of the individual tapes, but not in the ones of the whole cable. In order to see if a larger spread of I_c influences the total loss of the cable, the distribution of J_{c0} has been artificially widened by a factor 5 around the average value. Figure 5.21 also shows the losses of the individual tapes for this case. As expected, the variations are very large and follow the same shape of the "small" spread of I_c. This influences the total losses of the cable, which increase, but only by about 10%. Additional simulations have shown that a similarly widened distribution (i.e. by a factor 5 around the average value) for the power index n does not influence the losses of individual tapes.

The obtained results indicate that, for simulating multi-layer HTS cables with macroscopic models, each layer can be treated as a single conductor. As a matter of fact, this has been done in the search of the optimal pitch lengths at the beginning of this chapter and will be done with the equivalent circuit model, which is presented in the next section.

5.5.3 Validation of the model with experimental measurements

For validating the utilized FEM model, a comparison with electrical measurements of the AC losses has been made. In this experiment, the current and the voltage in individual tapes have been registered for each value of the cable total current. For voltage signals, the wires carrying the signal from voltage taps were placed 1 *cm* far from the cable surface to obtain true loss signal [63], see Fig. 5.18. Currents in individual tapes were determined with the help

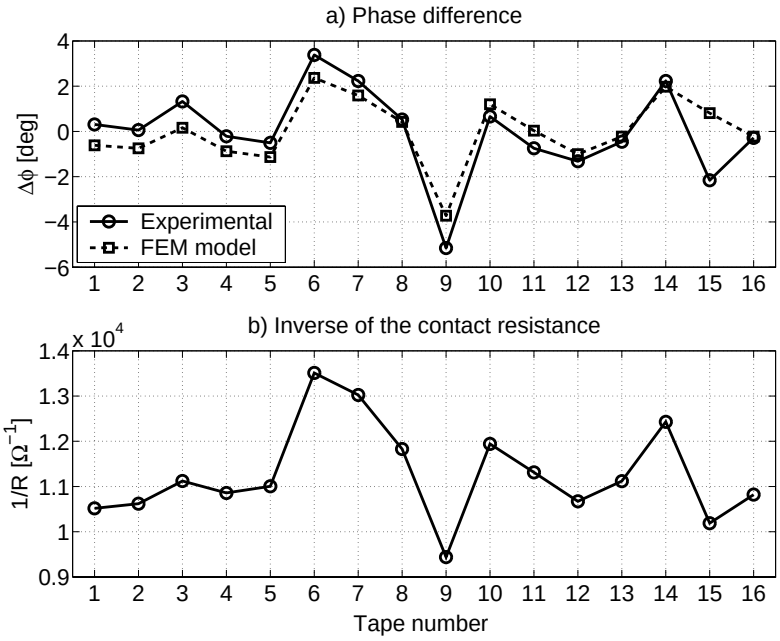

Figure 5.23: Phase shift of the current in the tapes with respect to the total current (a). Inverse of the contact resistance of the different tapes (b), see also Table 5.5. The lines are just eye-guides.

of miniature Rogowski coils wrapped around the brass rods put in every branch of the cable. The signals were led to lock-in amplifier to distinguish the component in phase with the total current in the cable. Figure 5.22 displays the experimental AC losses as a function of the transport current, together with the results of FEM calculations and of another simpler model, which considers the tapes from the macroscopic point of view, without computing in detail the current and field distributions inside the tapes [62]. According to this latter model, the losses are computed as the sum of two terms: $P = P_{mag} + P_{res}$. The first describes the self-magnetization losses, according to Norris's predictions [31], whereas the second takes into account the losses in the superconductor due to the flux creep as well as the losses in the silver due to the excess of transport current in the superconductor. The models are in substantial good agreement with the measurements: the slope of the curve is close to the experimental one as well as the bending point, which identifies the effective critical current of the cable ($\simeq$ 500 A). The agreement is very good for overcritical currents. The discrepancy between the FEM and the macroscopic model is probably due to the fact that the magnetic field effects are not taken into account by the latter. The difference between FEM computation and measurements can be imputed to different reasons, such as the not perfect regularity of the sinusoidal current during the measurements and to the fact that, for sake of size and time saving, the multi-filamentary tapes have been modelled as mono-filamentary, which influences to a certain extent the numerical results. A more detailed knowledge of the internal geometrical structure of the tapes (size and arrangement of the filaments) is necessary for obtaining results closer to the experiment.

FEM simulations have given results in very good agreement with experimental measurements in the determination of the phase shift of the current flowing in each tape. Figure 5.23a displays the phase shift of each tape with respect to the total current experimentally measured and given by the FEM calculations. The agreement between measurements and simulations is very good, with the exception of only one point, corresponding to tape no.15. The phase shift is related to the non-uniformity of the contact resistance, as can be seen from Fig. 5.23b.

5.6 Equivalent circuit model of HTS cables

For the prediction of the current repartition among the layers and the computation of the AC losses, another approach is possible. Presented in this section is an equivalent circuit model of HTS cables, which is somehow halfway between the electrical model and the FEM simulations presented in sections 5.3 and 5.4, respectively[5].

This model, developed for describing the hysteretic behaviour of superconductors, has been originally proposed by Mårten Sjöström in his Ph.D. thesis [64]. In that work it has been mainly used for separating the different contributions to self-field AC losses in HTS tapes. In this thesis work the use of this model has been extended to multi-layer HTS cables.

The equivalent circuit model considers the HTS cable (and any superconducting device in general) from the macroscopic point of view, without detailed information about the current and field distributions inside conductors. The main advantage of this model is that it does not need a detailed knowledge of superconductors and deals with global quantities, such as current and voltage, instead of local ones, such as current density and electric field. It is therefore particularly useful for studying problems on large scale, such as a grid of superconducting devices. For the simulation of individual tapes or cables, it is faster than FEM simulations. In addition, if coupled with a user-friendly graphical interface, its use becomes extremely simple, with no need to know the details of the software implementation.

5.6.1 Description of the model

In general, a superconductor with by-pass material can be modelled as a parallel of two branches, as displayed in Fig. 5.24: R_s is a non-linear resistance describing the resistive behaviour of the superconductor, R_b is the resistance of the by-pass material and L_{si} is a non-linear inductance for describing the hysteretic behaviour of the superconductor. This term is actually the kernel of the equivalent circuit approach and there are different possibilities for modelling it: the solution adopted in Sjöström's thesis (which has been followed here) has been the Preisach model [65]. The equivalent circuit model also contains two linear inductances, one for the superconductor and one for the by-pass material, describing the magnetic coupling of the two branches.

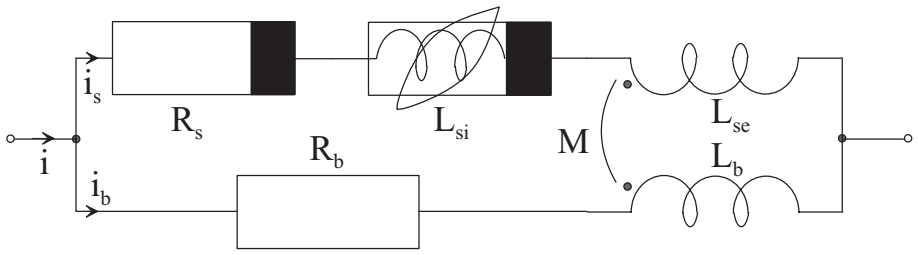

Figure 5.24: Equivalent circuit model for a superconductor with by-pass material.

The model has been extended to multi-layer HTS cables, as schematically shown in Fig. 5.25, with the further simplification of neglecting the by-pass material. The cable is modelled in terms of layers and not in terms of tapes. This is a fair assumption, because the non-uniformity in the transport properties of the individual tapes scarcely influences the global performance of the layer, as it has been demonstrated in section 5.5.

As in the case of the electrical model treated in section 5.3, the contact resistance between the tapes and the current source can be easily inserted; but, again, it has been neglected, due

[5]In this section the notation is sometimes slightly different from the one utilized so far. In particular, the winding of the layers is expressed in terms of *winding angle* instead of *pitch length*. The AC losses are computed in $J/(cycle \cdot m)$ instead of W/m.

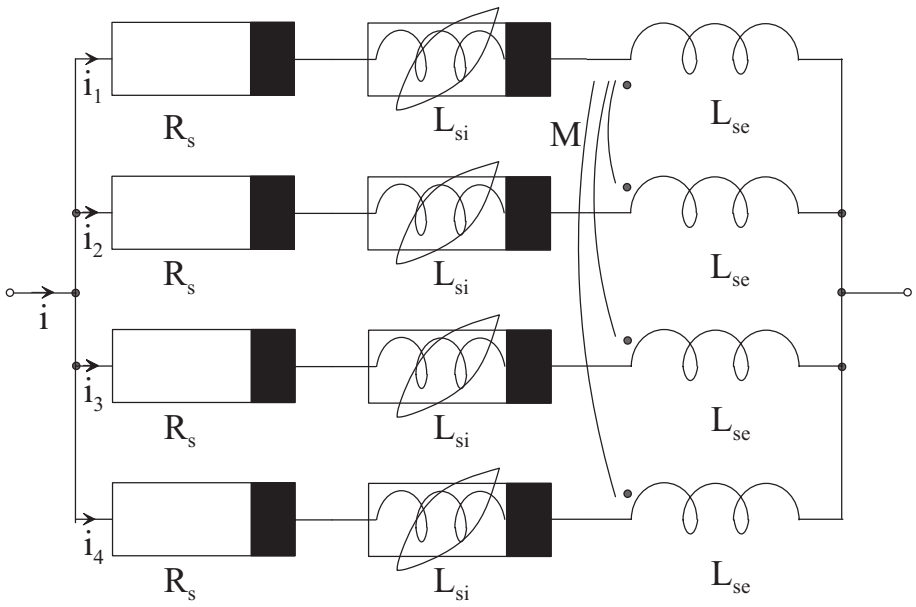

Figure 5.25: Equivalent circuit used to simulate a four-layer HTS cable.

Cable length l $[m]$	1
No. of layers n_l	4
Radius layer 1, r_1 $[m]$	$19.88 \cdot 10^{-3}$
Radius layer 2, r_2 $[m]$	$20.60 \cdot 10^{-3}$
Radius layer 3, r_3 $[m]$	$21.32 \cdot 10^{-3}$
Radius layer 4, r_4 $[m]$	$22.04 \cdot 10^{-3}$
Radius of return path, D $[m]$	$44.08 \cdot 10^{-3}$
Minimal winding angle, layer 1–4, φ_{min} [°]	10
Maximal winding angle, layer 1–4, φ_{max} [°]	38
Critical current, layer 1–4, I_{ck} $[A]$	1200
Power index, layer 1–4, n	21

Table 5.6: Cable parameters

to the fact that it is the inductive behaviour of the cable which most importantly influences the current repartition among the layers in long samples [52]. The equivalent circuit model has been used for studying the current repartition and computing the AC losses in a four-layer HTS cable, whose geometrical and physical parameters are listed in Table 5.6. In the presented analysis, the winding of each layer is described in terms of winding angle instead of the pitch length. The two parameters are linked through the radius of the layer: $l_{pk} = 2\pi r_k / \tan(\phi_k)$. Positive or negative values of the angles correspond to clockwise or anticlockwise orientation of the layer, respectively. The non-linear resistance of each layer R_k is derived from the $V - I$ power-law (2.18):

$$R_{sk} = \frac{V_c}{I_{ck}} \left| \frac{i_{sk}(t)}{I_{ck}} \right|^{n-1} + R_{0k} \qquad k = 1, ..., 4 \tag{5.11}$$

so that the resistive losses can be computed as

$$P_{res,k} = \int_0^T R_k(i_{sk}) i_{sk}^2 \, dt. \tag{5.12}$$

The Preisach model used for the hysteretic inductance consists of a superposition of an infinite

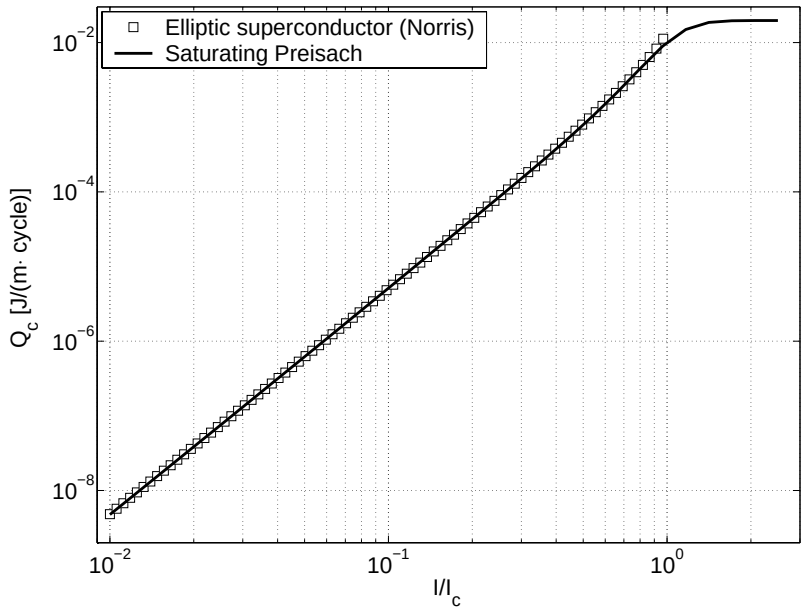

Figure 5.26: AC losses in the hysteretic inductance as a function of the transport current, normalized to I_c.

number of weighted relay-operators $\hat{\gamma}_{\alpha\beta} = \pm 1$, which are switches with up-switch at $i_k = \alpha$ and down-switch at $i_k = \beta$, $\alpha \geq \beta$. The flux Φ_k in the hysteretic inductance generated by the current i_k is then expressed by

$$\Phi_k(t) = \int \int_{\alpha \geq \beta} \mu(\alpha, \beta) \hat{\gamma}_{\alpha\beta}[i_k(t)] d\alpha d\beta \,, \tag{5.13}$$

which depends on the history of the current i_k. The flux is differentiated to give the voltage over the hysteretic inductance $v_{si(k)} = d\Phi_k/dt = L_{si,k}(i_k) \cdot di_k/dt$, which is made by differentiating the Preisach model directly, rather than the value of the flux [66].

The characteristics of the hysteresis are defined by the Preisach function $\mu(\alpha, \beta)$, where a superconductor can be modelled by using the following function:

$$\mu(\alpha, \beta) = \mu_0(\alpha - \beta) \cdot l_{\mathrm{u}}(\alpha) \cdot l_{\mathrm{l}}(\beta) \,. \tag{5.14}$$

The hysteresis then complies to the critical state model by using $\mu_0(\alpha - \beta)$, where the argument is the difference $\alpha - \beta$. A smooth saturation is obtained by using the limiting functions l_u and l_l [67], so that over-critical currents can also be taken into account. This is carried out by using the following Preisach functions:

$$\mu_{0,k}(x) = I_c \sum_{p=2}^{7} c_{p,k} \cdot \left(\frac{x}{2I_c} \right)^p , \tag{5.15}$$

where $c_{p,k} = 10^{-7} \cdot [0.9812, 0.8120, -2.0780, 3.3452, -1.3514, 0.1912] \cdot l_c / [n_s \cos \phi_k]$ for $p = 2, ..., 7$ and layers $k = 1, ..., 4$, respectively, by which the hysteretic inductances take into account the longer tape-lengths due to the winding angle ϕ_k. Furthermore, the hysteresis saturates when the current surpasses the critical current I_c in the cable layer, which is performed by the limiting functions

$$l_u(\alpha) = 1 + \exp[s \cdot (\alpha - I_s)]^{-1} \tag{5.16}$$

$$l_u(\beta) = 1 + \exp[-s \cdot (\beta + I_s)]^{-1}, \tag{5.17}$$

with $s = 8/I_c$ and $I_s = 1.05 I_c$. The resulting losses are depicted in Fig. 5.26.

The values of the linear self and mutual inductances L_{se} and M_{ij} are solely given by the geometry of the cable, see Eqs. 5.1-5.2.

Energy losses are produced in the resistances and the hysteretic inductances, whereas the linear inductances have no energy dissipation. The loss in each resistance is obtained by integration of the power loss over the time, whereas the hysteretic loss is computed with the Preisach function:

$$Q_{L_{si}}(t_0, t) = \int \int_{S(t_0,t)} \mu(\alpha, \beta)(\alpha - \beta) d\alpha d\beta, \tag{5.18}$$

where $S(t_0, t)$ is the surface the history function sweeps in the $\alpha - \beta$ plane [65].

5.6.2 Simulations and results

The investigation to find the winding angles and orientations that minimize the total loss in the described cable has been carried out by successively refined searches. Firstly (step 1), a rough search for the optimal solution was carried out by investigating all possible combinations of winding orientations and angles between 10° and 40° for all four layers, using a step size of 5°, giving a total of 19208 cases to investigate. These simulations were performed *without* a hysteretic inductance. Secondly, the full equivalent circuit *including* the hysteretic inductance was employed for winding angles and orientations in a vicinity of the previously obtained solution in two steps (step 2 and 3), each with the step-sizes of 2° and 1°, respectively. In that sense, a great deal of simulation time has been saved. In each step, 1.25 periods of a sinusoidal current source with an amplitude of $I_p = 3800\ A$ (0.8 of the total critical current) and a frequency of 50 Hz have been deployed using a time-step of $10^{-4}\ s$. The loss was computed over the last observed half-cycle in order not to take transients into account.

Simulating the cable with the equivalent circuit on a Pentium III of 1.2 GHz and 256 MB of RAM takes less than 5 s for the 1.25 cycles when excluding the hysteretic inductance (step 1), and approximately 10-70 s when including the hysteretic inductance (step 2, 3). (The fewer values of the currents above I_c, the faster the simulation.) The computation of both the hysteretic and the resistive losses over the last half-cycle is performed within approximately 3-4 s. As a comparison, a complete 2D FEM simulation of the cable lasts between 3 and 4 hours on a PC with 2 GHz processor and 2 GB of memory. Therefore, the advantage of using the equivalent circuit model for the present investigation becomes obvious.

5.6.3 Equal critical current and power-law exponent in all layers

In this part of the investigation, equal values of the critical current $I_c = 1200\ A$ and the power-law exponent $n = 21$ have been used for all of the cable layers. The results in step 1 reveal that the orientations CCAA for layers 1-4 are the most favourable for a minimized loss, where the combination of angles that produced the smallest total loss in the cable was $35°, 15°, -15°$ and $-40°$ for layers 1-4, respectively. The second step examined angles in the vicinity of this solution, see Table 5.7, whereby these 1008 cases took into account the limits of the winding angles. (C.f. Table 5.6.) The winding angles between $26° \rightarrow 28°$, $10° \rightarrow 12°$, $-16° \rightarrow -12°$, $-38° \rightarrow -36°$ for the respective layer produced the ten cases of smallest losses, so that in the third step the angles given in Table 5.7 have been chosen for consideration, a total of 480 cases. The number of winding combinations for a certain total loss is depicted in Fig. 5.27. The best combination of winding angles is: $25°, 10°, -13°, -36°$, which gives the total loss of 19.12 $mJ/cycle$. The corresponding current distribution across the layers results to be next to uniform, as depicted in the inset of Fig. 5.27. The figure shows that the currents in layer 1 and 4 are slightly smaller, which is due to the fact that these layers have the largest winding angles

Step 1:	step-size of 5°	
	Layer 1-4:	$-40° \rightarrow -10°$
		$+10° \rightarrow +40°$
Step 2:	step-size of 2°	
	Layer 1:	$+26° \rightarrow +38°$
	Layer 2:	$+10° \rightarrow +20°$
	Layer 3:	$-20° \rightarrow -10°$
	Layer 4:	$-38° \rightarrow -32°$
Step 3:	step-size of 1°	
	Layer 1:	$+25° \rightarrow +29°$
	Layer 2:	$+10° \rightarrow +13°$
	Layer 3:	$-17° \rightarrow -12°$
	Layer 4:	$-38° \rightarrow -35°$

Table 5.7: Considered angles for simulations.

and therefore contain the longest superconducting tape. For the considered winding angles in the vicinity of the optimum, the increase of the total loss is quite moderate, about 10-15%.

The results show that the good winding orientation is CCAA and the good angles are of the form (large, little, -little, -large), in agreement with theoretical calculations [56] and the configuration utilized by manufacturers [57, 58]. For random orientations of the layers, the current is far from being partitioned uniformly, and so the loss is higher, as demonstrated in Fig. 5.28a-b. Even if the optimization has been carried out at about $0.8 \cdot I_{c,tot}$, the current distribution remains approximately the same also when the current approaches the total critical current, see Fig. 5.28c-d. The total losses in the optimized cable are presented in Fig. 5.29, together with the hysteretic and resistive contributions. Displayed are also the losses computed by the monoblock model, which are well above those computed by the equivalent circuit model for the optimal configuration of the cable. The inset of Fig. 5.29 depicts the power loss in each layer during the time of the simulation. The losses of layer 3 and 4 are the largest and almost equal, so the graphs are difficult to separate. The losses produced in the first half-period are smaller because the superconductor started in a virgin state, i.e. no flux had penetrated.

5.6.4 Reduced critical current and power-law exponent

As previously mentioned, the critical current I_c and the power exponent n of the layers are not constant parameters, but depend on the presence of the magnetic field acting on the tapes. Therefore, the equivalent circuit model has been refined by using a different critical current for each layer.

The model of the hysteretic inductances (5.13)- (5.15) requires a constant critical current I_c, so that, in order to take into account the effect of the field dependence, the average magnetic field acting on the layers has been computed by means of 2D FEM simulations, as already described in section 5.4.1; in particular, the average field for computing the reduction of the critical current, has been evaluated according to Eq. 5.10.

FEM simulations compute the instantaneous value of the magnetic field at each node of the meshed geometry, but for the macroscopic equivalent circuit model, an average effect is needed. Firstly, for each simulated time step, the average value of the magnetic field acting on the tapes of each layer has been computed by FEM as the spatial integral of the magnetic field on the superconducting cross-section. Secondly, the reduction of I_c and n has been calculated, according to Eqs. 4.10 and 4.11. Finally, their average value during one cycle has been computed and used as input data for performing new simulations with the equivalent circuit model. Using $I_c(0) = 1200\ A$ and n(0)=21 for all the layers, the effective critical currents $I_{c,k}$ and power-law

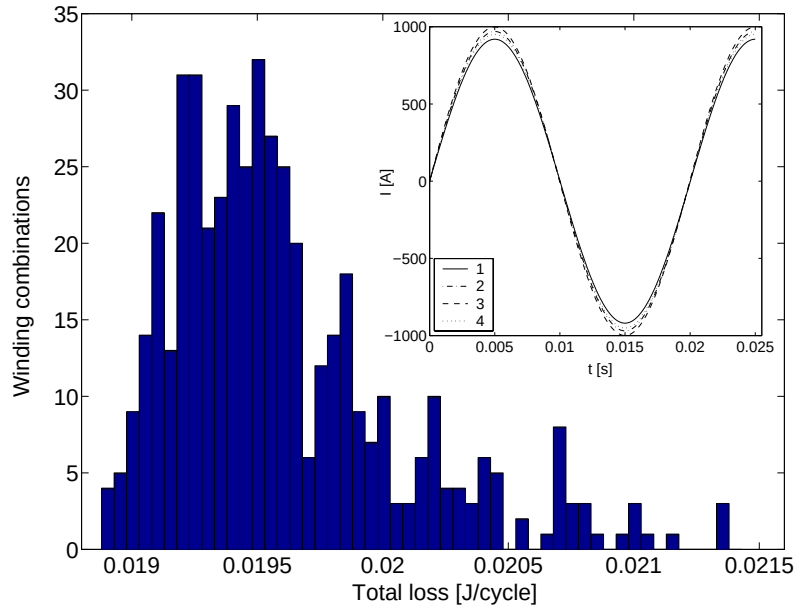

Figure 5.27: Histogram over the number of winding angle combinations that give the same total loss in the sample cable for the 480 combinations of winding angles of step 3. The increase of the total loss lies between 10% and 15% for the considered winding angles in a vicinity of the optimum. The inset depicts the currents in the four layer using the optimal winding angles 25°, 10°, −13° and −36°.

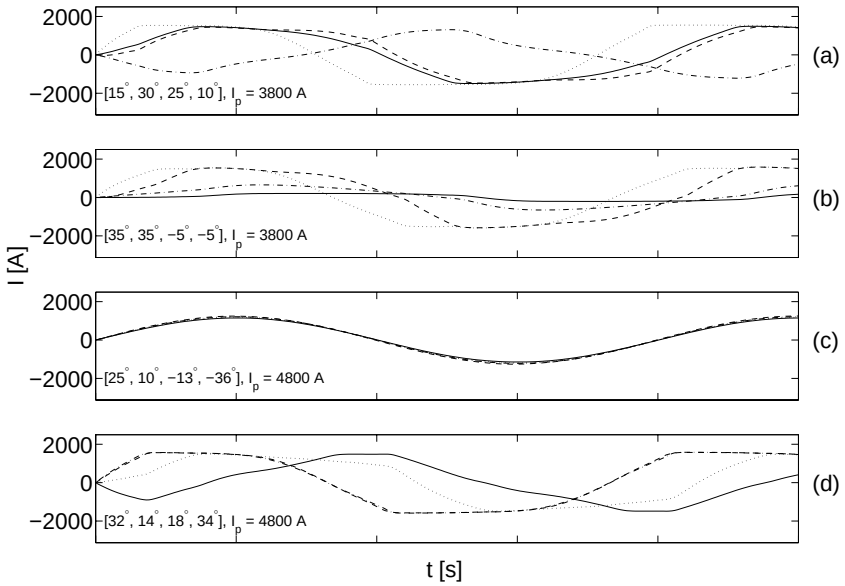

Figure 5.28: Current repartition among layers 1 (solid), 2 (dot-dashed), 3 (dashed) and 4 (dotted). Graphs (a)–(b) are with two bad choices of winding orientations and angles at $I_p = 3800$ A, graphs (c)–(d) with the optimal and a bad choice of angles at $I_p = I_{c,tot} = 4800$ A.

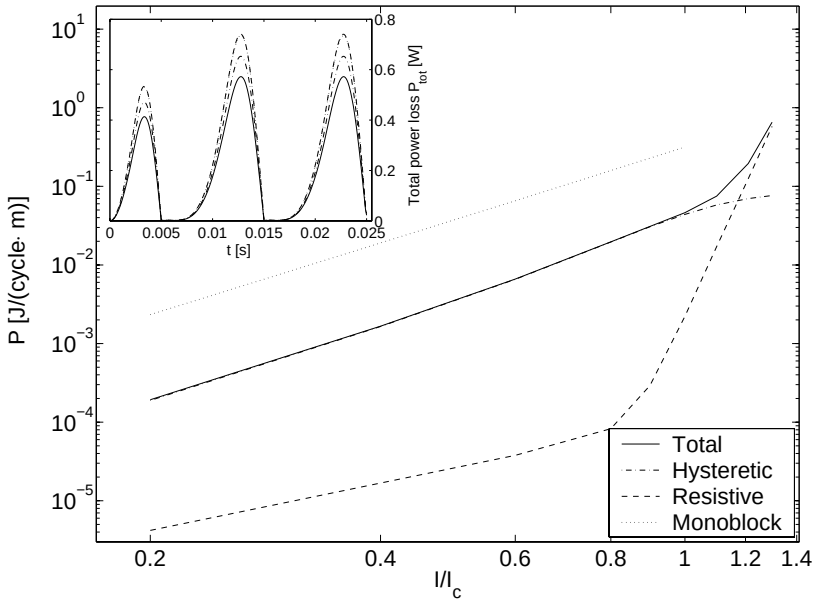

Figure 5.29: Losses in the optimized cable. Inset: the power losses in layer 1 (solid), 2 (dot-dashed), 3 (dashed) and 4 (dotted) during the simulation at $I_p = 3800\ A$. Layer 3 and 4 produce the largest losses (almost equal).

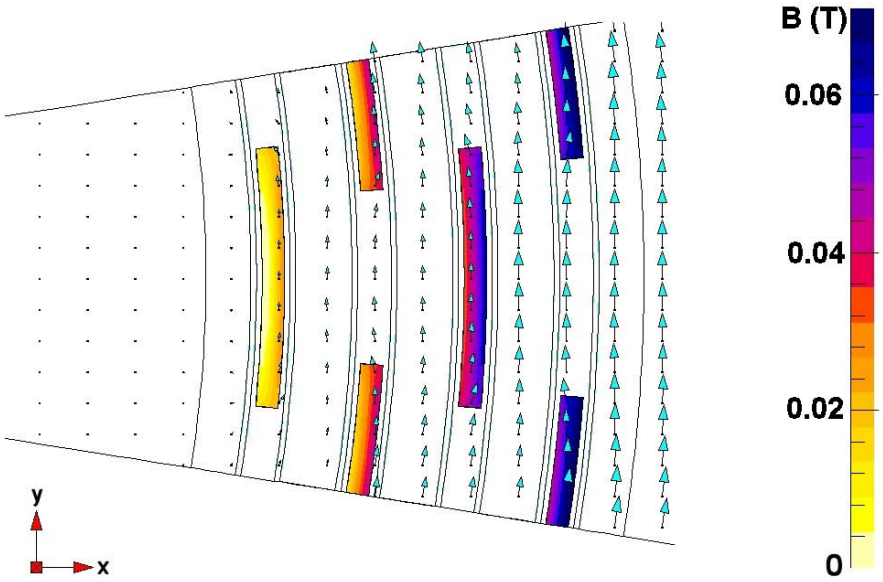

Figure 5.30: Magnetic field map for a transport current of 3800 A equally shared by the four layers, obtained by FEM simulations. The field is evaluated at the peak value of the transport current. Only an angular sector (1/20) of the cable cross-section is shown.

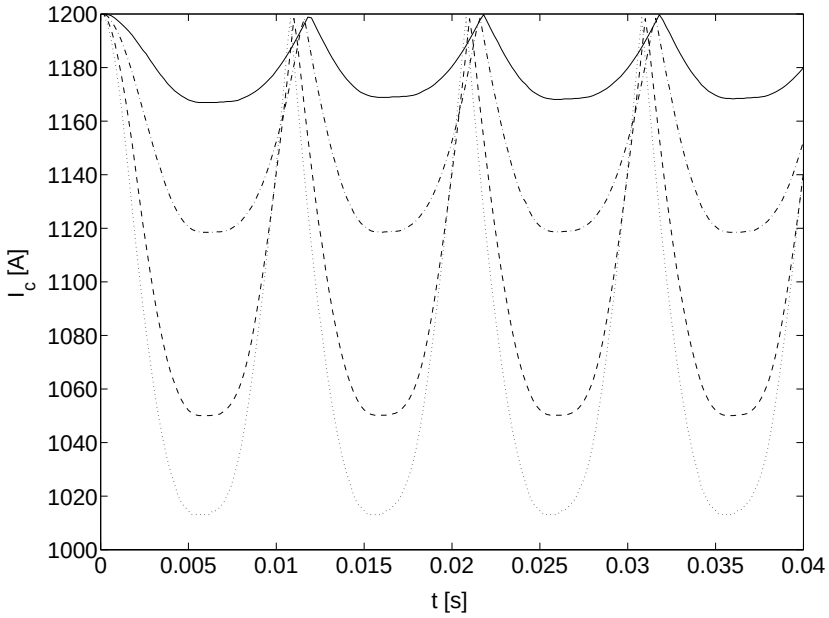

Figure 5.31: Evolution of critical current I_c during two cycles in each of the cable layers 1 (solid), 2 (dash-dotted), 3 (dashed) and 4 (dotted).

exponents n_k for the four layers $k = 1, \ldots, 4$ result to be 1178 A, 1143 A, 1095 A, 1071 A and 20.6, 19.9, 19.0, 18.5, respectively.

Figure 5.30 displays the map of the magnetic field in the superconducting tapes, for a transport current of 3800 A equally shared by the four layers, obtained by FEM simulations. Figure 5.31 depicts the temporal evolution of the reduced critical currents. The effect of the reduced critical currents $I_{c,k}$ and power-law exponents n_k on the optimal winding angles has been investigated. The current repartition is mainly determined by the inductances computed by Eqs. 5.1-5.2, as they dominate the voltage due to the resistances (5.11), below $I_{c,k}$. This means that step 1 (no hysteretic inductances) can be omitted, since the B-dependence for the superconductor only influences the resistances. Therefore, it suffices to examine step 2 and 3, for which it turns out that the same combinations of angles had to be investigated as in the previous section. (See Table 5.7.) The minimal total loss is so obtained with the winding angles 25, 10, -14 and -37 for the four layers, respectively, which produce a total loss of 21.52 $mJ/cycle$ (about 13% more than with equal I_c and n for all layers).

The winding angles of the optimal configuration with reduced critical currents result to be very close to the optimal configuration with equal I_c in all layers, c.f. previous section. As mentioned, the current distribution is mostly determined by the linear inductances. Nevertheless, since a transport current close to I_c is considered, the resistive term can have a slight influence on how the current is partitioned across the layers. This influence is expected to be more prominent as the considered currents are closer to I_c. Finally, the *optimal* configuration is affected by the reduced critical currents through *both* the resistive loss (prominent close to I_c) as well as the hysteretic loss (below I_c). Fig. 5.32 shows the current distribution across the layers and the corresponding power losses for the optimal winding combination.

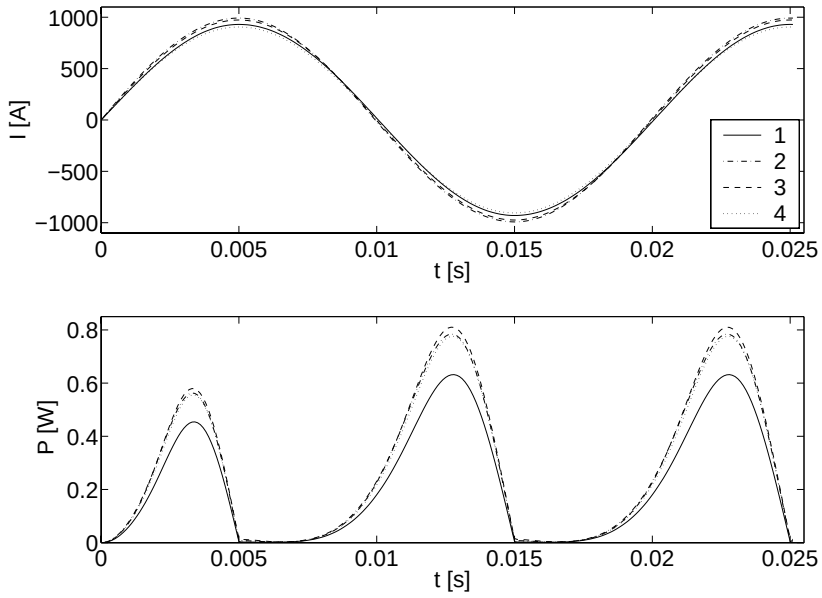

Figure 5.32: Current distribution across the four layers, and the corresponding power losses for the optimal winding angles, using reduced critical current and power-law exponent. Layer 1 (solid), 2 (dot-dashed), 3 (dashed) and 4 (dotted).

5.6.5 Applied voltage source

In the preceding optimization, a current source has been applied in the simulations. In a real situation, it is rather a voltage source that produces the transport current. The equivalent circuit model allows for the employment of a voltage source. In order to have a current corresponding to approximately 80% of the total critical current, a sinusoidal voltage source of peak value 0.18 V has been used in a separate simulation of the optimized cable from section 5.6.4. The resulting current distribution across the layers is close to uniform thanks to the optimized winding angles, and no practical difference can be noted from the results in Fig. 5.32.

5.7 BIG-POWA power-link

This thesis work has been almost entirely performed within the framework of the European Project BIG-POWA: "High current Bi-2223 conductors with innovative wire geometry for power applications". The project, which involved many European academic and industrial partners, was funded by the European Community under the Competitive and Sustainable Growth Programme (1998-2002); it started on March 1, 2000 and finished on May 31, 2003. One of its goals was the manufacturing of a two-layer power-link sample, realized with special low-loss Bi-2223 multi-filamentary tapes. The tapes have been produced by Nordic Superconductor Technology (Denmark).

The tasks of EPFL were mainly about numerical modelling of superconducting tapes and cables; nevertheless, I helped Mr. Sergio Spreafico (Pirelli Labs, Milan, Italy) in the manufacturing of the power-link, which has been performed at the Pirelli laboratories in Livorno Ferraris, Vercelli, Italy. This section provides a description of the assembling process, which is valid for the production of long-length HTS cables, too, and the results of the AC loss characterization of the cable (made by Pirelli).

Tape	Type A	Type B
I_c @ 77 K $[A]$	44	42
Length $[m]$	58.5	21.7
Width $[mm]$	3.554	3.912
Thickness $[mm]$	0.255	0.253
Twist pitch $[mm]$	15	15

Table 5.8: Properties of Bi-2223/Ag tapes provided by NST.

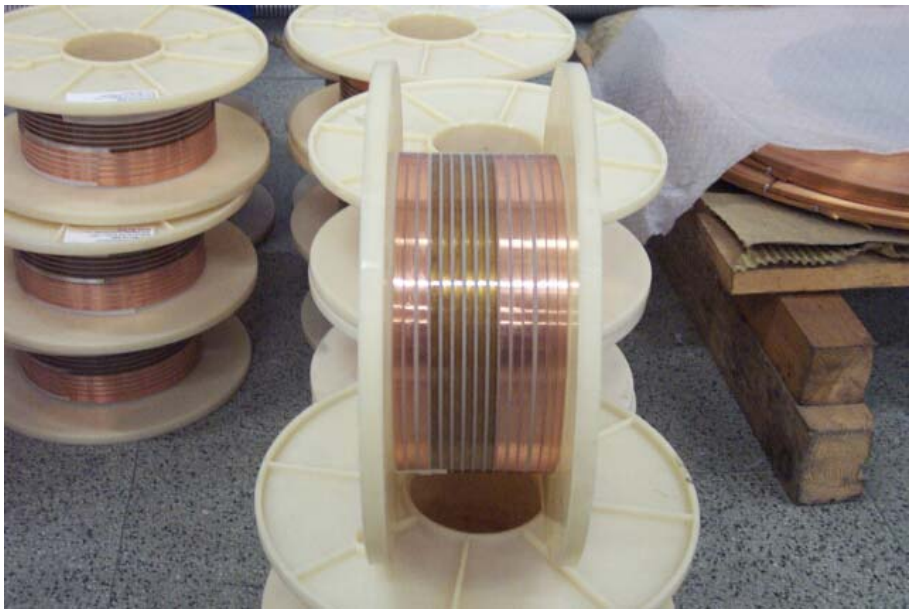

Figure 5.33: View of the plastic reels the tapes are wrapped on, before the deposition on the former. The superconducting tape is wrapped in the central part of the reel (dark colour). The copper tape used for pulling the superconducting tape can be distinguished in the left and right part of the reel (light colour).

NST provided two types of Bi-2223 twisted tapes, whose properties are listed in Table 5.8. In order to protect the tapes from liquid nitrogen diffusion inside the Bi-2223 structure, a thin layer of plastic varnish was applied. In fact, the diffusivity phenomenon can cause important damages during tape warming-up. The tapes have been received from NST on two reels and they have been cut into pieces 1.60 m long. Few meters of thin copper tape (3.5 $mm \times 0.3$ mm) have been soldered at the two ends of each piece for pulling the superconducting tape during the deposition on the former. For manufacturing the power link, an industrial machine has been used, which needs the tapes wrapped on special reels, see Fig. 5.33. The passage from the two original reels to the ones to be used for wrapping the tapes around the former has been done by means of a special equipment, which works at constant load. The tape path consisted in few direct bending steps on 100 mm pulleys and one reverse bending step on a 200 mm pulley. Unfortunately, this operation has sensibly damaged the tapes. The initial critical current of 42-44 A dropped at about 33-34 A, with a reduction of about 25 %. This has been a significant damage not only in terms of absolute transport capacity, but also because it could have had an impact on the coupling between the Bi-2223 filaments. The former consisted of an aluminum tubular spiral 1 mm thick wrapped with a copper braid. In order to obtain a smooth cylindrical surface for the deposition of the tapes, a layer of bedding material has been utilized. The first

Figure 5.34: First deposited layer of superconducting tapes.

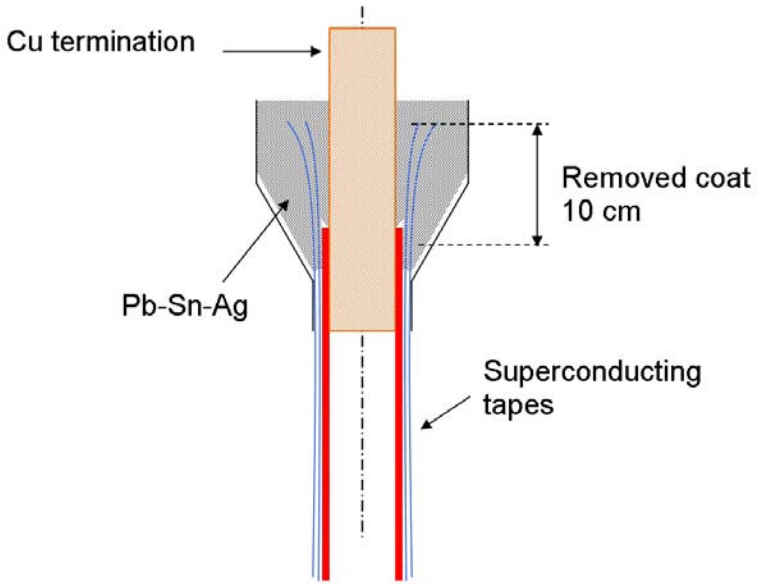

Figure 5.35: Sketch of the cable termination.

and second layer, each of them composed by 15 tapes, have been deposited with a pitch angle of 20.3° and 20.8°, respectively, see Fig. 5.34. In order to electrically insulate the two layers, a layer of bedding material has been wrapped between them. More type A tape than B has been received, see Table 5.8. Since the two tapes have slightly different dimensions (type B is wider), in order to have a configuration as uniform as possible, in each layer the 15 tapes have been arranged as follows: BAA-BAA-BAA-BAA-BAA. The two ends of the cable sample have been connected to copper terminations. The external varnish layer has been removed from the last 10 *cm* of the tapes. The cable termination is sketched in Fig. 5.35, whereas the view of the real sample is given in Fig. 5.36. The connection between the copper cylinder and the tapes has been made with a low-melting point Pb-Sn-Ag alloy, which is permeable to the liquid nitrogen. The contact resistance between the cable termination and the HTS tapes has been estimated between 1 $\mu\Omega$ and 20 $\mu\Omega$.

The DC critical current has been measured with the standard four-point contact method. The voltage taps have been positioned near the two end terminations. The measured $E - I$ curve is reported in Fig. 5.37: the cable has a critical current of about 1050 A and a n-value of about 10. This corresponds to an average critical current of 35 A per tape and gives an indirect confirmation of the damage occurred to the tapes, when they have been moved from the original

Figure 5.36: View of the head of the cable sample.

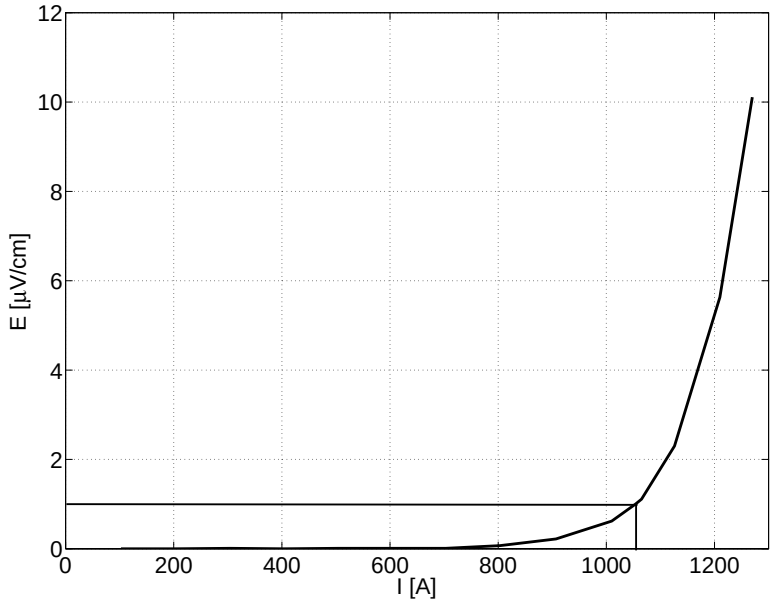

Figure 5.37: DC characterization of the power-link, made by Pirelli: $I_c \simeq 1050\ A$, $n \simeq 10$.

NST reels to the plastic ones.

The self-field AC losses have been measured for different values of the (sinusoidal) transport current. The voltage taps have been positioned at a distance of 80 cm. A lock-in amplifier has been used to analyze the voltage at fixed current; the circuit has been equipped with a variable compensator, in order to reduce the inductive component of the voltage signal. The

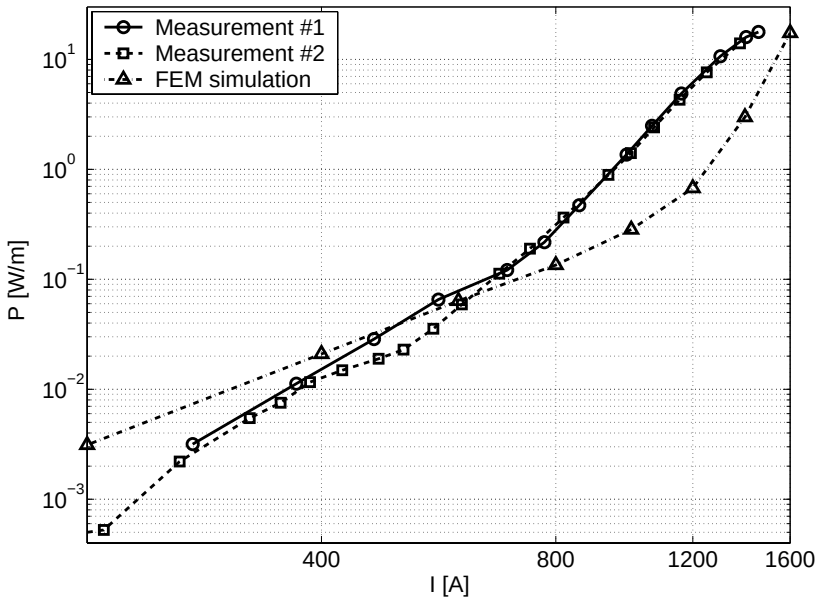

Figure 5.38: AC losses as a function of the transport current in the BIG-POWA power-link. Displayed are the measured values and the results of FEM simulations.

measurements have been done in an open liquid nitrogen bath at atmospheric pressure.

Due to the use of tapes with twisted filaments, the AC losses of the power-link were expected to be quite low, especially in the low current regime.

For evaluating the effect of such twisting, the measured AC losses have been compared with the ones predicted by 2D FEM computations, which consider straight filaments. For sake of simplicity, the real sample (composed by tapes with twisted filaments) is referred to as *twisted conductor* and the simulated cable as *straight conductor*. Figure 5.38 shows the measured AC losses and the results of FEM simulations as a function of the applied transport current. The losses have been measured twice and the results of both tests are reported. In the low current regime, the decoupling effect reduces the losses of the twisted conductor with respect to the straight one. By increasing the current, the filaments start coupling and the AC losses of two conductors become closer until the two curves cross at about 600 A. At higher current, the AC losses of the twisted conductor become higher. This can be explained by the magnetic coupling of twisted filaments in the tapes. Furthermore, the filament decoupling was probably influenced by the damaging occurred during the spooling of HTS tapes. At high transport currents, part of the current can flow in the silver matrix instead of following the twisted path of the filaments, causing dissipation. In any case, the figure shows the capacity of reducing the AC losses by filament twisting in the low current regime. In order to increase the efficiency of this method, it is needed to work on better filaments decoupling, which can be obtained by using a shorter twist pitch and/or a higher matrix resistance.

5.8 Original contributions of this thesis

- Development of a simple electrical model of multi-layer HTS cables for finding the geometrical configurations giving a uniform repartition of the current among the layers.

- Extension of 2D FEM calculations from tapes to cables for evaluating the effects of the

magnetic self-field on the transport capacity of HTS cables and for computing the AC losses.

- Study of the influence of the non-uniformity of the parameters of the individual tapes (contact resistance, I_c, n) on the global performance of a single-layer cable.
- Use of an equivalent circuit model of multi-layer HTS cables for a quicker evaluation of the AC losses without computing the current and field distributions inside conductors.
- Assembling of the BIG-POWA power-link in collaboration with Pirelli.

Chapter 6

3D modelling of the coupling effect

This chapter is dedicated to 3D modelling of the coupling effect between filaments via the resistive matrix, induced by an external varying magnetic field. When a varying magnetic field is acting on multi-filamentary superconductors, it can couple the filaments into a larger unique magnetic object giving rise to higher power losses. Theoretical predictions of this effect only exist for the quite peculiar case of fully penetrated infinite slabs, a configuration often very far from the real geometry. Since the magnetic field and the current profiles drastically depend on the shape of the filaments, it is interesting to study this phenomenon for geometries involving finite dimensions and for magnetic fields only partially penetrating the superconducting filaments.

At the beginning of this chapter, the coupling effect is qualitatively explained and a summary of the existing theory is given. Therefore, the results obtained by 3D FEM simulations are discussed in detail. Three very different geometries have been analyzed: the slab, the square and the strip. The results for the corresponding field profiles and AC losses are given. A criterion for quantitatively determining the coupling field is also discussed.

6.1 Introduction

The coupling effect between filaments can be easily explained by referring to Fig. 6.1, which displays two superconducting filaments of finite length separated by a silver matrix and subjected to a varying magnetic field. At low field rates, the magnetic field induces current loops in each filament, as displayed in Fig. 6.1a. Reported on the bottom of the figure is the magnetic field profile inside the filaments. In this situation the filaments behave as two separated identical objects. For a sufficiently high field rate, the induced voltage is sufficient to overcome the resistive drop across the matrix: the loop is closed through the silver matrix and the current flows in opposite direction in each filament, see Fig. 6.1b. The filaments are now coupled into a larger magnetic object, as can be derived from the corresponding field profile on the bottom of Fig. 6.1b, and a coupling current flows through the silver. Since the resistivity of the silver is much higher (2-3 orders of magnitude) than superconductor's one, the coupling current in the silver gives an important contribution to the total losses. The coupling effect depends in general on several parameters: the field variation rate, the resistivity of the matrix material, the size of the filaments, the critical current density and the length of the superconductor. A theoretical quantitative description can be drawn in the case of fully penetrated infinite slab filaments [68], as follows.

Considered is a sandwich of normal conductor between two slabs of superconductor, as shown in Fig. 6.2. When a varying field is imposed parallel to the broad faces of the slabs (z-direction), coupling currents are induced as shown, screening as much of the sandwich as possible from the varying field. The changing rate is indicated as $\dot{B}$ and it is assumed that $\dot{B}$ is the same everywhere. Let the total current (per unit of distance in the z-direction) in one of the

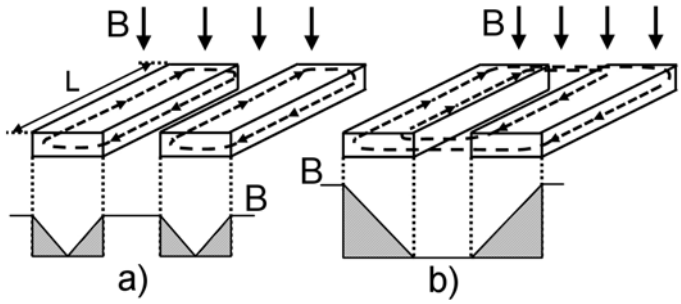

Figure 6.1: Sketch of two superconducting filaments subjected to a varying magnetic field, in the uncoupled (a) and coupled (b) case. The profile of the magnetic field penetration is shown on the bottom of each figure.

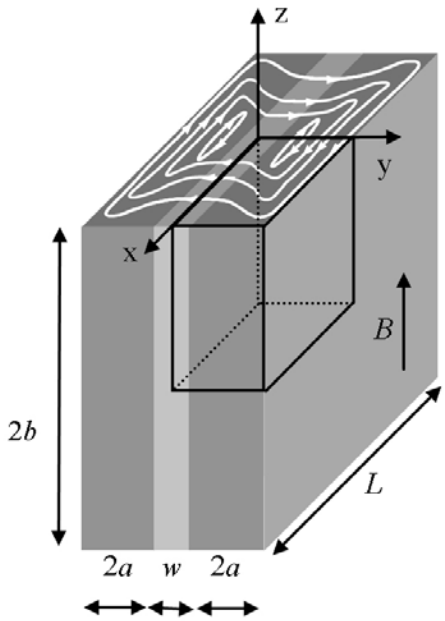

Figure 6.2: Coupling currents induced in a sandwich of superconductor and normal metal by a changing magnetic field.

superconducting slabs at distance x from the centre of the slab be $I(x)$. The amount of current crossing over the silver matrix between x and $x+\delta x$ is indicated with δI. This current is driven by the voltage $\dot{B}wx$, where w is the silver thickness, as indicated in Fig. 6.2. Therefore, one has

$$\delta I(x) = \dot{B}wx/\rho w. \tag{6.1}$$

Solving this differential equation with the boundary condition $I(L/2) = 0$ gives

$$I(x) = \dot{B}(L^2/4 - x^2)/2\rho. \tag{6.2}$$

The maximum of the current is in the centre ($x = 0$); it will fill all the cross-section of the slab when $I(0) = 2aJ_c$, i.e. when the sample has a critical length

$$L_c = 4(a\rho J_c/\dot{B})^{1/2}. \tag{6.3}$$

For a given length L, this relation can be inverted to find the critical value of the magnetic field rate, the *coupling field rate*

$$\dot{B}_c = 16(a\rho J_c/L^2). \tag{6.4}$$

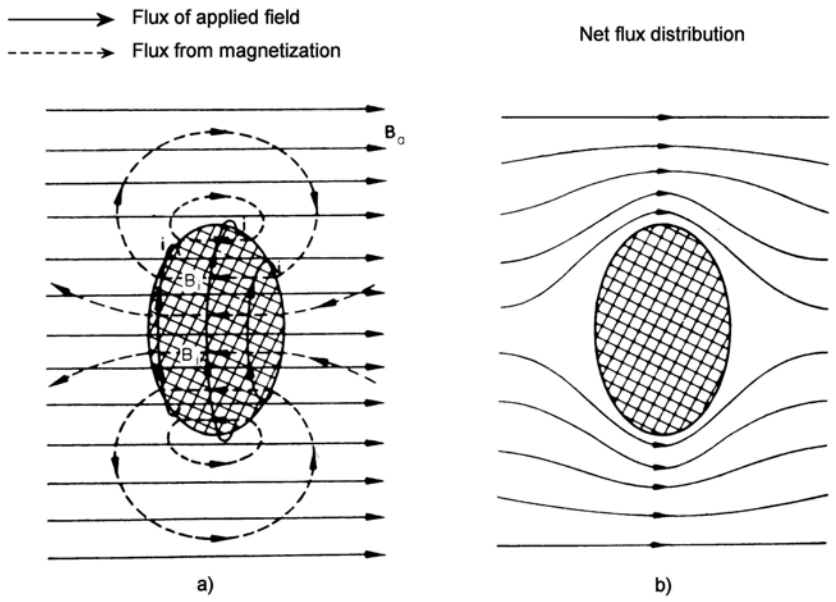

Figure 6.3: Magnetic flux around a superconducting sphere. In a) the flux of the applied field and the one from magnetization of the sphere are shown separately. In b) the resulting net flux is displayed.

6.2 The demagnetizing effect

The analysis carried out so far refers to the case of a slab geometry, where the dimension parallel to the direction of the applied field is considered infinite. When this is not the case, the field profiles at the interface between superconductor and normal regions change drastically, resulting in a magnetic field that can be locally larger than the applied one. This section contains a brief description of what happens when specimens of arbitrary shape are considered. This will be useful to understand the results obtained by FEM simulations in the case of squares and strips, which will be shown later. Considered is the case of a superconducting sphere placed in a uniform magnetic field $\mathbf{H}_a$. If the field is not large enough, the flux lines are excluded from the interior of the sphere[1] by the diamagnetic screening currents, as displayed in Fig. 6.3[2]. In order to evaluate the magnetic field strength inside the sphere (H_i), one can suppose that the field $\mathbf{H}_a$ is produced by a solenoid, as shown in Fig. 6.4. The line-integral of the magnetic field vector $\mathbf{H}$ around any closed path is equal to the number of current-turns linking the path. Applying this property to the closed path ABCDEF shown in Fig. 6.4 gives

$$\oint \mathbf{H} \cdot d\mathbf{l} = NI, \tag{6.5}$$

where N is the total number of turns in the solenoid and I is the current through each of them. The line-integral can be separated into two parts:

$$\oint \mathbf{H} \cdot d\mathbf{l} = \int_{AB} \mathbf{H}_i \cdot d\mathbf{l} + \int_{BCDEFA} \mathbf{H}_e \cdot d\mathbf{l}, \tag{6.6}$$

[1] For simplicity, type-I superconductors are considered.
[2] Figures 6.3 and 6.4 have been taken from [4].

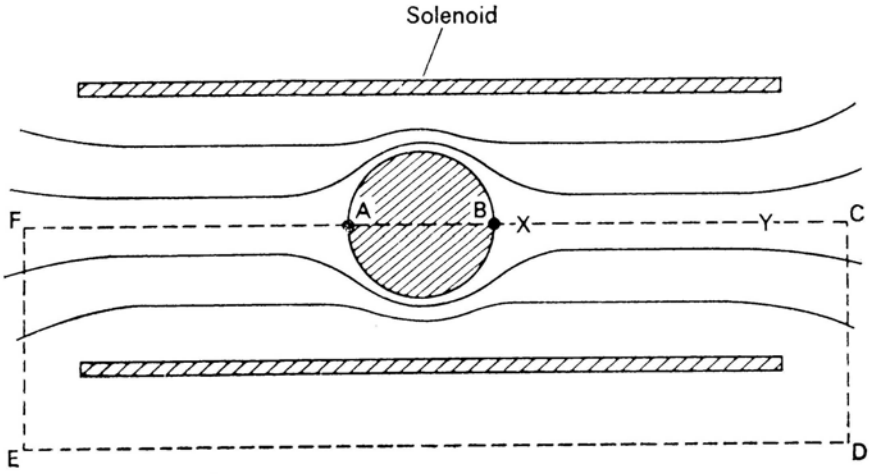

Figure 6.4: Superconducting sphere in a uniform magnetic field generated by a solenoid.

where $\mathbf{H}_i$ is the field within the sphere and $\mathbf{H}_e$ the field at any point outside. Now, if the sphere is removed, the line integral is still equal to NI and one can write

$$\oint \mathbf{H} \cdot d\mathbf{l} = \int_{AB} \mathbf{H}_a \cdot d\mathbf{l} + \int_{BCDEFA} \mathbf{H}'_e \cdot d\mathbf{l}, \tag{6.7}$$

where the field between A and B in the absence of the sphere is $\mathbf{H}_a$, whereas $\mathbf{H}'_e$ is the field at any point outside AB when the sphere is removed. Therefore one has:

$$\int_{AB} \mathbf{H}_i \cdot d\mathbf{l} + \int_{BCDEFA} \mathbf{H}_e \cdot d\mathbf{l} = \int_{AB} \mathbf{H}_a \cdot d\mathbf{l} + \int_{BCDEFA} \mathbf{H}'_e \cdot d\mathbf{l}. \tag{6.8}$$

If H_e and H'_e are compared at a point on the axis of the solenoid such as X in Fig. 6.4, H_e is clearly less than H'_e, because the effect of the screening currents extends outside the sphere and distorts the flux lines (see Fig. 6.3 for comparison). On the other hand, at points far from the sphere, such as Y, the presence of the sphere has a negligible effect and $H_e = H'_e$. Hence everywhere $H_e \leq H'_e$ and it follows from Eq. 6.8 that H_i must be greater than H_a, i.e. the magnetic field strength inside the sphere exceeds the applied field H_a.

This is a special case of a well known problem in magnetostatics. Because historically the study of magnetism preceded that of superconductivity, the phenomenon is referred to as *demagnetization*. A magnetized body is said to produce within itself a *demagnetizing field* $\mathbf{H}_D$, which is superimposed on the applied field. The field $\mathbf{H}_i$ inside the body can be therefore written as $\mathbf{H}_i = \mathbf{H}_a - \mathbf{H}_D$.

For bodies of general shape the situation is complicated because the demagnetization is not uniform, the internal field varying in strength and direction throughout the body. For the special case of ellipsoids, with the internal field uniform throughout the body and parallel to the applied field, the internal field can be written as $\mathbf{H}_i = \mathbf{H}_a - N\mathbf{I}$, where $\mathbf{I}$ is the magnetization and N is the *demagnetizing factor*.

The demagnetizing factor in general depends on the shape of the body. Its value in the case of simple geometries is given in Table 6.1. The corresponding shape factors (defined by $(1 - N)^{-1}$) are listed as well. The aspect ratio is defined as width/thickness.

Geometry	Aspect ratio	Demagnetizing factor N	Shape factor $(1-N)^{-1}$
Slab	a/b $(a \ll b)$	≈ 0	≈ 1
Square	1	$\approx 1/2$	≈ 2
Round	1	$1/2$	2
Strip	a/b $(a \gg b)$	$1 - b/a$	a/b

Table 6.1: Demagnetizing and shape factors for different geometries.

6.3 The model, the geometry, the mesh and the solving process

For studying electrical conductors in externally applied magnetic field by FEM technique, the $\mathbf{T}-\Phi$ formulation has been used, see chapter 3. For the simulations a simple geometry consisting of two superconducting filaments divided by a silver matrix has been considered, as displayed in Fig. 6.2. The magnetic field is applied along the z-axis, which induces current loops in the xy plane.

The width $2a$ of the superconducting filaments has been set equal to 0.3 mm. The width w of the silver matrix and the length of the conductors L, when not differently specified, have been set equal to 0.2 mm and 2 mm, respectively. Three different geometries have been considered: the slab ($2b = 6$ mm), the square ($2b = 0.3$ mm) and the strip ($2b = 0.03$ mm), which have an aspect ratio (a/b) of 0.05, 1 and 10, respectively. In order to reduce the size of the problem and the computation time, only one eighth of the full geometry has been simulated. The appropriate symmetry conditions have been applied on the three symmetry planes: normal magnetic field on the xy plane, tangential magnetic field on the xz and yz planes. Throughout this chapter all the figures refer to the reduced geometry.

Particular attention has been paid to the mesh of the geometry. It has to be quite fine in order to have sufficiently detailed results, yet keeping the size of the problem and the computation time to a reasonable scale. The conducting regions (superconducting filaments and silver matrix) and the surrounding air volumes have been meshed with a fine mapped mesh, i.e. consisting of regular parallelepiped elements. The rest of the air domain has been meshed automatically (tetrahedral elements), because it does not involve regions where it is important to know precisely the magnetic field distribution. Since the most rapid variation of the electromagnetic state variables takes place at the interface between the different regions (superconductor-silver and superconductor-air), the density of the mesh points has been mostly concentrated there by means of a logarithmic mesh. Figure 6.5 displays an example of the mesh for the square geometry. The computation time depends on many factors: the number of nodes (the slab geometry has about 25,000 nodes, the square about 22,000, the strip about 7,500), the amplitude and the frequency of the applied field (simulations are slower for large and low-frequency fields). It depends also on the number of consecutive time steps, which have to be quite numerous for avoiding convergence problems: in most cases the peak value of the applied magnetic field ($\omega t = \pi/2$, one quarter of the cycle) is reached with 100 time steps. Generally speaking, on a computer equipped with a 2 GHz processor, the simulation of half a cycle lasts between 4 and 48 hours.

6.4 The computed quantities

For this investigation, the behaviour of a virgin sample under the action of an externally applied sinusoidal magnetic field has been studied. The amplitude of the field has been varied in order to take into account two different situations, i.e. fully and partially penetrated superconductors.

Simulated is half a cycle, since the points of main interest are two: $\omega t = \pi/2$, when the applied magnetic field reaches its peak value, and $\omega t = \pi$, when the externally applied field

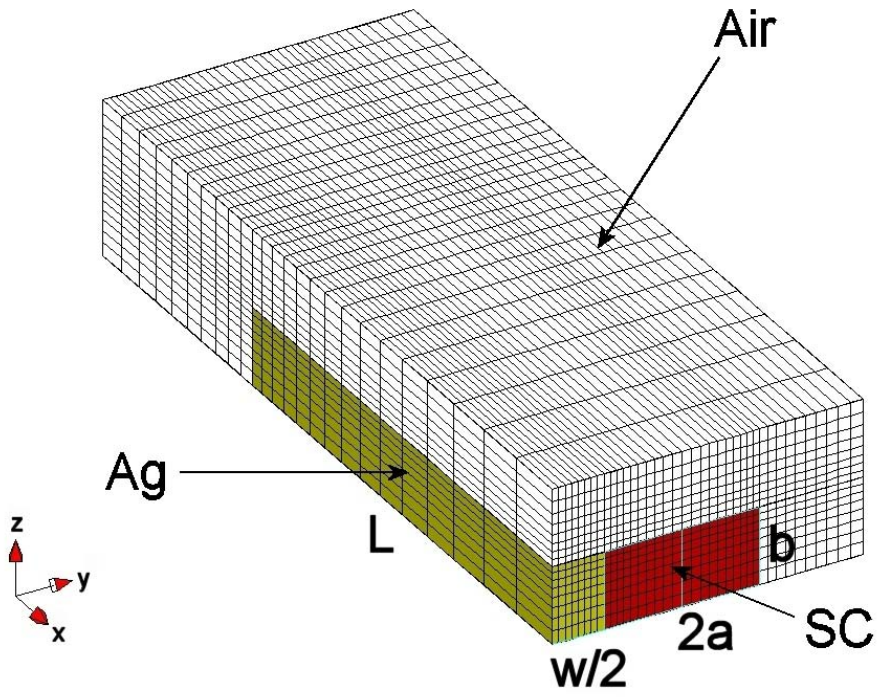

Figure 6.5: Reduced (1/8) meshed geometry used for simulations for an aspect ratio equal to 1 (square). The superconducting filament is rectangular due to the symmetry with respect to xy plane.

becomes zero again.

The following quantities have been analyzed (see Fig. 6.2 as reference):

- The magnetic field profiles along the positive part of the y-axis.
- The coupling current flowing from one superconducting filament to the other through the xz plane in the silver.
- The AC losses in the silver volume due to the coupling current.

The first quantity allows determining the degree of penetration of the magnetic field inside the filaments and if they are coupled or not. The other two, after having been normalized by the aspect ratio, give a more quantitative estimation of the coupling for comparison among the different geometries. In particular, the coupling current is given by the integral of J_y on the xz plane, whereas the AC losses are computed as follows:

$$P = \frac{1}{T} \int_T \int_V \mathbf{J} \cdot \mathbf{E} \, dV dt, \tag{6.9}$$

where T is the time interval of the simulation (half a cycle), V is the silver volume.

An example of the typical current density distribution both for the uncoupled and coupled case is given in Fig. 6.6, which refers to the square geometry, already shown in Fig. 6.5. The arrows represent the direction of the current density and their size is proportional to the value. When the filaments are uncoupled (a), each filament carries its own "go-and-return" current and no current flows in the silver matrix. According to the scale, the dark colour in the silver means that no current is flowing there. On the other hand, when they are coupled (b), the current

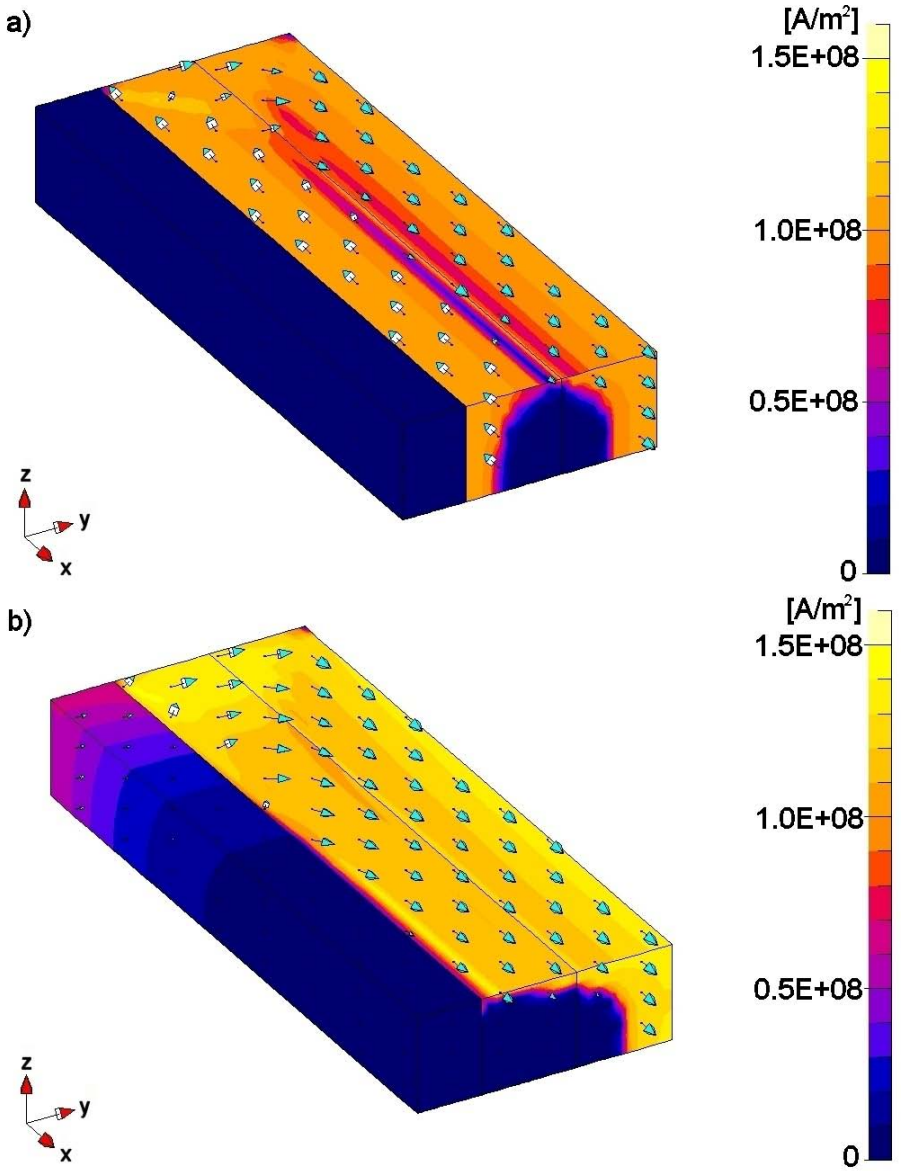

Figure 6.6: Current density distribution in the square geometry for the uncoupled (a) and coupled case (b). The pictures refer to an applied field of 5 mT at 100 Hz (a) and 10 kHz (b), respectively.

crosses the silver matrix near the end and closes the loop flowing in the adjacent filament, which is not displayed due to the imposed symmetry. As clearly visible, in this case the current in the superconducting filament flows in only one direction.

6.5 The influence of the aspect ratio on the magnetic field profiles

Figure 6.7 shows the profiles of the magnetic field along the positive part of the y-axis for the slab at different frequencies for an external magnetic field of 35 mT (a) and 5 mT (b), computed by FEM simulations. In this plot and in the next similar ones, the silver region corresponds to the

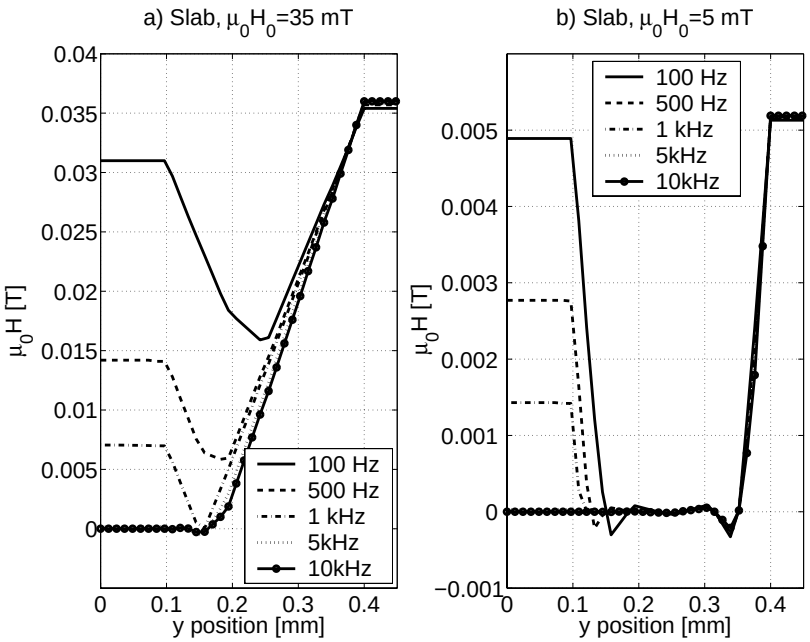

Figure 6.7: Magnetic field profile along the positive y-axis for the slab, $\mu_0 H_0 = 35\ mT$ (a) and $\mu_0 H_0 = 5\ mT$ (b).

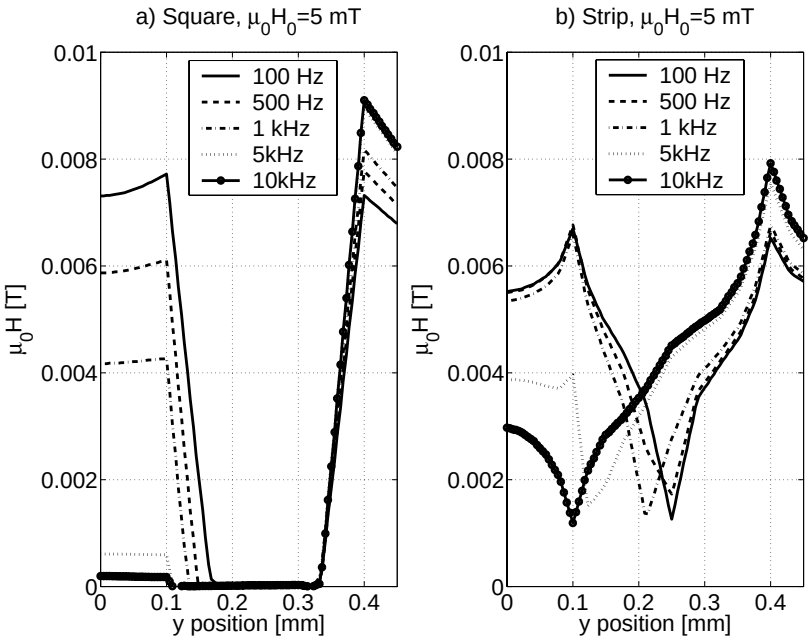

Figure 6.8: Magnetic field profile along the positive y-axis for the square (a) and the strip (b) geometry, $\mu_0 H_0 = 5\ mT$.

points with $0\ mm < y < 0.1\ mm$, the superconductor to the points with $0.1\ mm < y < 0.4\ mm$, the air to the points with $y > 0.4\ mm$.

Both plots clearly show the passage from an almost completely uncoupled ($100\ Hz$) to a complete coupled ($10\ kHz$) situation. In the first case (a) the field fully penetrates the

superconductor, whereas in the second one (b) the internal part of the filament is not reached by the magnetic field.

According to the critical state model, the field profile allows an indirect evaluation of the critical current density of the superconductor by looking at the slope of the magnetic field penetrating the superconductor from the air interface. For this configuration the general relation $\nabla \times \mathbf{H} = \mathbf{J}$ can be written as $J_x = \partial H_z/\partial y \cong \Delta H_z/\Delta y$, where ΔH_z is the amplitude of the field at the superconductor-air interface and Δy is the distance between this interface and the point where the field becomes zero. In Fig. 6.7a for $f = 1\ kHz$, one has $\Delta H_z = H_0 = 2.8 \cdot 10^4\ A/m$ and $\Delta y = 0.24\ mm$, which gives $J_c = 1.16 \cdot 10^8\ A/m^2$, which is not very far from the imposed value of $10^8\ A/m^2$. This is a confirmation of the fact that the quantities are correctly calculated by the FEM software. Moreover, the numerical differences with respect to the CSM are also due to the finite-exponent power-law ($n = 21$), which only approximates the CSM ($n = \infty$).

In both figures 6.7a and 6.7b the magnetic field in the air region immediately outside the superconductor is equal to the external applied field. This is a peculiarity of the slab geometry, whereas it is not the case for the square and even more for the strip geometry. This is visible in Fig. 6.8, which shows the same kind of profile for the square and strip geometry, for an external field of 5 mT. In the case of the square (a) the demagnetizing effect, due to the finite thickness of the conductors, causes the field at the superconductor-air interface to be higher than the applied one, reaching a value between 7 mT and 9 mT, increasing with the frequency. This increasing value is due to the fact that at high frequencies (for example 10 kHz) the square filaments are fully coupled and the entire geometry has an aspect ratio $(4a + w)/2b = 0.8\ mm/0.3\ mm \cong 2.7$ instead of two separate squares with aspect ratio 1; and the higher the aspect ratio, the higher the demagnetizing effect.

In the case of the strip the demagnetizing effect is even more evident and the strip is so thin that the field of 5 mT is high enough to fully penetrate the filaments. Also with this geometry the field at the superconductor-air interface is increasing with the frequency due to the increase of the aspect ratio caused by the coupling between the filaments. In this case the aspect ratio increases from 10 to $0.8\ mm/0.03\ mm \cong 27$.

Figures 6.9-6.11 depict the three-dimensional profiles of the magnetic field for the slab, square and strip geometry, respectively, for a magnetic field of 5 mT at 100 Hz.

6.6 The coupling current and the AC losses

The shape of the filaments strongly influences the time evolution of the coupling current and the rapidity of saturation. Figure 6.12 displays the case of a sinusoidal field of 350 mT at 50 Hz, which corresponds to a full penetration for all the three geometries. In order to compare the results, the coupling current has been normalized by the aspect ratio. Displayed is the first half cycle (a) with a detailed view of the initial stage (see inset) on a log-log scale. First of all one can see that the current evolution is almost cosinusoidal, since the driving voltage is proportional to the time derivative of the magnetic flux in the filaments, according to Faraday's law $\nabla \times \mathbf{E} = -\partial \mathbf{B}/\partial t$. The coupling current increases sharply to saturation at the beginning, when the variation rate dB/dt is maximum. The initial rising speed for the coupling current varies significantly according to the shape factor η of the superconductor: $\eta = 1$ for slabs, $\eta = 2$ for squares, $\eta = a/b$ for strips [69]. In order to make a quantitative comparison, the time when the coupling current reaches 2 A has been chosen: it corresponds to the time when there is a significant deviation from the initial slope of the curve (see inset of Fig. 6.12a) and to a partial penetration of the magnetic field in all the cases (see Fig. 6.12b). The time for reaching saturation is reduced linearly with increasing η, as indicated by the arrows in the inset of Fig. 6.12a. In this case the filaments are almost completely coupled, see field profiles in Fig. 6.12b, so that the strip has an aspect ratio of about 27 (as pointed out at the end of

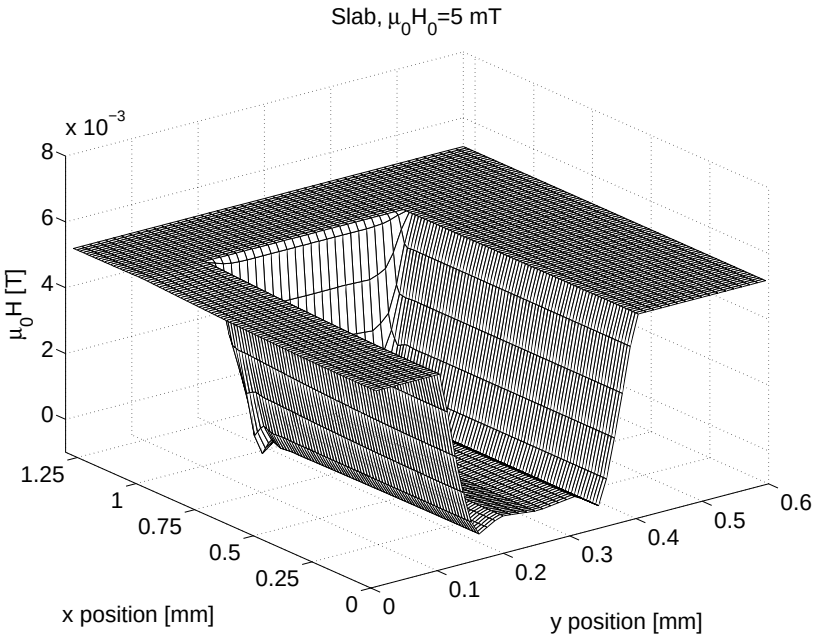

Figure 6.9: Penetration of the magnetic field in the slab, $\mu_0 H_0 = 5\ mT$, $f = 100\ Hz$.

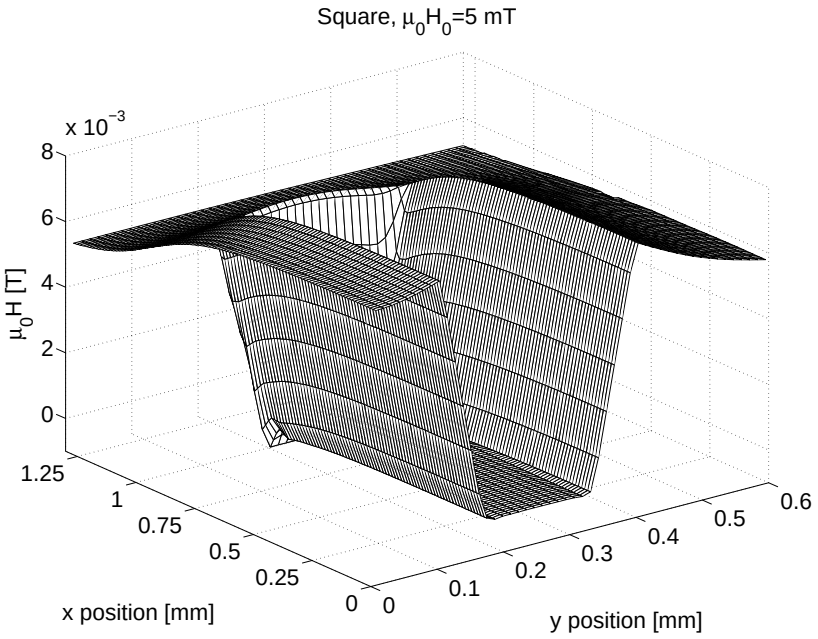

Figure 6.10: Penetration of the magnetic field in the square, $\mu_0 H_0 = 5\ mT$, $f = 100\ Hz$.

the previous section), which corresponds to a difference in the shape factor with the slab by a factor 27. The time at which the 2 A current is reached by the slab and strip geometries differs approximately by this factor. The square is an intermediate case and it is not easy to make precise numerical predictions on the value of this time: in fact, when the filaments are coupled, it has an aspect ratio of 2.7 (see end of the previous section) and its shape factor is not precisely determined, the formula a/b being valid only for strips ($a \gg b$).

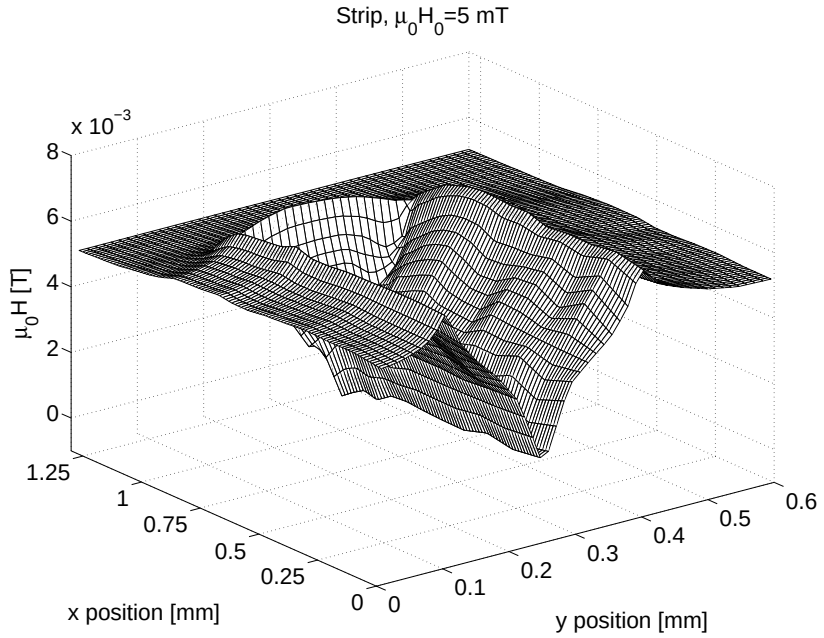

Figure 6.11: Penetration of the magnetic field in the strip, $\mu_0 H_0 = 5\ mT$, $f = 100\ Hz$.

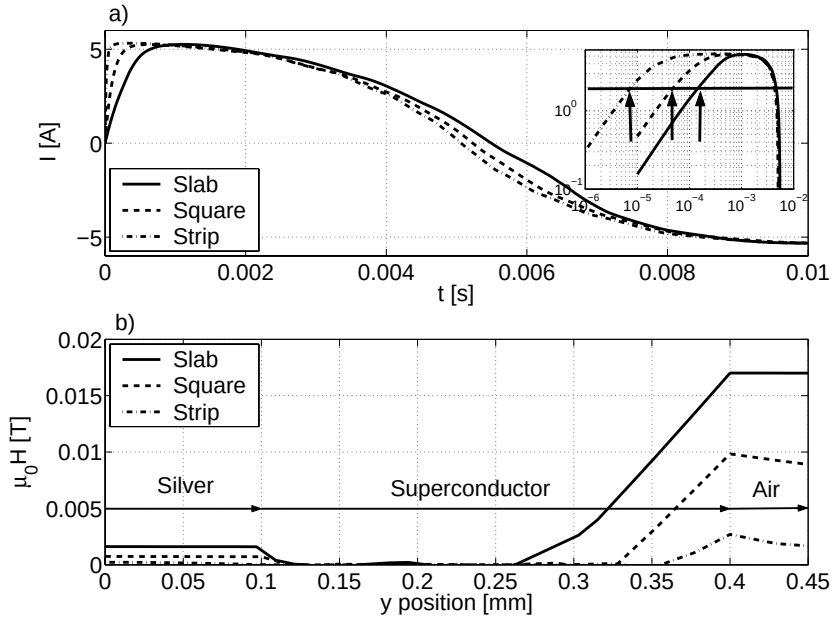

Figure 6.12: Evolution of the coupling current through the xz plane for the three geometries for $\mu_0 H_0 = 350\ mT$ at 50 Hz during the first half cycle (a), with a detailed view of the initial stage (inset). The current has been normalized by the aspect ratio in order to be compared. The scaling factors for the slab, the square and the strip are 0.05, 1 and 10, respectively. The magnetic field profiles at the time when the coupling current reaches 2 A (indicated by arrows in the inset of (a)) are shown in (b).

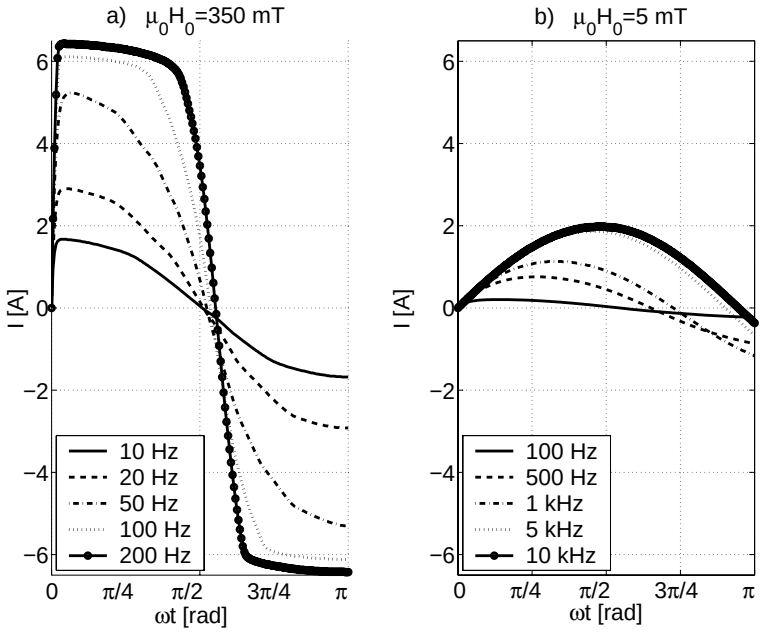

Figure 6.13: Coupling current evolution as a function of the angular frequency for a square geometry at different frequencies for $\mu_0 H_0 = 350\ mT$ (a) and $\mu_0 H_0 = 5\ mT$ (b).

A further example for the square is given in Fig. 6.13a, which depicts the time evolution of the coupling current at different frequencies, for an applied field of 350 mT. The current is plotted as a function of the angular frequency instead of the time, since the time intervals are very different due to the wide spectrum of the analyzed frequencies. The shape of the current evolution does not change for the different frequencies, because the field is so large that there are no significant changes in the field profiles and in the effective demagnetizing factor. The modulus of the coupling current increases with increasing frequency, i.e. passing from uncoupled to coupled situation. At high frequencies (fully coupled) the coupling current is larger than 6 A, whereas, according to the CSM, the maximum current a superconducting filament can carry should be J_c times the area of the cross-section of the filament, i.e. 4.5 A. This underlines again the difference between the CSM and the $E - J$ power-law model: according to the former, the maximum current density flowing in the superconductor is J_c, whereas the latter, due to the finite exponent of the power-law relation, allows exceeding this value, reaching locally $1.3 \div 1.4$ times J_c in this case. When the field amplitude is smaller and the field does not penetrate completely the filaments, the behaviour of the coupling current is different. The change of the frequency corresponds to a change of the field profiles and of the effective demagnetizing factor of the geometry. In this case there is not the saturation of the coupling current at the very beginning. By increasing the frequency the filaments become fully coupled and the coupling current becomes practically in phase with the applied field. Figure 6.13b shows the coupling current for a sinusoidal magnetic field of 5 mT at different frequencies for the square geometry. In this picture it is possible to see the increase of the maximum of the coupling current with the increasing frequency (which was also present with larger fields, see Fig. 6.13a) and the passage toward a coupling current in phase with the external field, emphasized by the displacement of the maximum to the right.

Another important quantity for evaluating the coupling effect is the AC losses in the silver matrix, computed according to Eq. 6.9. Figure 6.14a shows the losses per unit volume for the three geometries as a function of frequency for an external magnetic field of 5 mT. The

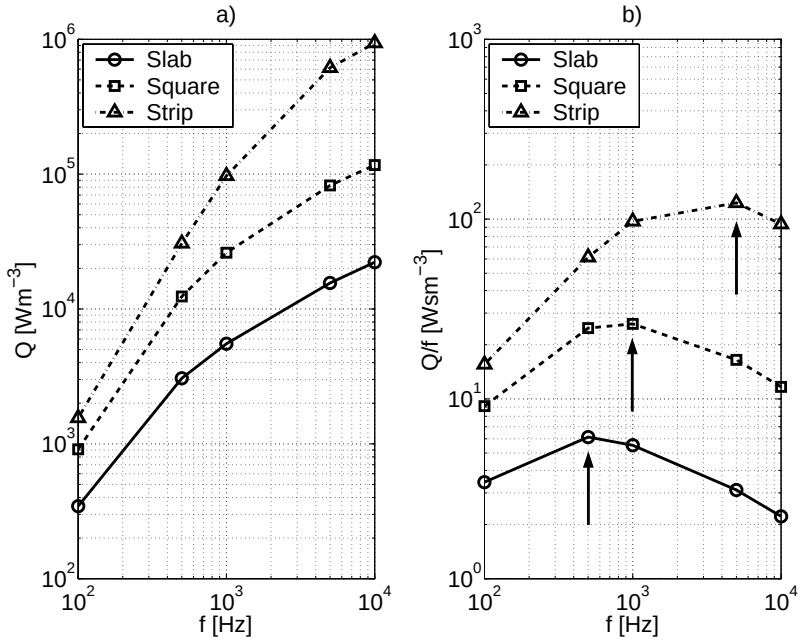

Figure 6.14: AC losses in the silver (per unit volume) for the three geometries as a function of frequency for $\mu_0 H_0 = 5\ mT$ (a). Identification of the "coupling field" (b).

strip geometry has the higher losses, since it is more easily penetrated by the magnetic field. Then there is the square and finally the slab, as expected. For all the geometries one can see that the slope of the curve changes as a function of frequency. In particular it flattens with increasing frequency, i.e. passing from a uncoupled to a coupled configuration, meaning that the coupling current has almost reached its maximum value and does not increase too much. This change of slope could be put in relation with the coupling field and could provide a quantitative determination of the coupling. In order to better visualize it, data have been divided by the frequency and then plotted again as a function of frequency itself, see Fig. 6.14b. The change of the slope of the previous curves is in this way transformed into a peak of the curve, which might identify the "coupling field", as displayed by the arrows [70].

The position of the peak shows that for a given magnetic field the slab geometry becomes coupled first (i.e. at lower frequency), then the square and finally the strip. This is quite surprising since, according to the faster increase of the coupling current in the geometries with larger aspect ratio, the coupling should occur first in the strip, then in the square and finally in the slab (see also Fig. 6.12). An explanation of this discrepancy can be found in the very different analyzed geometries, which correspond to different physical situations: a magnetic field of 5 mT partially penetrates the square and the slab, but fully penetrates the strip (see Figs. 6.7-6.8). However, the remaining discrepancy between square and slab, which are both partially penetrated, makes it necessary to find another criterion for defining the coupling field.

6.7 Influence of the conductor length and of the silver width and resistivity

For slab geometries, the critical field rate $\dot{B}$ and the square of the conductor length are expected to be inversely proportional according to Eq. 6.4. The increase of the length L with a fine mesh density makes the number of nodes and the computation time enormously increase for the slab.

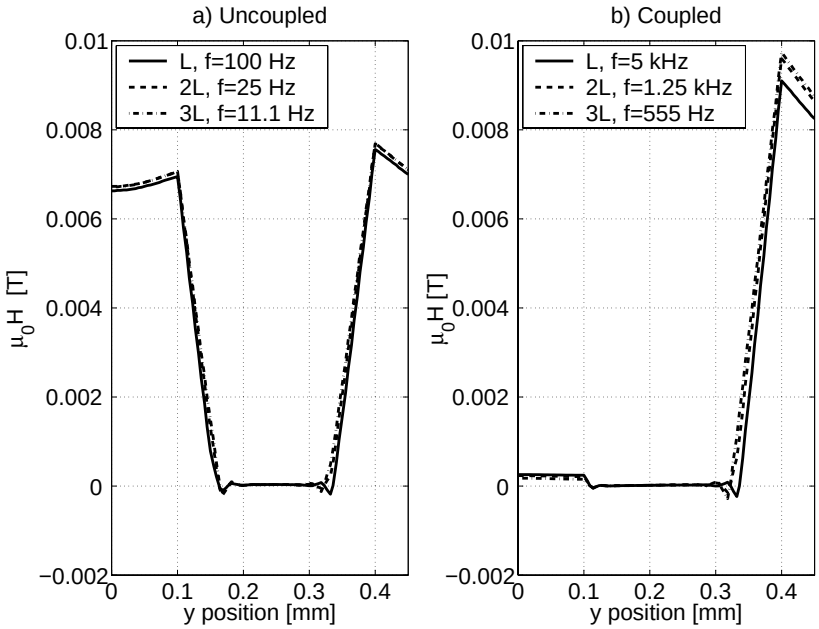

Figure 6.15: Field profiles along the positive y-axis of a square geometry for different lengths: 2 mm, 4 mm, 6 mm in the uncoupled (a) and coupled case (b). The corresponding variation rates have been varied in order to keep the product $\dot{B} \cdot L^2$ constant. The amplitude of 5 mT has been attained with a constant rate field: $H = \dot{H}t$, $\dot{H} = 2\pi H_0 f$.

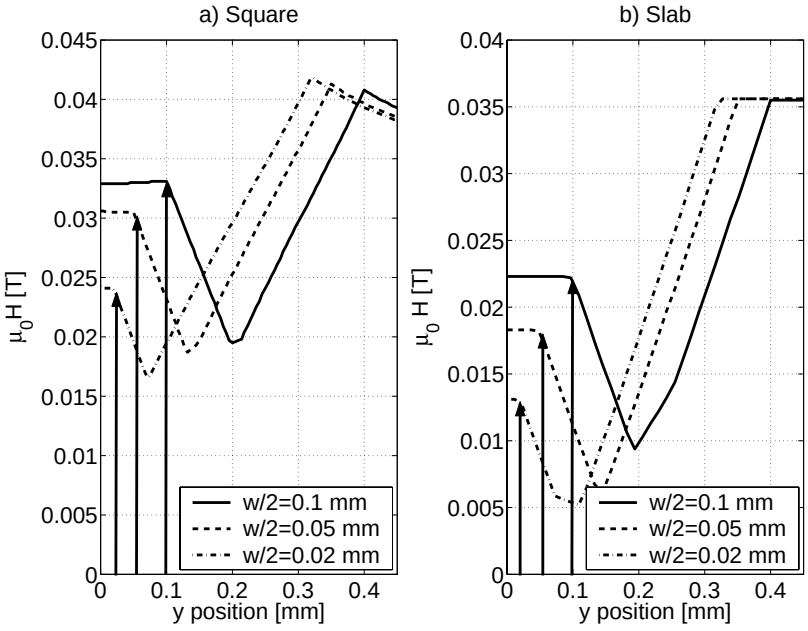

Figure 6.16: Field profiles along the positive y-axis, $\mu_0 H_0 = 35\ mT$, $f = 100\ Hz$ for three different values of silver width, for the square (a) and the slab (b). The arrows indicate the boundary between the silver and the superconductor in the three cases. The amplitude of 35 mT has been attained with a constant rate field: $H = \dot{H}t$, $\dot{H} = 2\pi H_0 f$.

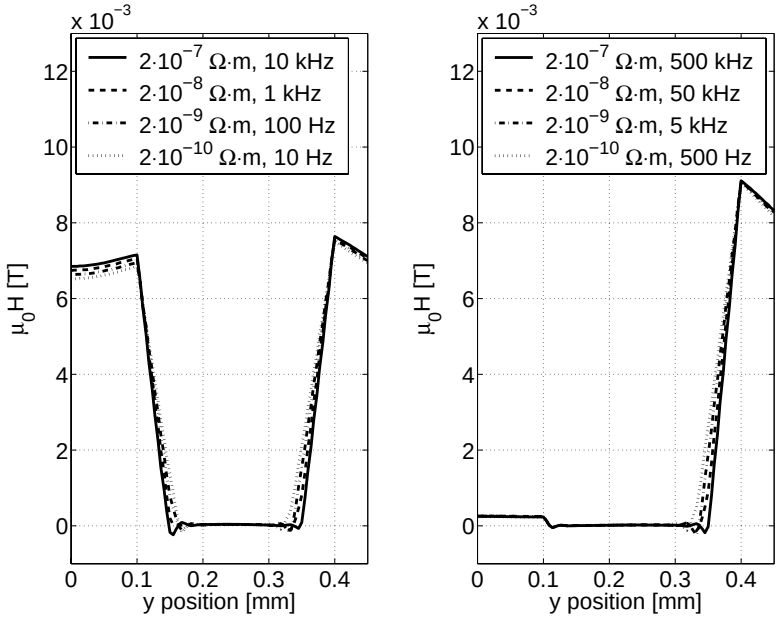

Figure 6.17: Magnetic field profiles for the square geometry, obtained by varying the resistivity of the normal matrix and the frequency of the field, but keeping constant their ratio. The simulations refer to a field of 5 mT obtained with a constant rate ramp.

Consequently, the length has been varied for the square geometry, for which the computation time remains reasonable even for long lengths. Moreover, always for reducing the computation time, the desired magnetic field amplitude has been obtained with a constant rate ($H = \dot{H}t$, $\dot{H} = 2\pi H_0 f$) instead of the usual sinusoidal field. Figure 6.15 shows a comparison in the case of a field amplitude of 5 mT between the usual geometry ($L = 2$ mm) and the case with L two and three times greater. The corresponding variation rates have been divided by 4 and 9, respectively, according to Eq. 6.4. The field profiles fall close to each other, meaning that the dependence of the coupling effect on the square of the conductor length can be considered valid for finite cross-sections, too.

Another prediction made by the theory developed for fully penetrated infinite slabs [68] is the lack of influence of the silver width on the critical magnetic field rate, see Eq. 6.4, where the only geometrical parameters are the half width of the superconducting filaments a and the length of the conductor L. If this is reasonable for an infinite slab, it is not the case for the studied geometry, where the silver width w is much smaller but still comparable with the height b. The results of the simulations show that the width of the silver plays an important role even for slabs. Figure 6.16 shows the modification of the field profile along the y-axis for the square (a) and for the slab (b), when the silver width is reduced from 0.2 mm to 0.1 mm and to 0.04 mm. Reducing this width, the filaments are more easily coupled, as clearly visible looking at the value of the field in the silver region: the lower the field in the silver, the higher the coupling of the filaments.

Finally, the dependence of the coupling on the resistivity of the normal metal between the filaments has been verified. According to Eq. 6.4, the resistivity and the frequency of the field are directly proportional: this means that the same magnetic field profile should be obtained by keeping constant the ratio $\rho/\dot{B}$. This has been verified on the square geometry, both for the uncoupled and coupled case, as displayed in Fig. 6.17.

6.8 Original contributions of this thesis

- Demonstration of the feasibility of 3D FEM computations for studying the coupling effect between superconducting filaments.
- Quantitative evaluation of the influence of the aspect ratio of the filaments on the shape of the magnetic field profiles and on the rising of the coupling current in a virgin sample.
- Investigation of the relation between the coupling and the geometrical and physical parameters of the conductors in the case of filaments with finite aspect ratio.
- Proposition of a criterion based on the coupling loss in the silver for determining the onset of coupling.

Chapter 7

Conclusion

This thesis work has been dedicated to the numerical modelling of superconducting tapes and cables, in order to determine the current and field distributions and compute the losses in AC regime.

The analyzed devices have been multi-filamentary Bi-2223/Ag tapes and HTS cables. For studying their electromagnetic behaviour, the finite element method has been mostly used. This method allows to obtain very detailed results, taking into consideration the local effects of the current/field distribution on the global performance of the device. The modelling of HTS cables has been split into two parts, due to the difficulty of simulating the entire geometry with the FEM technique. The investigation of the current repartition among the layers (which involves the 3D structure of the cables) has been performed with a macroscopic electrical model; the computation of the AC losses has been done with 2D FEM simulations, using the results from the electrical model as input data.

The accomplished results can be summarized as follows.

- The software package FLUX3D has been used for performing 2D finite element method simulations of multi-filamentary HTS tapes. The results have been validated by means of a comparison with the ones obtained with FLUX2D. This FEM software package was already in use in our group and its results had already been successfully compared with experimental measurements. The results from FLUX3D have also been compared with the ones obtained by another analytical model, based on a model originally developed by Brandt.

- Two power-law models with non-constant J_c and n have been implemented in FLUX3D. The first for describing the decrease of the local value of J_c and n from the centre to the edge of HTS tapes. As a result of this decrease, on the tested geometry the AC losses increase by about 50% with respect to the case when a constant value of the parameters is assumed. The second for describing the anisotropic decrease of the transport capacity in the presence of the magnetic field, either externally applied or self-generated. It has been shown that this latter dependence is particularly important for the AC loss evaluation for certain particular arrangements of the filaments inside the wires.

- A recently developed 3D formulation for problems coupled with circuit equations has been validated on a straight geometry that can be simulated in 2D, too. After that, the new model has been tested on typical 3D geometries, such as corner-shaped and twisted conductors.

- The use of the FEM technique has been extended to multi-layer HTS cables for evaluating their AC losses. In this case the B-dependence of the critical current density must be taken into consideration because of the large involved transport currents (order of kA), which

generate a magnetic self-field high enough to sensibly reduce the transport capacity of the cable. In addition to these FEM simulations (which have been performed in 2D), a simple electrical model of the cable has been proposed and implemented. This model considers the cable from the macroscopic point of view and allows to overcome the intrinsic limits of FEM computations for taking into account the 3D geometry of HTS cables. The electrical model allows to find the geometrical configurations of the cable (in terms of pitch length and winding direction of the layers) leading to a repartition of the transport current among the layers as uniform as possible, in order to minimize the AC losses in the superconductor. The evaluation of the AC losses has been done by means of 2D FEM simulations, with the use of independent current sources for injecting the desired current in each layer.

- The influence of the non-uniformity of the values of the parameters of individual tapes (contact resistance, I_c, n) on the global performance of a single-layer HTS cable has been studied by means of FEM simulations. It has been shown that such non-uniformities may influence the behaviour of the individual tapes, but not the one of the whole cable. This means that, for many purposes, macroscopic models can describe multi-layer cables in terms of layers instead of tapes.

- In the framework of the European Project BIG-POWA, I have collaborated with Pirelli for assembling a HTS power link. The conductor has been electrically characterized by Pirelli. FEM simulations have been performed in order to evaluate the efficiency of the filament decoupling obtained by using twisted filaments.

- An equivalent circuit model of the cable has been proposed as an alternative method for computing the current repartition and evaluating the AC losses within the same model. It does not provide detailed information on the current and field distributions inside conductors, but it is faster and of simpler use than FEM simulations.

- Finally, FEM simulations have been used for studying the coupling between filaments in multi-filamentary superconductors, induced by an externally applied varying magnetic field. This is a typical 3D effect and the use of FEM simulations is necessary for investigating the cases which are not addressed by the theory. In fact, theoretical predictions exist only in the particular case of fully penetrated infinite slabs, which in most cases constitute a too rough approximation. The current and field distributions have been investigated for a variety of cases with different geometries. At the best of author's knowledge, this approach has never been presented elsewhere.

Concerning future work and development, there are three main interesting directions to be followed:

1. In two dimensions, the temperature dependence of the superconductor parameters has to be introduced. Its implementation is mandatory for simulating problems of superconducting devices not operating at constant temperature, e.g. superconducting fault current limiters. This implementation is more complicated than the one of the dependence of J_c and n on the position or on the local magnetic field, because it involves the coupling between Maxwell's and heat equations.

2. In three dimensions, several improvements are needed for extensively simulating twisted geometries without enormously increasing the size of the problem. For example, the possibility of applying a periodicity condition along the third dimension would allow to simulate a virtually infinite conductor by drawing the geometry corresponding to one twist pitch only.

3. Another interesting subject is the modelling of the coated conductors, which are characterized by very high aspect ratios. In order to continue to use the FEM method, advanced meshing tools, such as the adaptive mesh, are undoubtedly necessary. On the other hand, the use of models which are in principle less sensible to large aspect ratios would be probably more convenient.

Appendix A

Modified power-law for currents largely exceeding I_C

When the superconductor is embedded in a normal metal matrix, as in the case of Bi-2223/Ag tapes, the power-law (A.1) gives a quite precise description of the transition from superconducting to normal state. In particular, the superconductor and normal metal material are modelled as an electric parallel, so that when the current exceeds I_c, the resistivity of the superconductor becomes quickly so large that the current finds a lower resistance path in the normal metal.

In the case of bulk superconductors, which are for example used for fault current limiters [47], there is not any normal metal where the current can flow when the resistance of the superconductor becomes too large. In this case, all the current can flow in the superconductor only, which is forced into the normal state. This means that its resistivity does not have an unbound increase as given by Eq. A.1, but saturates to the normal state value.

It is not easy to perform precise measurements of the resistivity as a function of the transport current because of the damaging of the sample and of the thermal instability due to the high dissipated power. On the other hand, it is reasonable to assume that the transition of the resistivity to the normal state value is similar to the one obtained by increasing the temperature above T_c, for which experimental data are available [71].

The precise shape of the curve describing the transition depends in general on the quality of the sample and no analytical formula exists. A simple way for obtaining a $\rho(J)$ relation which better reproduces the actual electrical behaviour of the superconductor is by adding a constant resistivity ρ_{sat} (equal to the value in the normal state) in parallel with the traditional power-law [72]:

$$\rho_{pl} = \frac{E_c^{1/n}}{J_c} |\mathbf{E}|^{(n-1)/n} + \rho_0 \tag{A.1}$$

$$\rho^* = \frac{\rho_{pl} \cdot \rho_{sat}}{\rho_{pl} + \rho_{sat}}. \tag{A.2}$$

It has to be remarked that the electrical parallel in Eq. A.2 has no physical meaning. It is only a simple way for having a $\rho(J)$ relation closer to reality than the unbound power-law (A.1). The results from simulations reported below are just an indication of the error that would be made by using the unbound power law (A.1) for evaluating the losses in a bulk superconductor when the current largely exceeds I_c.

A bulk superconductor has been simulated in 2D, with cross-section 2 mm × 0.015 mm, critical current density $J_c = 1.3\ A/m^2$ and $\rho_{sat} = 3.5 \cdot 10^{-6}\ \Omega \cdot m$. The inset of Fig. A.1 displays the difference between the usual and the modified power-law for two different values of the power index n: for $n = 21$ the two curves start to differ at $J \simeq 2J_c$, whereas for $n = 51$ the separation

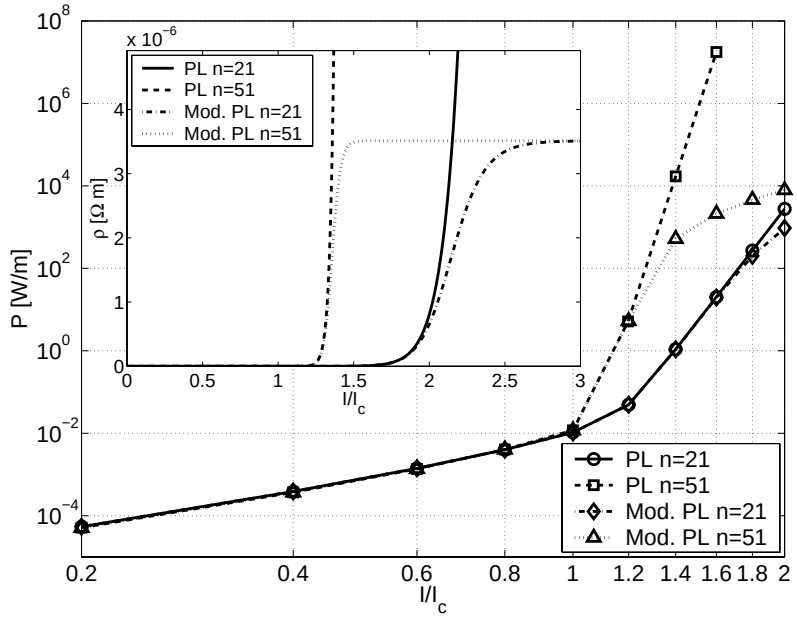

Figure A.1: AC losses as a function of the reduced transport current in a bulk superconductor, computed with a resistivity expressed by the usual and modified power-law, which are shown in the inset.

occurs at $J \simeq 1.3J_c$. The main window of Fig. A.1 shows the AC losses as a function of the transport current (normalized to I_c), computed using Eq. A.1 and Eq. A.2, for $n = 21$ and $n = 51$. For $I \leq I_c$, the losses are the same in all cases, as expected. For $I > I_c$ the losses computed with the two relations differ, the ones computed by Eq. A.2 being much smaller for those values of the current where the modified power law differs from the usual power-law.

Appendix B

The Newton-Raphson algorithm

In the solution process, the Newton-Raphson (NR) method is used for solving the system of non-linear equations. It is a method often used for solving non-linear problems and basically it consists in eliminating the non-linearity of the equations by introducing a linear residual. In particular, let the general non-linear system to be solved be

$$[A(X)][X] = [B], \tag{B.1}$$

where A depends on the solution vector X. By introducing the residual

$$[R(X)] = [A(X)][X] - [B], \tag{B.2}$$

the equation (B.1) can be re-written as

$$[R(X)] = 0. \tag{B.3}$$

The NR method therefore consists in solving a series of linear systems. For doing that, the residual is developed in Taylor series (first order) around the point X and, at each iteration, an increment of the solution ΔX is computed and added (after having been multiplied by a coefficient α) to the solution found at the previous iteration. The process is iterated until the residual becomes less than a threshold fixed by the user. For the simulations a threshold between 10^{-4} and 10^{-3} has been chosen. FLUX3D disposes of four methods for fixing the relaxation coefficient α. With the *scaled* method, the relaxation coefficient is determined at each iteration of the NR algorithm, depending on the value of the precision obtained at the previous iteration step. With the *fixed* method, the relaxation coefficient is assigned by the user in the interval (0,1] and is kept fixed during the solving process. With the *optimal* method, the relaxation coefficient is determined at each iteration. The principle consists in computing the coefficient such that to mimimize the following function:

$$W^i = \sum_{j=1}^{n} (R_j^i)^2. \tag{B.4}$$

In Eq. B.4 R_j^i is the j^{th} component of the residual $R(X^i)$ at the i^{th} iteration of the NR algorithm. $R(X^i)$ is a vector with n elements and n is the number of unknown of the system. The search of the minimum is done by using an iterative method; in particular, by computing the values of W^i for $\alpha = \alpha_k = 1/2^{k-1}$ (i.e. $\alpha = 1$, then 1/2, 1/4, 1/8,...) until when W_{k+1}^i becomes larger than W_k^i. Finally, with the *automatic* method, the software automatically determines, according to the utilized formulation, which one of the three methods is most suitable for the solution.

In most cases the optimal method has been used, since it allows to obtain a fast convergence at each time step, usually with only few iterations of the NR algorithm. Nevertheless, for some kinds

of problems, such as the study of the coupling effect, where rapid spatial and temporal variation of the variables are imposed, the fixed method proved to be more stable for the convergence. Especially in the initial stage of the simulation, for obtaining the convergence, low values of α (0.1 or 0.2) have to be used, and this makes the simulation quite slow (few tens of NR iterations necessary at each time step).

Bibliography

[1] J.C. Bednorz and K.A. Müller. Possible high-T_c superconductivity in the Ba-La-Cu-O system. *Zeitschrift fur Physik B*, 64(2):189, 1986.

[2] R. Mikkonen. Highlights of SC power applications in Europe. *IEEE Transactions on Applied Superconductivity*, 12(1):782, 2002.

[3] F. Grilli. Preparazione e caratterizzazione di nastri superconduttori di $(Bi, Pb)_2Sr_2Ca_2Cu_3O_{10}$ in matrice d'argento. Master's thesis, Dipartimento di Fisica, Università di Genova, 1998.

[4] A.C. Rose-Innes and E.H. Rhoderick. *Introduction to superconductivity*, volume 6 of *International Series in Solid State Physics*. Pergamon Press, UK, 2nd edition, 1978.

[5] K. Onnes. Further experiments with liquid helium. On the change of the electrical resistance of pure metal at very low temperature. *Leiden Comm.*, 122b:3–5, 13–15, 21–25, 1911.

[6] W. Aschcroft and D. Mermin. *Solid State Physics*. Saunders College Publishing, USA, 1976.

[7] W. Meissner and R. Ochsenfeld. Ein neuer Effekt bei Entritt der Supraleitfähigkeit. *Die Naturwissenschaften*, 21:787, 1933.

[8] J. Bardeen, L.N. Cooper, and J.R. Schrieffer. Theory of superconductivity. *Physical Review*, 108:1175, 1957.

[9] F. London and H. London. The electromagnetic equations of the superconductor. *Proceedings of the Royal Society*, A149:71, 1935.

[10] V.L. Ginzburg and L.D. Landau. On the theory of superconductivity. *Zhurnal Experimentalnoi i Theoreticheskoi Fisiki*, 20:1064, 1950 (in Russian).

[11] A.A. Abrikosov. *Zhurnal Experimentalnoi i Theoreticheskoi Fisiki*, 32:1442, 1957. English translation in Soviet Physics - Journal of experimental and theoretical physics 5:1174, 1957.

[12] R.N. Richardson and A.C.R. Tavner. Neon liquefaction system for high T_c experiments. *Cryogenics*, 35:195, 1995.

[13] M. Nunez-Regueiro, J.L. Tholence, E.V. Antipov, J.J. Capponi, and M. Marezio. Pressure induced enhancement of T_c up to 150 K in Hg-1223. *Science*, 262:97, 1993.

[14] R. Wesche. *High-temperature superconductors: materials, properties, and applications*. International Series in Solid State Physics. Kluwer Academic Publishers, Boston, USA, 1998.

[15] A. Jeremie, R. Flükiger, and E.W. Seibt. Effect of controlled carbon impurities on J_c in Ag/Bi(2223) tapes. *IEEE Transactions on Magnetics*, 30(4):1883, 1994.

[16] G. Grasso. *Preparation and superconducting properties of silver-sheathed* $(Bi, Pb)_2Sr_2Ca_2Cu_3O_{10}$ *tapes*. Thesis no. 2962, University of Geneva, Geneva, Switzerland, 1998.

[17] C.P. Bean. Magnetization of hard superconductors. *Physical Review Letters*, 8(6):250, 1962.

[18] C.P. Bean. Magnetization of high-field superconductors. *Reviews of Modern Physics*, 36:31, 1964.

[19] E.H. Brandt and M. Indenbohm. Type-II superconductor strip with current in a perpendicular magnetic field. *Physical Review B*, 48(17):12893, 1993.

[20] M. Maslouh, F. Bouillault, and J.C. Verite. Two-Dimensional numerical modeling of superconductors with imposed currents by the finite element method. *IEEE Transactions on Magnetics*, 36(4):1234, 2000.

[21] N. Amemiya, S. Murasawa, N. Banno, and K. Miyamoto. Numerical modelings of superconducting wires for AC loss calculations. *Physica C*, 310:16, 1998.

[22] N. Nibbio. *Nonlinear electromagnetic modeling of high temperature superconducting tapes*. Thesis no. 2031, Swiss Federal Institute of Technology - Lausanne, Lausanne, Switzerland, 1999.

[23] Y. Le Floch. *Dévéloppement de formulations 3D éléments finis* TΦ *pour la prise en compte de conducteurs massifs et bobinés avec un couplage circuit*. PhD thesis, Institut National Polytechnique de Grenoble, Grenoble, France, 2002.

[24] E. Vinot, G. Meunier, and P. Tixador. Different formulations to model superconductors. *IEEE Transactions on Magnetics*, 36(4):1226, 2000.

[25] E. Vinot. *Modélisation des supraconducteurs HTC. Applications au calcul des pertes AC*. PhD thesis, Institut National Polytechnique de Grenoble, Grenoble, France, 2000.

[26] G. Meunier, Y. Le Floch, and C. Guérin. A nonlinear circuit coupled $t - t_0 - \phi$ formulation for solid conductors. *IEEE Transactions on Magnetics*, 39(3):1729, 2003.

[27] S. Stavrev, F. Grilli, B. Dutoit, N. Nibbio, E. Vinot, I. Klutsch, G. Meunier, P. Tixador, Y. Yang, and E. Martinez. Comparison of numerical methods for modeling of superconductors. *IEEE Transactions on Magnetics*, 38(2):849, 2002.

[28] S. Stavrev. *Modelling of high temperature superconductors for AC power applications*. Thesis no. 2579, Swiss Federal Institute of Technology - Lausanne, Lausanne, Switzerland, 2002.

[29] E.H. Brandt. Superconductors of finite thickness in a perpendicular magnetic field: Strips and slabs. *Physical Review B*, 54(6):4246, 1996.

[30] Y. Yang, E. Martínez, and C. Beduz. Numerical modeling of the critical state and calculation of AC losses and current profiles in multi-filamentary Bi-2223 tapes. *Inst. Phys. Conf. Ser.*, (167):855, 1999.

[31] W.T. Norris. Calculation of hysteresis loss in hard superconductors carrying ac: isolated conductors and edges of thin sheets. *Journal of Physics D: Applied Physics*, 3:489, 1970.

[32] G. Strano, A.S. Siri, and G. Grasso. Current distribution and microstructure studies of isolated filaments extracted from Ag-sheathed Bi(2223) tapes. *Superconductor Science and Technology*, 13:1470, 2000.

[33] G. Grasso, B. Hensel, A. Jeremie, and R. Flükiger. Distribution of the transport critical current density in Ag sheathed $(Bi, Pb)_2Sr_2Ca_2Cu_3O_x$ tapes produced by rolling. *Physica C*, 221:45, 1995.

[34] A.V. Volkozub, J. Everett, G. Perkins, P. Buscemi, A.D Caplin, M. Dhallé, F. Marti, G. Grasso, Y.B. Huang, and R. Flükiger. The analysis of current distribution in filamentary conductors: the influence of intergrowths. *IEEE Transactions on Applied Superconductivity*, 9(2):2147, 1999.

[35] B. ten Haken, H.J.N. van Eck, and H.H.J. ten Kate. A new experimental method to determine the local critical current density in high-temperature superconducting tapes. *Physica C*, 334:163, 2000.

[36] S. Stavrev, Y. Yang, and B. Dutoit. Modelling and AC losses of BSCCO conductors with anisotropic and position-dependent J_c. *Physica C*, 378-381:1091, 2002.

[37] L.N. Bulaevskii, J.R. Clem, L.I. Glazman, and A.P. Malozemoff. Model for the low-temperature transport of Bi-based high-temperature superconducting tapes. *Physical Review B*, 45(5):2545, 1992.

[38] Y.B. Kim, C.F. Hempstead, and A.R. Strnad. Critical persistent currents in hard superconductors. *Physical Review Letters*, 9(7):306, 1962.

[39] P.W. Anderson. Theory of flux creep in hard superconductors. *Physical Review Letters*, 9(7):309, 1962.

[40] N. Amemiya and Y. Otha. Mode of magnetic flux penetration into high T_c superconductors with various cross-sectional shape and their AC loss characteristics. *Physica C*, 357-360:1134, 2001.

[41] M. Maslouh, F. Bouillault, A. Bossavit, and J.C. Vérité. Numerical modelling of superconductor materials using an anisotropic Kim law. *IEEE Transactions on Magnetics*, 34(5):3064, 1998.

[42] N. Nibbio, S. Stavrev, and B. Dutoit. Finite element method simulation of AC loss in HTS tapes with B-dependent E-J power law. *IEEE Transactions on Applied Superconductivity*, 11(1):2627, 2001.

[43] O. van der Meer, B. ten Haken, and H.H.J. ten Kate. A model to describe the angular dependence of the critical current in a Bi-2223/Ag superconducting tape. *Physica C*, 357-360:1174, 2001.

[44] B. Dutoit, M. Sjöström, and S. Stavrev. Bi(2223) Ag sheathed tape I_c and exponent n characterization and modelling under DC magnetic field. *IEEE Transactions on Applied Superconductivity*, 9(2):809, 1999.

[45] S. Stavrev, B. Dutoit, and P. Lombard. Numerical modelling and AC losses in multifilamentary Bi-2223/Ag conductors with various geometry and filament arrangement. *Physica C*, 384:19, 2003.

[46] S. Stavrev, B. Dutoit, and N. Nibbio. Geometry considerations for use of Bi-2223/Ag tapes and wires with different models of $J_c(B)$. *IEEE Transactions on Applied Superconductivity*, 12(3):1857, 2002.

[47] J.G. Noudem, D. Bourgault, J.M. Barbut, P. Tixador, and R. Tournier. Possible application of bulk textured Bi:2223 for current limitation. *Physica C*, 349:47, 2001.

[48] P.W. Fisher, M.J. Cole, J. A. Demko, C.A. Foster, M. J. Gouge, R.W. Grabovickic, J.W. Lue, J.P. Stovall, D.T. Lindsay, M.L. Roden, and J. C. Tolbert. Design, analysis, and fabrication of a tri-axial cable system. *IEEE Transactions on Applied Superconductivity*, 13(2):1938, 2003.

[49] S. Mukoyama, K. Miyoshi, H. Tsubouti, M. Mimitra, N. Uno, N.Ichiyanagi, Y. Tanaka, M. Ikeda, H. Ishii, S. Honjo, Y. Sato, T. Hara, and Y. Iwata. 50-m long HTS conductor for power cable. *IEEE Transactions on Applied Superconductivity*, 7(2):1069, 1997.

[50] S. Mukoyama, K. Miyoshi, H. Tsubouti, T. Yoshida, M. Mimura, N. Uno, M. Ikeda, H. Ishii, S. Honjo, and Y. Iwata. Uniform current distribution conductor of HTS power cable with variable tape-winding pitches. *IEEE Transactions on Applied Superconductivity*, 9(2):1269, 1999.

[51] K. Goto, C. Suzuki, K. Takada, T. Hasegawa, N. Kashima, and S. Nagaya. Development of HTS cable with Bi-2223 transposed segment conductors. *Physica C*, 357-360:1255, 2001.

[52] F. Grilli, S. Stavrev, B. Dutoit, and S. Spreafico. Numerical modeling of a HTS cable. *IEEE Transactions on Applied Superconductivity*, 13(2):1886, 2003.

[53] S. Krüger Olsen, C. Træholt, A. Kühle, O. Tønnesen, M. Däumling, and J. Østergaard. Loss and inductance investigations in a 4-layer superconducting prototype cable conductor. *IEEE Transactions on Applied Superconductivity*, 9(2):833, 1999.

[54] H. Noji. AC loss of a high-T_c superconducting power-cable conductor. *Superconductor Science and Technology*, 10:552, 1997.

[55] L. Masur, D. Parker, M. Tanner, E. Podtburg, D. Buczek, J. Scudiere, P. Caracino, S. Spreafico, P. Corsaro, and M. Nassi. Long length manufacturing of high performance BSCCO-2223 tape for the Detroit Edison power cable project. *IEEE Transactions on Applied Superconductivity*, 11(1):3256, 2001.

[56] V.E. Sytnikov, P.I. Dolgosheev, G.G. Svalov, N.V. Polyakova, and D.I. Belij. Influence of the multilayer HTS-cable conductor design on the current distribution. *Physica C*, 310:387, 1998.

[57] P. Corsaro, M. Bechis, P. Caracino, W. Castiglioni, G. Cavalleri, G. Coletta, G. Colombo, P. Ladiè, A. Mansoldo, R. Mele, S. Montagner, C. Moro, M. Nassi, S. Spreafico, N. Kelley, and C. Wakefield. Manufacturing and commissioning of 24 kV superconducting cable in Detroit. *Physica C*, 378-381:1168, 2002.

[58] S. Mukoyama, N. Ishii, H. Iizuka, M. Yagi, H. Hirano, S. Maruyama, Y. Yagi, M. Mimura, O. Sato, and A. Kikuchi. Development of high-T_c superconducting power cable. *Furukawa Review*, 23:82, 2003.

[59] G. Vellego and P. Metra. An analysis of the transport losses measured on HTSC single-phase conductor prototypes. *Superconductor Science and Technology*, 8:476, 1995.

[60] J. Rieger, M. Leghissa, J. Wiezoreck, H.P. Krämer, G. Ries, and H.W. Neumüller. Development of a 10 m long superconducting multistrand conductor for power transmission cables. *Superconductor Science and Technology*, 11:902, 1998.

[61] M. Leghissa, J. Rieger, H.W. Neumüller, J. Wiezoreck, F. Schmidt, W. Nick, P. van Hasselt, and R. Schroth. Development of HTS power transmission cables. *IEEE Transactions on Applied Superconductivity*, 9(2):406, 1999.

[62] F. Gömöry, E. Janíková, and J. Šouc. Resistive losses in a high-T_c wire carrying AC current larger than I_c. *Superconductor Science and Technology*, 15:1345, 2002.

[63] J.R. Clem, M. Benkraouda, T. Pe, and J. McDonald. Penetration of magnetic flux and electrical current density into superconducting strips and disks. *Chinese Journal of Physics*, 34(2):284, 1996.

[64] M. Sjöström. *Hysteresis modelling of high temperature superconductors.* Thesis no. 2372, Swiss Federal Institute of Technology - Lausanne, Lausanne, Switzerland, 2001.

[65] I.D. Mayergoyz. *Mathematical models of hysteresis.* Springer-Verlag, New York, USA, 1991.

[66] M. Sjöström. Differentiation and power loss computation of classical Preisach model. *Physica B*, in press, 2003.

[67] M. Sjöström. Possibilities and limitations of using Preisach model for hysteresis in superconductors. *Physica B*, 306:256, 2001.

[68] M.N. Wilson. *Superconducting magnets.* Oxford Science Publications. Clarendon Press, Oxford, UK, 1983.

[69] A. M. Campbell. A general treatment of AC losses in multifilamentary superconductors. *Cryogenics*, 22:3, 1982.

[70] E. Martínez, Y. Yang, C. Beduz, and Y.B. Huang. Experimental study of loss mechanisms of AgAu/PbBi-2223 tapes with twisted filaments under perpendicular AC magnetic fields at power frequencies. *Physica C*, 331:216, 2000.

[71] G. Grasso, F. Marti, Y. Huang, A. Perin, and R. Flükiger. Correlation between the normal state resistivity and the critical current density of Ag sheathed Bi(2223) tapes. *Physica C*, 281:271, 1997.

[72] J. Duron, F. Grilli, B. Dutoit, and S. Stavrev. Modelling the E-J relation of high-T_c superconductors in an arbitrary current range. *Physica C*, 401:176, 2004.

Curriculum vitæ et studiorum

Francesco Grilli was born in Genoa, Italy, on 1974 December 4^{th}. In 1998 he received the M.S. degree in Physics from the University of Genoa (final grade 110/110) with a diploma work entitled *Preparation and characterization of silver sheathed* $(Bi,Pb)_2Sr_2Ca_2Cu_3O_{10}$ *tapes*. After that, during the civil service (in substitution of the army), he received two study grants from the National Institute for the Physics of Matter (INFM) for developing a project of scientific divulgation and for continuing the research activity of the diploma work.

From October 1999 to August 2000 he worked as software engineer at Marconi Communications, a worldwide leader company in telecommunications.

In September 2000 he joined the Laboratory of Nonlinear Systems at the Swiss Federal Institute of Technology - Lausanne, where he followed the Doctoral School in Communication Systems and started his Ph.D. research activity, whose most important results have been summarized in the present manuscript.

Publications

- G. Grasso, F. Marti, F. Grilli, A.S. Siri, and R. Flükiger. Development of Ag-sheathed Bi(2223) tapes with oriented filaments. *Cryogenics*, 39(3):267, 1999.
- G. Grasso, F. Grilli, A.S. Siri, F. Marti, Y. Huang, and R. Flükiger. Optimization of Bi(2223)/Ag conductors for practical applications. *Philosophical Magazine B*, 80(5):991, 2000.
- S. Stavrev, F. Grilli, B. Dutoit, N. Nibbio, E. Vinot, I. Klutsch, G. Meunier, P. Tixador, Y. Yang, and E. Martinez. Comparison of Numerical Methods for Modelling of Superconductors. *IEEE Transactions on Magnetics*, 38(2):849, 2002.
- S. Stavrev, F. Grilli, B. Dutoit, I. Klutsch, E. Vinot, P. Tixador, G. Meunier, P. Skov-Hansen, and J. Bindslev Hansen. Numerical modelling of Bi-2223 multifilamentary tapes with position-dependent J_c. *Physica C*, 372:1800, 2002.
- F. Grilli, S. Stavrev, B. Dutoit, and S. Spreafico. Numerical Modeling of a HTS Cable. *IEEE Transactions on Applied Superconductivity*, 13(2):1886, 2003.
- M. Costa, E. Martínez, C. Beduz, Y. Yang, F. Grilli, B. Dutoit, E. Vinot, and P. Tixador. 3D Modelling of Coupling between Superconducting Filaments via Resistive Matrix in AC Magnetic Field. *IEEE Transactions on Applied Superconductivity*, 13(2):3634, 2003.
- S. Stavrev, B. Dutoit, and F. Grilli. Self-field and geometry effects in transport current applications of multifilamentary Bi-2223/Ag conductors. *IEEE Transactions on Applied Superconductivity*, 13(3):3807, 2003.
- F. Grilli, M. Costa Bouzo, Y. Yang, C. Beduz, and B. Dutoit. Finite element method analysis of the coupling effect between superconducting filaments of different aspect ratio. *Superconductor Science and Technology*, 16(10):1128, 2003.

- F. Grilli, S. Stavrev, B. Dutoit, S. Spreafico, R. Tebano, G. Coletta, F. Gömöry, L. Frolek, and J. Šouc. Numerical modelling of a HTS cable in AC regime. *Physica C*, 401:176, 2004.
- J. Duron, F. Grilli, B. Dutoit, and S. Stavrev. Modelling the E-J relation of high-T_c superconductors in an arbitrary current range. *Physica C*, 401:231, 2004.
- F. Grilli and M. Sjöström. Prediction of resistive and hysteretic losses in a multi-layer HTS Cable. Accepted for publication in *Superconductor Science and Technology*.
- F. Grilli, S. Stavrev, B. Dutoit, and S. Spreafico. Numerical analysis of the magnetic self-field effects on the transport properties of a multi-layer HTS cable. Accepted for publication in *IEEE Transactions on Applied Superconductivity*.

Awards

- Best poster award at the Conference on Electromagnetic Field Computation, Perugia, Italy, 16-19 June 2002, with a poster entitled "Numerical modelling of superconductors: from 2D to 3D".